ABSTRACT

V-SHAPED TEMPERATURE DEPENDENCES AND PRESSURE DEPENDENCE OF ELEMENTARY REACTIONS OF HYDROXYL RADICALS WITH SEVERAL ORGANOPHOSPHORUS COMPOUNDS

by
Xiaokai Zhang

Organophosphorus compounds have brought increasing attention since they are widely used as flame-retardants, which can take effect in combustion via reactions with reactive radicals. These reactions are influenced by variables such as temperature and pressure, resulting in a temperature and pressure dependent rate constant. Studying this reaction kinetics has great importance in both combustion reaction and atmospheric environment.

This study is focused on kinetics of several elementary reactions of combustion importance. The kinetics of hydroxyl radicals were studied using pulsed laser photolysis coupled to transient UV-vis absorption spectroscopy over the 295 – 837 K temperature range and the 1 - 30 bar pressure range. Hydroxyl radical was generated by photolysis of N_2O/H_2O/He. The time-resolved OH absorption profiles were fitted by different models to get the reaction rate constant at corresponding reaction conditions.

Three such reactions were experimentally studied, reactions of OH with trimethyl phosphate (TMP), dimethyl methyl phosphonate (DMMP), and trimethyl phosphite (TMPi). All three compounds exhibit the features predicted for elementary reactions with "negative" (submerged) barriers, where V-shaped temperature dependencies are observed (negative at low and positive at elevated temperatures). For reaction OH + DMMP, bath gas pressure dependence was also observed (1 – 30 bar, He). These reactions are suggested to have "transition states" with the ground state lying below the ground state of the

reactants, presumably caused by the “long-range electrostatic interactions” in the “transition states”.

V-SHAPED TEMPERATURE DEPENDENCES AND PRESSURE DEPENDENCE OF ELEMENTARY REACTIONS OF HYDROXYL RADICALS WITH SEVERAL ORGANOPHOSPHORUS COMPOUNDS

by
Xiaokai Zhang

A Dissertation
Submitted to the Faculty of
New Jersey Institute of Technology
in Partial Fulfillment of the Requirements for the Degree of
Doctor of Philosophy in Chemistry

Department of Chemistry and Environmental Science

May 2023

APPROVAL PAGE

V-SHAPED TEMPERATURE DEPENDENCES AND PRESSURE DEPENDENCE OF ELEMENTARY REACTIONS OF HYDROXYL RADICALS WITH SEVERAL ORGANOPHOSPHORUS COMPOUNDS

Xiaokai Zhang

Dr. Lev N. Krasnoperov, Dissertation Advisor — Date
Professor of Chemistry and Environmental Science, NJIT

Dr. Alexei Khalizov, Committee Member — Date
Associate Professor of Chemistry and Environmental Science, NJIT

Dr. Farnaz Shakib, Committee Member — Date
Assistant Professor of Chemistry and Environmental Science, NJIT

Dr. Xianqin Wang, Committee Member — Date
Professor of Chemical and Materials Engineering, NJIT

Dr. Mirko Schoenitz, Committee Member — Date
Associate Professor of Chemical and Materials Engineering, NJIT

BIOGRAPHICAL SKETCH

Author: Xiaokai Zhang

Degree: Doctor of Philosophy

Date: May 2023

Undergraduate and Graduate Education:

- Doctor of Philosophy in Chemistry,
New Jersey Institute of Technology, Newark, NJ, 2023

- Master of Science in Chemistry,
New Jersey Institute of Technology, Newark, NJ, 2018

- Bachelor of Science in Chemistry,
Beihang University, Beijing, China, 2015

Major: Chemistry

Publications:

Zhang, X., Sangwan, M., Yan, C., Koshlyakov, P. V., Chesnokov, E. N., Bedjanian, Y., & Krasnoperov, L. N. (2020). Disproportionation channel of the self-reaction of hydroxyl radical, OH+OH→ H_2O+O, revisited. *The Journal of Physical Chemistry A*, 124(20), 3993-4005.

Koshlyakov, P. V., Barkova, D. A., Gerasimov, I. E., Chesnokov, E. N., Zhang, X., & Krasnoperov, L. N. (2021). Kinetics of the gas-phase reaction of hydroxyl radicals with trimethyl phosphate over the 273–837 K temperature range. *The Royal Society of Chemistry*, 11(23), 14121-14131.

Zhang, X., Barkova, D. A., Koshlyakov, P. V., Gerasimov, I. E., Chesnokov, E. N., & Krasnoperov, L. N. (2022). Kinetics of the Gas-Phase Reaction of Hydroxyl Radicals with Dimethyl Methylphosphonate (DMMP) over an Extended Temperature Range (273–837 K). *Molecules*, 27(7), 2301.

Zhang, X., Krasnoperov, L. N. "V-shaped temperature dependence of reaction OH +Trimethyl Phosphite over the 295-837 K temperature range". Paper in preparation.

Scientific Presentations:

Xiaokai Zhang and Lev N. Krasnoperov, “Kinetics of the Reactions of Hydroxyl Radical (OH) with Trimethyl Phosphate (TMP) and Dimethyl Methyl Phosphonate (DMMP) over Extended Temperature and Pressure Ranges”, presentation at the 2021 Regional Meeting on Kinetics and Dynamic, online.

Xiaokai Zhang and Lev N. Krasnoperov, “Kinetics of the Reactions of Hydroxyl Radical (OH) with Organophosphorus Compounds over Extended Temperature (298~837 K) and Pressure Ranges (1~100 bar)”, presentation at the 2022 Regional Meeting on Kinetics and Dynamic, online.

Xiaokai Zhang and Lev N. Krasnoperov, “V-shaped temperature dependences and pressure dependences of elementary reactions of hydroxyl radicals with several organophosphorus compounds”, presentation at the 2022 Northeast Regional Meeting, Rochester, NY, USA, 2022.

ACKNOWLEDGEMENT

I would like to express my deepest gratitude to my dissertation supervisor, Dr. Lev N. Krasnoperov, for his invaluable guidance, support, and encouragement throughout my PhD research. His expertise, feedback, and constructive criticism have been instrumental in shaping my research project and improving the quality of my work.

I would like to thank the members of my dissertation committee, Dr. Alexei Khalizov, Dr. Farnaz Shakib, Dr. Xianqin Wang, and Dr. Mirko Schoenitz, for their insightful feedback and valuable suggestions that have contributed to the improvement of my dissertation.

I would also like to thank Dr. Joseph Bozzelli for providing the help of calculation related to my research work.

I am grateful to the Department of Chemistry and Environmental Science for providing financial support for my PhD studies. Their generous funding has made it possible for me to pursue my academic goals and complete my research. I spent 6 years studying here, and it has already become a home to me.

I would like to acknowledge the support and encouragement of my parents, Junlao Zhang and Xuecao Xie, and my wife, Xi Gao. Their love, patience, and understanding have been essential in keeping me motivated throughout the ups and downs of the PhD journey.

Finally, I would like to express my heartfelt gratitude to all the participants who generously gave their time and insights for my research project. Without their cooperation and willingness to share their experiences, my research would not have been possible.

Thank you all for your support and contributions.

TABLE OF CONTENTS

TABLE OF CONTENTS
(Continued)

TABLE OF CONTENTS
(Continued)

Chapter **Page**

LIST OF TABLES

Table **Page**

LIST OF FIGURES

Figure **Page**

LIST OF FIGURES
(Continued)

Figure **Page**

LIST OF FIGURES
(Continued)

Figure **Page**

CHAPTER 1

INTRODUCTION

1.1 Objective

The objective of this dissertation is to study the elementary free radical-radical/molecule reactions of combustion importance over an extended temperature and pressure range. Organophosphorus compounds, which are widely used as a flame retardant, have been brought an increasing attention as their industrial applications grow. While we have little knowledge about the reaction kinetics of organophosphorus compounds, in both combustion and environmental reactions.

Combustion reactions involve thousands of elementary reactions and hundreds of free radicals, with temperature and pressure often exhibiting significant fluctuations in certain instances. Studying the temperature and pressure effect on the reactions is therefore crucial to help us to understand the mechanism related to combustion process.

In combustion, reactive radicals play important roles since they are involved in all stages. The radicals can control important parameters of combustion, such as the ignition delay, the flame propagation speed, etc.

While quantitative kinetic studies of combustion-related reactions face several challenges, including lack of clean radical sources, overlap of the absorption spectra of different species. UV-vis absorption spectroscopy is capable of monitoring transient species with a high accuracy. Due to several limitations, such as the laser energy at the exit and a lower absorption cross section of OH radicals at high pressures, experimental

measurements of the rate constants were normally performed under the low-pressure conditions (up to 1 bar).

In this work, a pulsed laser photolysis - transient UV absorption technique was used to study the reaction kinetics of OH radicals with several organophosphorus compounds over an extended temperature and pressure ranges. The self-reaction of OH radicals is also discussed in Chapter 3. Trimethyl Phosphate (TMP), Dimethyl Methyl Phosphonate (DMMP), and Trimethyl Phosphite (TMPi) were chosen as three representing organophosphorus compounds (based on their molecular structures). The rate constants of the reactions of organophosphorus compounds with OH radicals were determined with the decay curves of the OH radicals' signals. Hydroxyl radials were produced in the fast reaction of electronically excited oxygen atoms $O(^1D)$ with H_2O. The electronically excited oxygen atoms were produced in the photolysis of N_2O at 193 nm (ArF excimer laser). The result of the study (the rate constants, including the temperature dependences and the pressure dependences) could enhance our understanding of the kinetics and mechanisms of such reactions important in combustion as well as the atmospheric chemistry, and better understand the flame retardation mechanisms caused by these compounds.

1.2 Background Information

1.2.1 General mechanism of combustion reactions

Usually combustion mechanisms consist of hundreds of elementary reactions[1-3] involving free radicals and molecules, including the chain initiation, chain propagation, chain branching and chain termination steps.[4] Use alkane RH as an example:[5]

$$RH + O_2 \rightarrow R\cdot + HOO\cdot \qquad \text{(initiation)}$$

$$R\cdot + O_2 \rightarrow RO\cdot + \cdot O\cdot \qquad \text{(branching)}$$

$$RH + RO\cdot \rightarrow R\cdot + ROH \qquad \text{(propagation)}$$

$$HOO\cdot + \cdot OH \rightarrow H_2O + O_2 \qquad \text{(termination)}$$

Despite the physical form of the combustible materials (liquid or solid), they always evaporate or/and pyrolyze into the gas phase first.[6, 7] Studying the gas phase radical kinetics has significant meaning in combustion reactions and related environmental science. Figure 1.1 shows an over simplified initial stage of combustion of methane[8]:

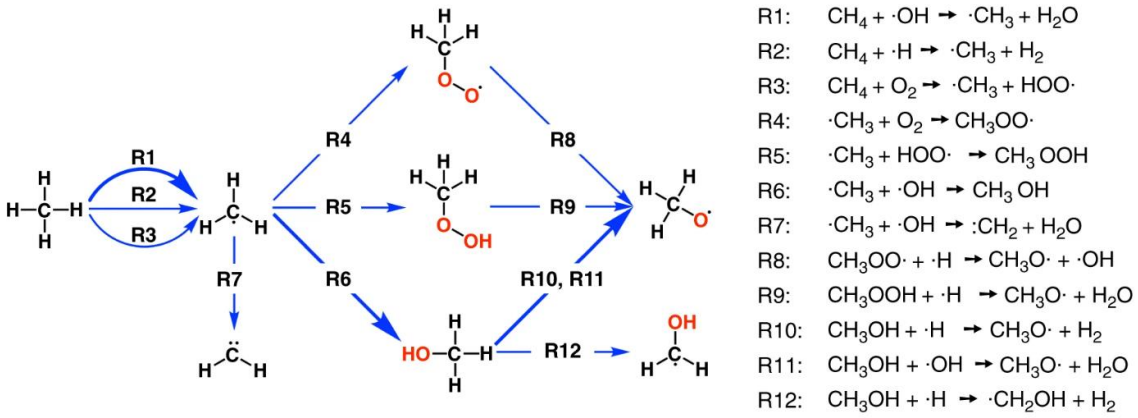

Figure 1.1 Initial stage of combustion of methane.

Source: [9]

Usually, temperatures of combustion reactions are greater than 500 K.

While at ambient temperature in the atmosphere (T = 300 K), H-abstraction occurs primarily by OH radicals.[10-12] A simplified atmospheric oxidation mechanism of n-Butane is shown below:[13]

$$C_3H_7CH_3 + \cdot OH \rightarrow C_3H_7CH_2\cdot + H_2O$$

$$C_3H_7CH_2\cdot + O_2 \rightarrow C_3H_7CH_2O_2\cdot$$

$$C_3H_7CH_2O_2\cdot + NO \rightarrow C_3H_7CH_2OONO\cdot$$

$$C_3H_7CH_2OONO\cdot \rightarrow C_3H_7CH_2O\cdot + NO_2$$

The above reactions show the initial steps of oxidation of n-Butane in the atmosphere. The H-abstraction could happen on other carbon atoms, too.[14] The oxidation process will continue to produce different products via different reaction pathways.

1.2.2 Organophosphorus Flame Retardants (OPFRs)

Organophosphorus flame retardants (OPFRs) are a class of chemical compounds that are commonly used as flame retardants in a variety of consumer products such as electronics, textiles, and furniture.[15, 16] These compounds contain phosphorus, carbon, and hydrogen atoms in their chemical structure, as shown in Figure 1.2. OPFRs work by reducing the flammability of materials and decreasing the rate at which flames spread (by reacting with the oxidizing radicals such as OH radicals). They do this by releasing phosphorus-containing gases that react with the radicals and other reactive species formed during the combustion process. These reactions effectively dilute and suppress the flame, thereby reducing the likelihood of a fire starting or spreading.

OPFRs have largely replaced the use of other classes of flame retardants such as polybrominated diphenyl ethers (PBDEs) and chlorinated organophosphates due to their perceived lower toxicity and greater effectiveness in preventing fires. However, concerns have been raised about the potential health and environmental impacts of OPFRs[16-18], and some studies have linked them to various adverse effects[19] including developmental and neurological toxicity, endocrine disruption, and environmental persistence.

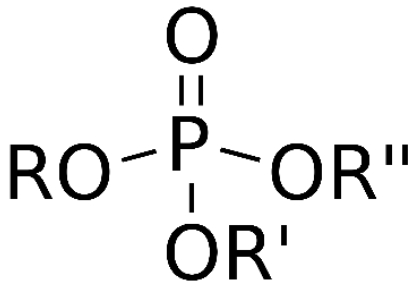

Figure 1.2 General chemical structure of an organophosphate.
Source:[20]

Their importance has significantly increased recently following the ban of polybrominated diphenyl ethers (PBDEs) in most countries. According to a market report published by Lucintel, the global organophosphorus flame retardants market was estimated as $2.0 billion annually today.[21, 22] Nowadays, there is an increasing concern for organophosphorus flame retardants due to their high production and usage volumes since they have been detected in various environmental matrices and have been identified as emerging contaminants. Studying their kinetics is very important for reactions in combustion and atmospheric environments. In both cases, the major oxidizing species for these compounds is hydroxyl radical, OH. However, very little data is available in the literature on the kinetics of these elementary reactions. The reaction between OPFRs and

the major oxidizing species, OH, is therefore very important in both atmospheric and combustive conditions.

$$OPFRs + OH \rightarrow Products \quad (1.1)$$

There is only one previous experimental work, where the rate constant of reaction (1.1) was measured using relative rate method, at a single (room) temperature.[23] As for the theoretical studies, there is only one theoretical work where an attempt was made to characterize the potential energy surface (PES) for this reaction using computational chemistry; subsequently the transition state theory was applied. Only one reaction channel was studied (H atom abstraction) in this theoretical paper, the temperature range was limited to 280 - 350K.[24]

In the initial study of the kinetics of reaction (1.1) performed by a collaborative group at the Institute of Chemical Kinetics and Combustion (IChK&C, Novosibirsk, Russian Federation), using the photolysis system based on the photolysis of ozone at 266 nm for the production of the excited oxygen atoms[25] with subsequent fast conversion to hydroxyl radicals in the reactions either with water or hydrogen molecules[26]:

$$O_3 + h\nu\ (266\ nm) \rightarrow O(^1D) + O_2 \quad (1.2)$$

$$O(^1D) + H_2O\ (or\ H_2) \rightarrow 2\ OH\ or\ OH + H \quad (1.3)$$

The reaction of generated OH radicals and Trimethyl Phosphate (TMP), one of the most common organophosphorus flame retardants, was studied in the temperature range of 273 – 470 K.

$$TMP + OH \rightarrow products \quad (1.4)$$

The highest temperature was limited by the thermal stability of ozone.[27] Despite the relatively narrow temperature range of this study, the results indicated that the temperature dependence is probably V-shaped, i.e., the rate constant decreases with temperature at low temperatures, and increases at higher temperatures. Therefore, the decision was made to significantly expand the temperature range using a different photolysis system, available at NJIT.

Photolysis of N_2O at 193 nm (ArF excimer laser) [28] was used since N_2O has much better thermal stability[29] compared with that of ozone. The replacement of excited oxygen atom allowed raising the upper temperature to 837 K.

$$N_2O + h\nu\ (193nm) \rightarrow O(^1D) + N_2 \qquad (1.5)$$

To obtain a time-resolved kinetic curve of reaction (1.4), a laser-pulsed photolysis-transient UV absorption technique was used. A high-pressure heatable configuration was set to control the reactor temperature and pressure.

1.2.3 Bimolecular elementary reactions

In 1889, the Arrhenius expression was first proposed by Svante Arrhenius to describe the temperature dependence of the rate of a chemical reaction. After then, a lot of efforts have been made to explain the meaning of the parameters in the Arrhenius expression. Based on different treatments and models, the development of kinetic theory includes the collision theory, ab initio molecular dynamics, transition state theory and RRKM theory. The collision model is the simplest one among these theories, although it is not accurate for complicated systems, some of its concepts are still very important.

Many reactions occur in a sequence of steps called elementary reactions, each step involves only a small number of molecules.[30] In a bimolecular reaction, a pair of molecules collide and exchange energy, atoms, or groups of atoms, or undergo some other changes.[31] A bimolecular elementary reaction has a second-order rate law:

$$A + B \rightarrow P \tag{1.7}$$

$$d[A]/dt = -k[A][B] \tag{E1.1}$$

"E" stands for "Equation" in "(E1.1)". This applies to all numerical equations throughout this work. Chemical equations are represented using only numbers.

Based on the assumptions of the collision theory, molecules must collide before they can react. This rule is fundamental to any analysis of an ordinary reaction mechanism. It explains why termolecular processes are so rare.[32, 33] A bimolecular reaction rate is proportional to the frequency of collisions between A and B, which in turn is proportional to their concentrations.

The collisional cross section is an "effective area" that quantifies the possibility of a scattering event when an incident species strikes a target species. In the hard sphere approximation, the cross section is the area of the conventional geometric cross section. The collisional cross sections typically denoted σ and measured in units of nm^2. The collisional cross section σ_{AB} between molecule A and molecule B can be calculated using the following equation:

$$\sigma_{AB} = \pi(r_A+r_B)^2 \tag{E1.2}$$

Based on the Maxwell-Boltzmann distribution of speeds, the mean speed, v_{mean}, of a molecule in the gas-phase can be calculated. Since the molecules are moving randomly towards all directions with different velocities, the mean relative speed, v_{real}, for two dissimilar molecules of masses m_A and m_B is:

$$v_{rel} = (8kt/\pi\mu)^{1/2} \quad \text{(E1.3)}$$

$$\mu = (m_A m_B)/(m_A + m_B) \quad \text{(E1.4)}$$

The collision frequency Z_{AB} can be derived from the collisional cross section σ_{AB} and the mean relative speed, v_{rel}.

$$Z_{AB} = \left\{\frac{8kT}{\pi\mu}\right\}^{1/2} N_A N_B \sigma_{AB} \quad \text{(E1.5)}$$

Where N_A and N_B are the number densities of A and B molecules in the system, k is the Boltzmann constant. A higher collision frequency should give a higher reaction rate, but not all collisions are effective in the reactions. If the reaction between A and B requires a significant disruption or rearrangement of the bonds between their atoms, the collision must be sufficiently energetic. Another requirement for complex molecules is the reactant species must be oriented in an appropriate manner for a particular process. These two requirements can be summarized as 1) The orientation of collision; 2) Activation energy.

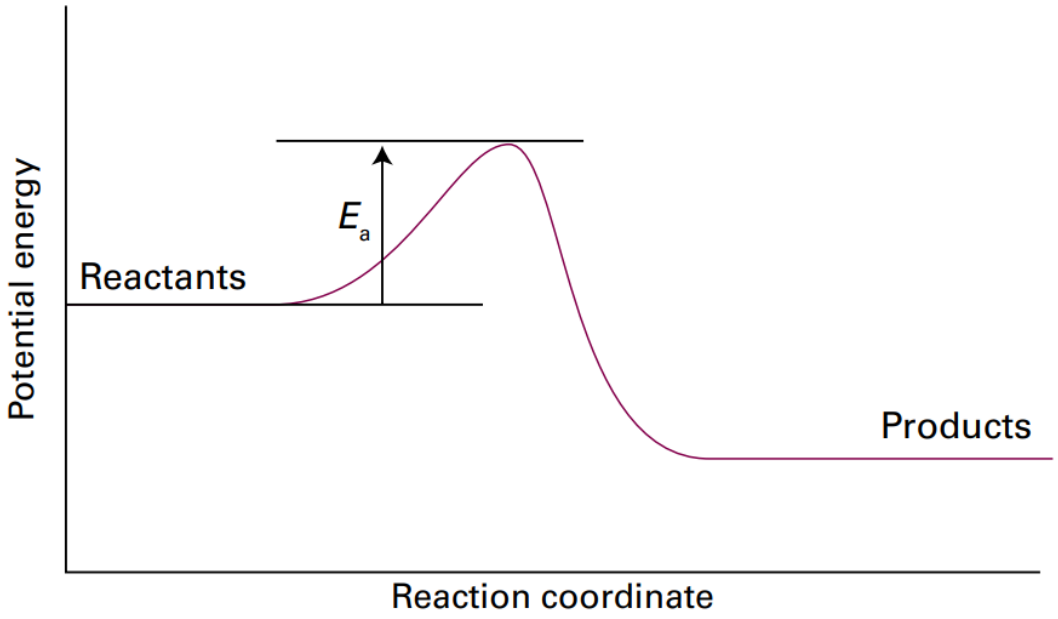

Figure 1.3 Energy change in the reaction path.
Source:[34]

Most reactions have a positive activation energy, as shown in Figure 1.3. The activation energy can be thought of as a barrier to the reaction, only those collisions with energies equal to or greater than the activation energy result in a reaction. The fraction of collisions with enough energy to overcome the activation barrier is given by:

$$f = e^{-Ea/RT} \quad \text{(E1.6)}$$

where: f is the fraction of collisions with enough energy, Ea is the activation energy (the reaction barrier).

The rate constant of the gas-phase reaction is proportional to the product of the collision frequency and the fraction of successful reactions. As stated above, sufficient kinetic energy is required for a successful reaction; however, they must also collide properly. Compare the following equation to the Arrhenius expression:

$$k = Z\rho e^{-Ea/RT} \quad \text{(E1.7)}$$

where: Z is the collision frequency, ρ is the steric factor.

Zρ is the pre-exponential factor, A, of the Arrhenius expression. In theory, it is the frequency of total collisions that collides with the right orientation. In practice, it is the pre-exponential factor that is directly determined by experiment and then used to calculate the steric factor.

In general, the pre-exponential factor A is not a constant. A modified Arrhenius expression may be introduced to account for this effect, i.e.,

$$k = BT^n e^{-Ea/RT} \quad \text{(E1.8)}$$

where: B is a constant and n is called the temperature exponent.

The collision theory provides a rough but apparent reaction diagram, it played an important role in the development of reaction kinetic theory. It explains a part of the experimental fact, the calculated rate constant fits the experimental data well for simple reactions, while this model involves the frequency factor, which is hard to calculate. Also, the activation energy needs to be obtained experimentally, so it is a semi-empirical model.

1.2.4 Potential Energy Surface (PES)

A potential energy surface (PES) describes the total energy of a system (excluding the kinetic energy of the nuclei), usually a collection of atoms, in terms of certain parameters, normally the position of the atoms (bond distance, bond angle, etc.). The surface might define the energy as a function of one or more coordinates. If there is only one coordinate, the surface is called a potential energy curve, such as the Morse potential. For a system

with two degrees of freedom, the value of the energy can be thought of as the height on a 2D planar surface defined by the two coordinates.

The geometry of a set of atoms can be described by a vector, **r**, whose elements represent the atom positions. The vector **r** could be the set of the Cartesian coordinates of the atoms or could also be a set of inter-atomic distances and angles. Given **r**, the energy as a function of the positions, V(**r**), gives the height on the "energy landscape" so that the concept of a potential energy surface arises. An example (Figure 1.4) is the PES for Li + HF → LiF + H, the energy varies as the distances between atoms change.[35]

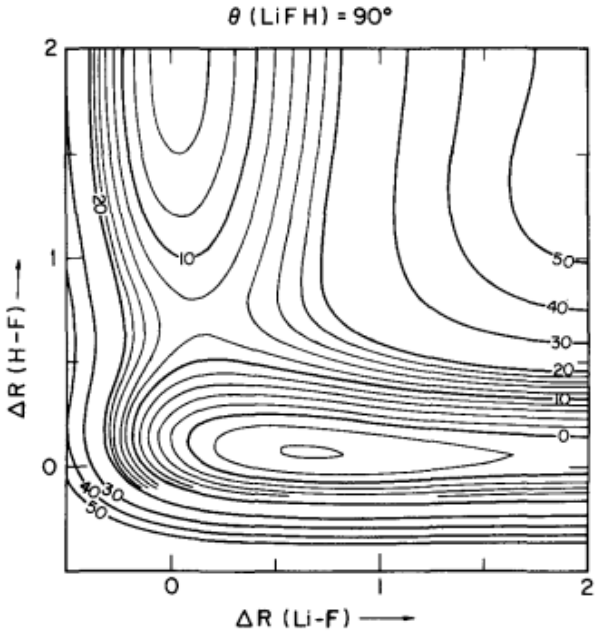

Figure 1.4 PES for Li + HF → LiF + H.
Source: [35]

The PES concept finds application in fields such as chemistry and physics, especially in the theoretical sub-branches of these subjects. It can be used to theoretically explore properties of structures composed of atoms, for example, finding the minimum energy shape of a molecule or computing the rates of a chemical reaction. The positions of

the minima on a potential energy surface which correspond to the reactant and product are called reactant/product valley. The reaction energy can be easily calculated from the energies or altitudes of the valleys for reactants and products.

In chemical reaction dynamics, once the necessary points are evaluated on a PES, the points can be classified according to the first and second derivatives of the energy with respect to position, which respectively are the gradient and the curvature. Stationary points on the PES have physical meaning: energy minima correspond to physically stable chemical species and saddle points correspond to transition states, the highest energy point on the reaction coordinate (which is the minimum energy pathway connecting a chemical reactant to a chemical product).

1.2.5 Transition State Theory (TST)

Chemical reactions can be thought of as the rearrangement of nuclear configurations from the reactant state to the product state. Since the complete description of a chemical reaction dynamics should include all possible paths, while mapping out a multidimensional potential energy surface is challenging, a simplified approach is commonly used, termed the transition state theory (TST).

$$\mathrm{A} + \mathrm{B} \rightarrow [AB]^{\neq} \rightarrow \text{Products} \tag{1.8}$$

The Eyring equation is an equation used in chemical kinetics to describe changes in the rate of a chemical reaction against temperature. It was developed almost simultaneously in 1935 by Henry Eyring, Meredith Gwynne Evans and Michael Polanyi.[36]

$$k = \kappa \frac{k_B T}{h} e^{-\triangle G^{\neq}/RT} \tag{E1.9}$$

Where $\triangle G^{\neq}$ is the Gibbs energy of activation, κ is the transmission coefficient, k_B is Boltzmann's constant, and h is Plank's constant.

Since $\triangle G^{\neq} = \triangle H^{\neq} - T \triangle S^{\neq}$, the rate constant expression can be expanded as:

$$k = \kappa \frac{k_B T}{h} e^{-\triangle H^{\neq}/RT} e^{\triangle S^{\neq}/R} \tag{E1.10}$$

An extra factor of $(c^{\Theta})^{1-m}$ is needed for correct dimensionality if the reactions are not unimolecular:

$$k = \kappa \frac{k_B T}{h} e^{-\triangle H^{\neq}/RT} e^{\triangle S^{\neq}/R} (c^{\Theta})^{1-m} \tag{E1.11}$$

Where (c^{Θ}) is the standard concentration 1M, m is the molecularity.

Classically, the fundamental assumption of TST is that there exists a hypersurface in the system phase space with two properties: (1) it divides space into a reactant region and a product region, (2) trajectories passing through this "dividing surface" in the production direction originated at reactants and will not reach the surface again before being thermalized or captured in a product state. The second part of the fundamental assumption is often called the no-recrossing assumption or the dynamical bottleneck assumption.[37]

TST has been widely used by researchers to understand qualitatively how chemical reactions take place, but it may fail in its simplest form. However, variational transition state theory (VTST) can provide a good description of a wide range of reactions. One reason why TST may fail is the tunneling effect. TST is based on classical mechanics, it is assumed that only the collision with enough energy to form a activated complex, can the reaction occur. While the quantum tunneling effect indicates that possibility always exists

if the barrier height is not infinite. This effect is not negligible when the barrier is relatively small, since the tunneling probability increases as the barrier decreases.[38]

In classical mechanics, TST provides an upper bound to the (classical) rate of a chemical reaction in terms of a flux integral over the dividing surface. The theory approximates the flux of reactive trajectories through the dividing surface by the total flux through the surface from reactant to product side. The accuracy of this approximation depends on the location of the dividing surface: The best surface is the surface that minimizes the transition state flux integral. Conventional TST is distinguished by placing the dividing surface at the saddle point and equating the net rate coefficient to the one-way flux coefficient.[39] VTST is distinguished by varying the definition of the dividing surface to minimize the one-way flux coefficient.[40]

1.2.6 Apparent Activation Energy (AAE)

The apparent activation energy (AAE) is an experimentally accessible value, it has played a central role in the field of reaction kinetics and mechanisms. It is typically measured by fitting the temperature dependence of the reaction rate to the Arrhenius expression.

Exothermic reactions between free radicals and molecules have been characterized by relatively small activation energy, but there are some reactions that involve a negative apparent activation energy.[41] Some of these kinds were studied using transition state theory by Benson[42, 43] since 1980s. The model indicates that there are a few bimolecular metathesis reactions that are expected to have a negative activation energy. Some features which have already been discussed are listed below:[44]

1) Two or more steps with two or more intervening transition state are involved, where the first step is the formation of a weakly bonded complex(chemical activation step).

2) They will be pressure-sensitive due to the deexcitation collision of the weakly bonded complex.

3) As the temperature increases, the vibrational energy contributes more to the second transition state, it even can change the sign of Ea.[43]

For bimolecular gas-phase reactions, negative activation energies and strongly curved Arrhenius plots may be explained by assuming that an intermediate complex is formed. As a result, at low temperature the average energy of the transition state will be less than that of the reactants and negative activation energy will be negative. As the temperature increases, the vibrational energy of the transition state becomes significant and the Arrhenius plot curves upward.[45] Benson and Dobis reviewed the mechanism of reactions proceeding via an intermediate complex and discussed the major features such as possible pressure dependence, the inverse isotope substitution effect, and possible inversion of the negative temperature dependence to a positive one at elevated temperatures.[42]

A modified transition state theory (MTST) was applied to a negative temperature dependent reaction, CH_3 + HBr(DBr) → CH_4(CH_3D) + Br, by Krasnoperov et al.[46] in 2005. The calculation revealed a transition state which is 2.3 KJ mol^{-1} lower than the ground state of the reactants, as well as the weakly bound complex. The "negative barrier", conservation of angular momentum, the centrifugal barrier at the entrance of the reaction valley, and the quantum effects of tunneling and above-the-barrier reflection are considered for the analytical expression, together with the potential energy surface at high level, a temperature dependent rate constant was obtained over a broad temperature range. The computed absolute rate constant shows a 'V-shaped' temperature dependence, which is shown in Figure 1.5.

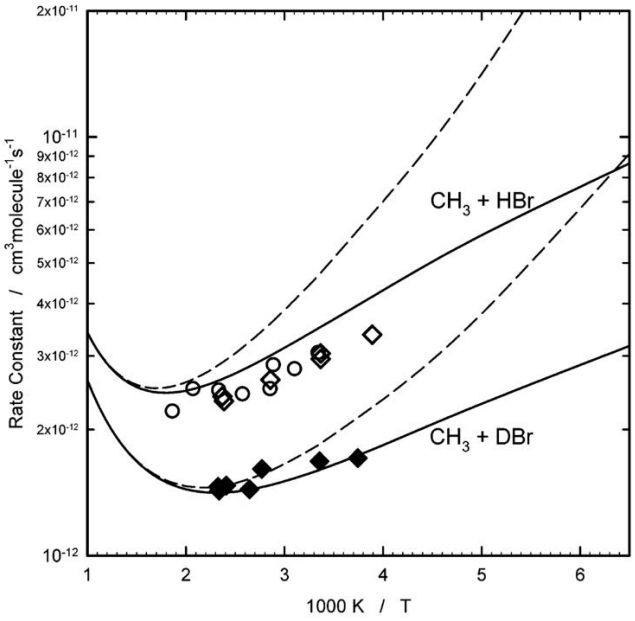

Figure 1.5 Computed result for the temperature dependent rate constant.
Source: [46]

Dashed lines in Figure 1.5 represent the result of the TST (with tunneling) with formally substituted negative barrier heights, corresponding to the high-pressure condition (fast energy relaxation on the time scale of passing from the entrance barrier to the transition state can be achieved, then the classical TST should become applicable). Solid lines are the calculation using modified TST, corresponding to the low-pressure condition, where the transition state is considered as sufficiently short-lived.

This comparison between solid lines (low pressure) and dashed lines (high pressure) shows a possible pressure dependence of the reactions with negative barriers. Large pressure effects are expected at lower temperatures (the difference between solid line and dashed line is larger when the temperature is low).

1.2.7 Pressure dependence of gas-phase reaction rates

Reactions proceeding via an excited intermediate should exhibit a pressure dependence due to collisional deexcitation of the intermediate. The pressure dependence of gas-phase reaction rates mainly arises from collisional energy transfer. This phenomenon can be described using simple consideration below.

Unimolecular Reactions

According to the Lindemann–Christiansen mechanism, unimolecular decomposition reactions (A → product) involving the following steps:

1. Collisional energy transfer between reactant and bath-gas (M) molecules
   - Collisional activation $A + M \rightarrow A^* + M$
   - Collisional deactivation $A^* + M \rightarrow A + M$
2. Intramolecular rearrangement
   - Molecular fragmentation $A^* \rightarrow$ product

The typical timescales of the collision processes and the reaction processes are significantly different (10^{-13} s and 10^{-9} s, respectively).[47] The overall rate has a dependence on bath-gas pressure. This dependence is governed by the competition between collisional energy transfer and intramolecular rearrangement processes, which results in three domains of pressure (as shown in Figure 1.6).

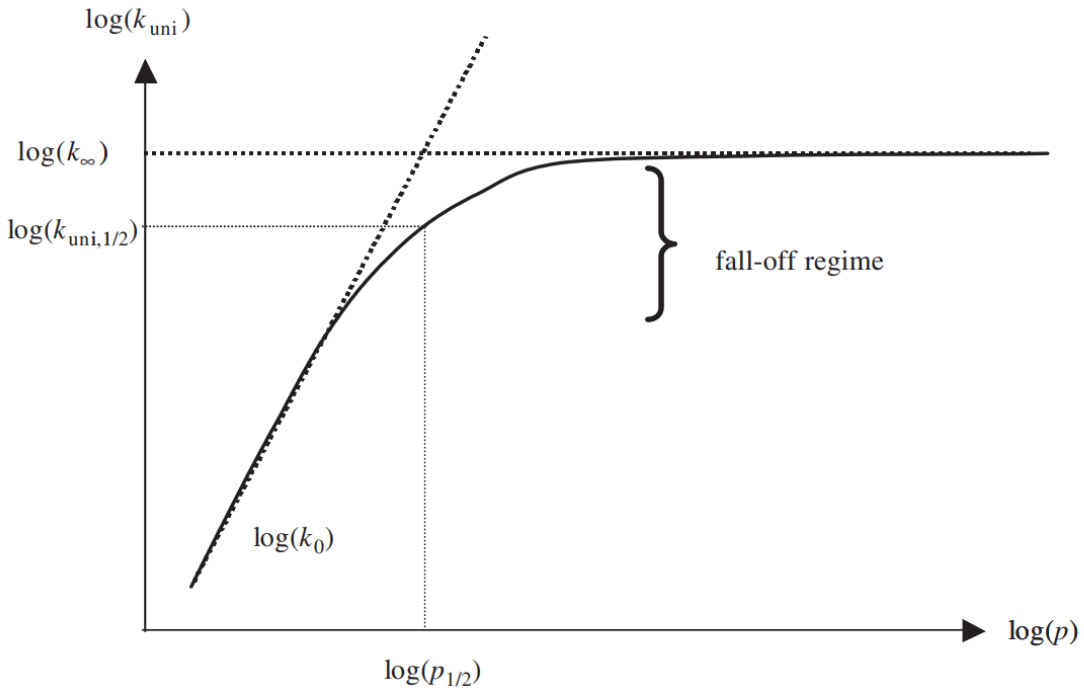

Figure 1.6 Typical pressure dependence of unimolecular reaction rate.
Source:[48]

High-pressure limit

At sufficiently high pressures, the number of collisions between reactant and bath-gas molecules is so large that energy and angular momentum populations maintain equilibrium Boltzmann distribution. The high-pressure rate coefficient is pressure-independent.

Low pressure limit

When the pressure decreases below a certain value of pressure, collisional activation and deactivation processes become rate limiting step, the rate coefficient is proportional to the bath-gas pressure.

Falloff region

The pressure domains that correspond to collisional energy transfer and intramolecular rearrangement overlap in the middle range domain of pressure. The pressure dependence of the reaction rate constant is no longer linear in this intermediate domain, this is referred to “falloff region”.

Bimolecular Reactions

For bimolecular reactions, only the association reactions that form vibrationally excited species leading to stable species by collision deactivation are pressure dependent.

- A + B → AB*

AB* can be stabilized by collision with some chemically inert species M (bath gas).

- AB* + M → AB + M

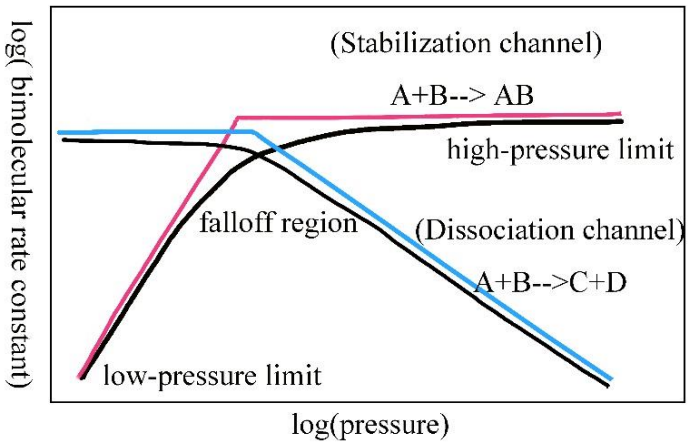

Figure 1.7 Typical pressure dependence of bimolecular reaction rate.
Source:[48]

The general pressure dependence behavior of bimolecular reactions is shown in Figure 1.7 for both the dissociation and stabilization channels.

Due to the making of new bond in the complex AB*, it may have a different chemical activation energy distribution. If this energy distribution extends above the barrier for new dissociations, these channels will be in competition with the collisional stabilization channel, resulting in a dropping line (blue) when the pressure is high.

CHAPTER 2

EXPERIMENTAL APPARATUS

2.1 General

The experimental method utilized excimer laser pulsed photolysis and UV-vis transient absorption spectroscopy, which were combined with both low and high-pressure flow systems. To initiate the reactions, the ArF excimer laser (Ex100 GAM Laser Inc., 193.3 nm) was used to photolyze the reactants. Additionally, various UV lamps were used, such as the Xe arc lamp (150 W, Oriel Instruments), the Hydroxyl lamp (H2O/Ar discharge lamp, homemade), the Hg arc lamp (500 W, Oriel Instruments), and a low-pressure radio frequency discharge Hg lamp (used to monitor free radicals and stable molecules by UV absorption).

To measure transient intensity at specific wavelengths, an imaging spectrograph (Acton Research Corporation SpectraPro – 300i), a photomultiplier tube (Hamamatsu R10699), a preamplifier (EMI) and a grated intensified CCD (ICCD) camera (ICCD Max, Roper Scientific) were combined. The heatable high-pressure flow reactor was made of 12.7 mm O.D. (1/2") stainless steel tubing and was placed in a cylindrical aluminum block with two electrical resistance heaters.

To trigger the oscilloscope (LeCroy 9310A, Dual channel, 400 MHz, 100 M samples/s, 50 K pts/ch), a pulse generator (BNC, model 555) triggered by the excimer laser was used. The traces were typically averaged for 500 to 3000 pulses by the oscilloscope and transferred to a PC for processing. Finally, nonlinear least squares fits were performed

using Origin software (Origin lab Corporation) in accordance with the reaction mechanism. An overall experimental configuration is shown in Figure 2.1.

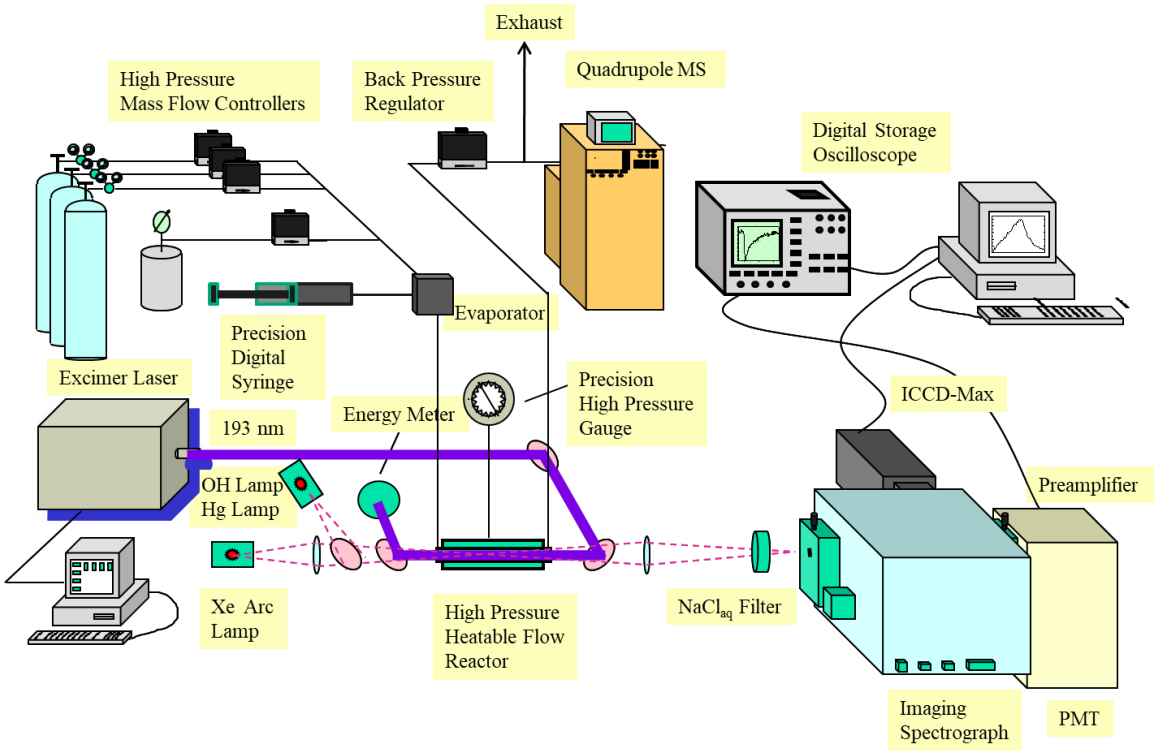

Figure 2.1 Experimental setup. Excimer laser pulsed photolysis coupled to UV-vis transient absorption spectroscopy and a high-pressure flow system.

2.2 Optics

The reactor was equipped with two UV-grade quartz windows (12.7 mm in diameter, 9.5 mm thick), which were sealed at the end of the reactor at ambient temperature outside the high-temperature zone using Viton O-rings. Two dichroic mirrors (CVI), which have high reflectivity at 193 nm and were mounted at an angle of 45^{o}, positioned before the entrance and after the exit of the flow reactor to allow for the merging of both the UV photolysis

beam and the monitoring beam in a single-pass configuration. The monitoring beam was formed by two diaphragms (1/4" diameter) located before and after the reactor.

Two dielectric mirrors with high reflectivity at 193 nm were installed after the Xe arc lamp at a 19^{o} incidence angle, which shift the high reflectivity range from the original 193 nm to the 200 – 230 nm region, attenuating the visible light from the Xe arc lamp by approximately 200 times. The original laser beam was expanded using a lens system consisting of a spherical lens (f = 30 cm) positioned at 70 cm from the reactor and a spherical lens (f = 30 cm) positioned at 23 cm from the reactor, to improve the homogeneity of the photolysis laser beam,

Spherical convex lenses were used to converge light from monitoring light sources. An additional liquid filter ($4.3x10^{-2}$ M NaCl aqueous solution, 1 cm) was installed before the entrance slit of the imaging spectrograph to provide complete suppression of scattered and back-reflected 193 nm laser light.

2.3 ArF Excimer Laser (193.3 nm)

The ArF excimer laser (Model EX100) from GAM Inc. produces unfocused light with a wavelength of 193.3 nm and a pulse duration of 20 ns. The laser beam was directed along the cell axis using a two-lens telescope and was reflected by a 45-degree dielectric mirror to fill the entire cross-section of the reactor. The laser energy was measured using an energy meter (Coherent, Max II) and a photodiode at the exit of the reactor, where it was reflected by the dielectric mirror. The laser repetition rate was adjusted to ensure complete replacement of the gas mixture inside the reactor between pulses, with a range of 0.1 - 2 Hz depending on the reaction conditions. The laser and optics were periodically aligned

and cleaned to maintain a good quality of the photolysis beam. The beam profile was measured by scanning with a small aperture diaphragm (approximately 0.5 mm, shown in Figure 2.2) and an energy meter. The beam uniformity across the reactor cross-section was ±7.3% from the mean value.

The overall design was to produce the radicals which are related to the target reaction, then fit the time-resolved absorption curves of this radial with our kinetic model, to determine the rate constant under different experimental conditions.

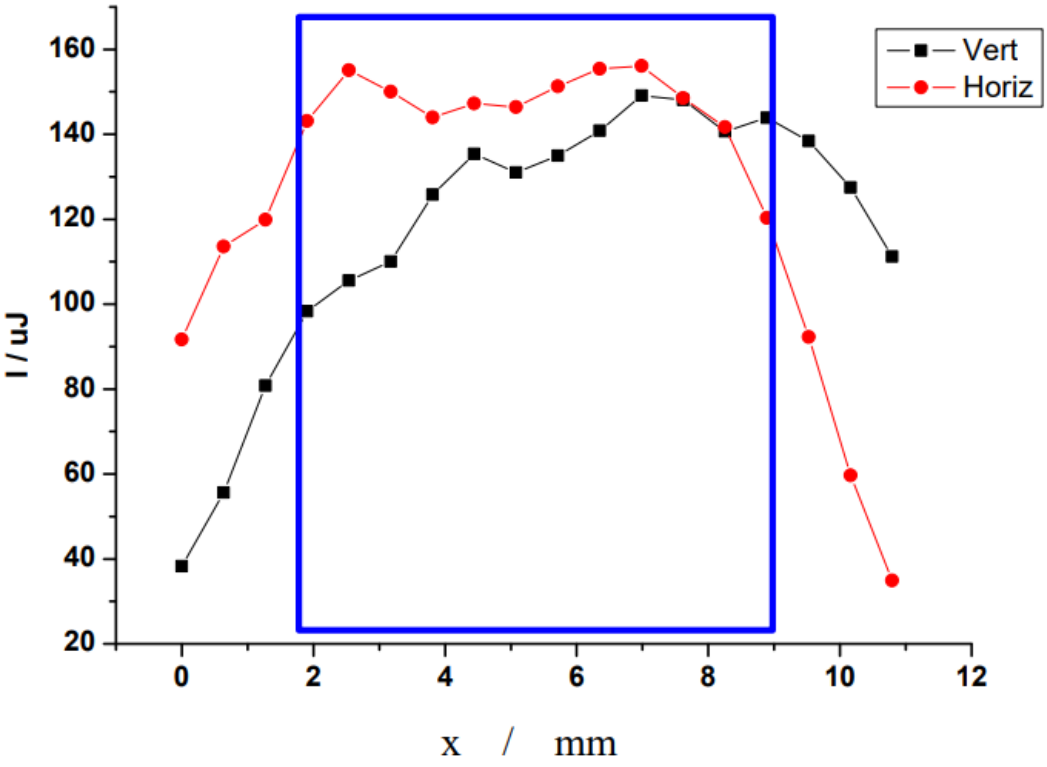

Figure 2.2 Laser intensity beam profiles across the cross-section of the reactor.

2.4 Heatable High-Pressure Reactor and Flow System

The high-pressure gas flow system with heating capabilities consists of various components, such as a heatable high-pressure reactor (Figure 2.3), high-pressure digital

syringes (Harvard Apparatus, Model PHD 4400), heatable transfer line, high-pressure mass flow controllers, high-pressure precision test gauges, high-pressure back pressure regulator, and helium cylinder.

The system was used for delivering liquid precursors through a capillary tube using a high-pressure precision digital syringe and an evaporator. The temperature of the evaporator was maintained at approximately 90 ℃, and a porous glass cap was installed at the end of the capillary inside the heated evaporator to ensure steady evaporation. This approach has been previously demonstrated to produce stable flows of liquid reactants mixtures over a pressure range of 1 - 100 bar.

Prior to loading into the stainless-steel syringe, the liquid solutions underwent a freeze-pump-thaw degassing procedure, which was typically repeated five times. The heated transfer line, which was positioned between the evaporator and the reactor, was utilized. When necessary, the temperature of the heated transfer line was increased to approximately 140°C to ensure a high concentration of water, particularly during high pressure measurements.

The high-pressure reactor used in this study was constructed using 12.7 mm O.D. (1/2”) stainless steel tubing, with an aluminum cylinder block covering the central portion of the tube for distributing heat. Two electrical resistance heaters were placed within the aluminum block, parallel to the reactor. The temperature profile of this reactor is shown in Figure 2.4. An additional heater was in the preheating unit (as indicated by the red dashed block in Figure 2.3). Two K-type thermocouples from Omega were installed, with one in the preheating unit and the other in the center of the aluminum block. The reactants were supplied through the stainless-steel tube located in the center of the reactor, with adequate

pre-heating. The preheating unit, which was approximately 15 cm in length, ensured that the gas mixture was fully preheated at the flow rates used in the experiments. The preheated reactant mixture entered the reactor at the center and exited through two outlets, located 5 cm from the center within the uniform temperature zone. Additional buffer gas flows were introduced into the reactor near the external windows to flush gas from the windows towards the outlets. Two additional thick (9.5 mm) magnesium fluoride (MgF_2) windows, separated by a stainless-steel insert, were placed without sealing inside the reactor near the reactor outlets. The active length of the reactor was determined by the length of the insert (10.0 cm), which prevented the reactants from penetrating outside of the active observation zone, providing precise definition of the observation zone within the uniform temperature region.

The gas flow rates were controlled by high pressure mass flow controllers (Brooks, 5850 TR series). To ensure accuracy, the controllers underwent periodic calibration using the soap film method.

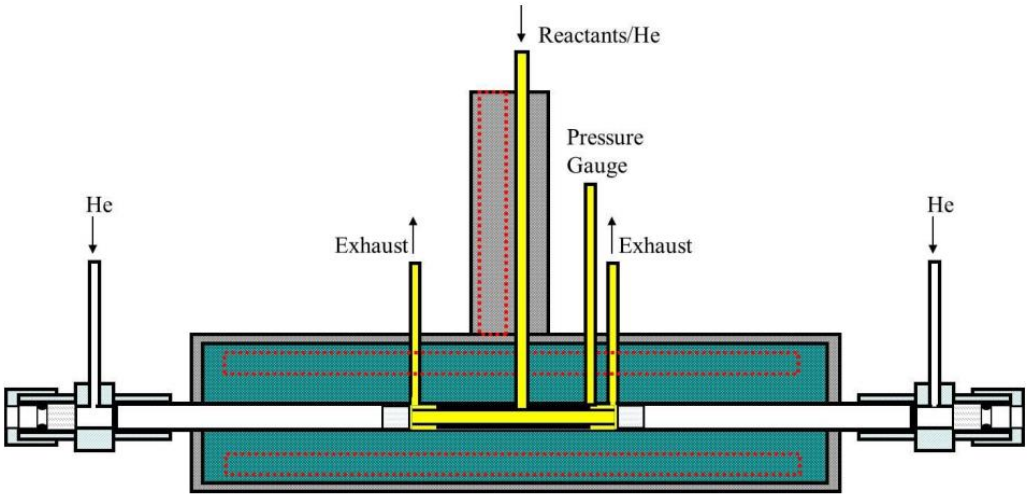

Figure 2.3 Detailed sketch of the heatable high-pressure flow reactor.

A high-pressure precision gauge was used to measure the pressure in the flow reactor (Matheson model 63 – 5633M, up to 250 bar pressure).

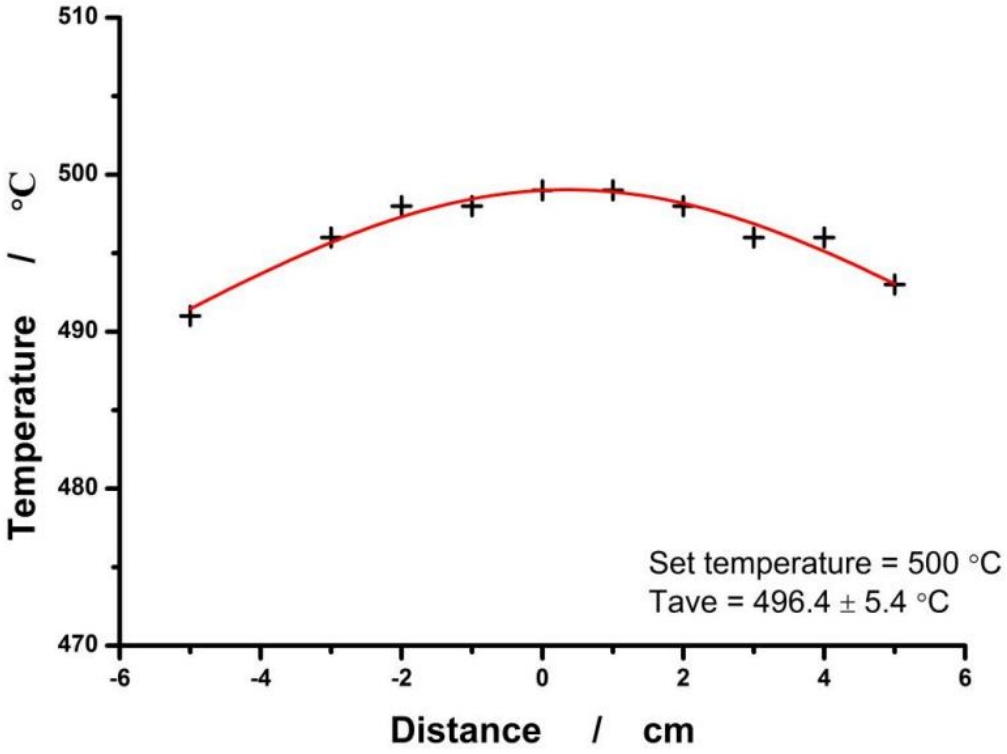

Figure 2.4 Temperature profiles of the heatable high-pressure flow reactor.

2.5 Generation of Hydroxyl (OH) Radicals

Hydroxyl radicals was generated using N_2O and water vapor, photolyzed by an ArF excimer laser at 193.3 nm:

$$N_2O + h\nu(193nm) \rightarrow O(^1D) + N_2 \quad (2.1a)$$

$$\rightarrow N(^4S) + NO(^2\Pi) \quad (2.1b)$$

$$O(^1D) + H_2O \rightarrow 2OH\ (v = 0.1) \quad (2.2a)$$

$$\rightarrow O(^3P) + H_2O \quad (2.2b)$$

$$\rightarrow H_2 + O_2 \quad (2.2c)$$

The quantum yield of the major channel 2.1a is 100% within the accuracy of 1 %; for the minor channel 2.1b, it is less than 0.8 %.[49]

The fraction of vibrationally excited hydroxyl radicals OH(v=1), formed in reaction $O(^1D)+H_2O$ (reaction 2.2a), is 22 - 24 %.

Fraction of $O(^1D)$, formed in photolysis of N_2O, reacts with N_2O:

$$O(^1D) + N_2O \rightarrow NO+NO \quad (2.3a)$$

$$\rightarrow O_2 + N_2 \quad (2.3b)$$

$$\rightarrow O(^3P) + N_2O \quad (2.3c)$$

The hydroxyl radical temporal profiles were recorded via multiline UV absorption at ca. 308 nm using low-pressure H_2O/Ar DC discharge lamp.

2.6 Thermal Stability of Reactants

Nitrous oxide (N_2O) would undergo spontaneous thermal decomposition at 1200 K (without catalysts).[50] While the aluminum would melt at 933 K. To keep the reactor and the supporting base from melting down, a lower temperature, 837 K, was set as the upper limit in the temperature dependent measurements. This temperature limit was also used in previous research conducted by our group.

2.7 UV Absorption Spectroscopy

Various light sources, including a 150 W Xe arc lamp (Oriel Instruments), a homemade H_2O/Ar discharge lamp, a 500 W Hg arc lamp (Oriel Instruments), and a low-pressure RF discharge Hg lamp, were utilized for both single-wavelength and spectral measurements of transient absorption.

The Acton Research Corporation SpectraPro-300i imaging spectrograph was utilized in conjunction with a photomultiplier tube (PMT) (Hamamatsu R10699), preamplifier (EMI), and gated intensified CCD (ICCD) camera (ICCD Max, Roper Scientific) to perform measurements of transient absorption at single wavelengths, as well as measurements of transient absorption spectra. To ensure good linearity and lower noise at high photon fluxes, the photomultiplier tube, mounted on the exit slit, operated on a reduced number of dynodes with a voltage divider current of 2.7 mA. Residual light from the excimer laser pulse was eliminated by utilizing a NaCl aqueous solution ($4.3x10^{-2}$ M solution NaCl in water, 1 cm). The PMT signal was then amplified, digitized, and stored via a digital storage oscilloscope (LeCroy 9310A, Dual channel, 400 MHz, 100 M samples/s, 50 K pts/ch). The time resolution was determined by the preamplifier setting, which could be 30 ns, 0.3 us, 3us, or 30 us. Since free radicals' lifetime in this study was generally shorter than 1 ms, a 0.3 μs time constant was used. The signal, typically averaged as 500 - 5000 pulses, was subsequently transferred to a PC for further processing and fitting.

During all measurements, the light intensity traces of monitoring were also collected without the precursor molecules (N_2O or H_2O) present. These traces were then subtracted from the traces collected with the presence of the precursors to create a 'zero shift'. This was done to eliminate the effect of changes in monitoring light intensity on the

multilayer mirrors caused by water release from the porous layers of multilayer coating and slight temperature changes in the mirror coatings. These factors result in small changes in the indexes of refraction of the coating layers materials and subsequently, in modulation of the mirror's reflectivity. The “zero shift” could be either negative or positive depending on the spectral separation of the monitoring wavelength from the wavelength of the maximum reflectivity of the mirrors. This was observed in all experiments using the same approach of merging the photolysis and monitoring beams. The typical scale of the “zero shift” in this study was approximately 4×10^{-4}. Additionally, subtracting the “zero shift” trace eliminated a slight distortion after the large spike caused by the luminescence of the reactor windows (of a similar scale, $(2 – 4) \times 10^{-4}$).

The decay curves of hydroxyl radicals (OH) were observed through absorption in the UV (with multiline at approximately 308 nm), using a DC driven low-pressure resonance hydroxyl lamp. The absorption cross sections of hydroxyl are dependent on the gas temperature and pressure within the lamp, which in this case was Argon flow that was saturated with water vapor at an absolute pressure of 1.28 atm and ambient temperature of 296 ± 3 K. To interpolate the data and evaluate the "curve of growth", a spectroscopic model was created in a prior study. The hydroxyl radical decays were detected using a DC discharge H_2O/Ar low-pressure resonance lamp and an imaging spectrometer (Acton 300i), with absorption at 308 nm (150 groove/mm grating, 300 mm focal length, both slits 0.5 mm, triangle slit function, FWHM = 10.7 nm).

2.8 In Situ Actinometry

Accurately determining the absolute concentrations of OH radicals is critical for understanding the reactions investigated in this study. To achieve this, the photon fluence was determined through in situ actinometry, which involved measuring the ozone produced during the photolysis of $N_2O/O_2/N_2$ mixtures.

In our measurements, a gas mixture containing 2.5% N_2O in helium and 8.0% O_2 in nitrogen was passed through the reactor at ambient pressure and photolyzed at a wavelength of 193.3 nm. The excited oxygen atoms $O(^1D)$ produced during photolysis underwent relaxation either through collisions with nitrogen ($k_{q,N2} = 2.6x10^{-11}$) and oxygen ($k_{q,O2} = 4.0x10^{-11}$) or through reaction with N_2O ($k_{q,N2O} = 1.35 \times 10^{-10}$). The concentration of the oxygen-nitrogen mixture (2.43×10^{19} molecule cm^{-3}) was significantly higher than the concentration of N_2O used in this experiment (7.4×10^{16} molecule cm^{-3}), which led to almost complete relaxation (97.4%) of $O(^1D)$ to the ground state oxygen atoms $O(^3P)$ and their subsequent conversion to ozone in a fast reaction (about 56 microseconds) with molecular oxygen. The formation of O_3 was monitored using a low-pressure RF discharge mercury lamp at 253.7 nm.

To determine the absolute concentrations of radicals in our experiments, we utilized several factors: the photon flux inside the reactor, the absorption cross-section of N_2O at 193.3 nm, and the efficiency of the conversion of $O(^1D)$ atoms produced during the photolysis of N_2O to these radicals. The absorption cross-section of N_2O is well-known at a temperature of 298 K and a pressure of 1 bar. In our specific case, we monitored ozone formation at 253.7 nm during the photolysis of $N_2O/O_2/N_2$ mixtures at 1 bar and 298 K to aid in our determination.

The concentration of ozone formed was calculated by taking the difference in absorbance between samples with or without the reactant (Only the initial parts of the traces are shown to resolve the build-up stage. In the measurements, a longer time domain (ca. 5 ms) is used).

Sample ozone formation traces are shown in Figure 2.5 with the mixture $N_2O/O_2/N_2$ (N_2O = 2.42 Torr, 8.0% O_2/N_2 mixture, total pressure 1 bar) in the reactor (between the two internal windows). In the blank experiment, where the reactants were absent, the flow of N_2O/He was turned off, and only the O_2/N_2 mixture was pumped through the reactor. The residual absorbance in the blank experiment was due to the photolysis of molecular oxygen inside the reactor and between the external and internal windows flushed with the O_2/N_2 mixture.

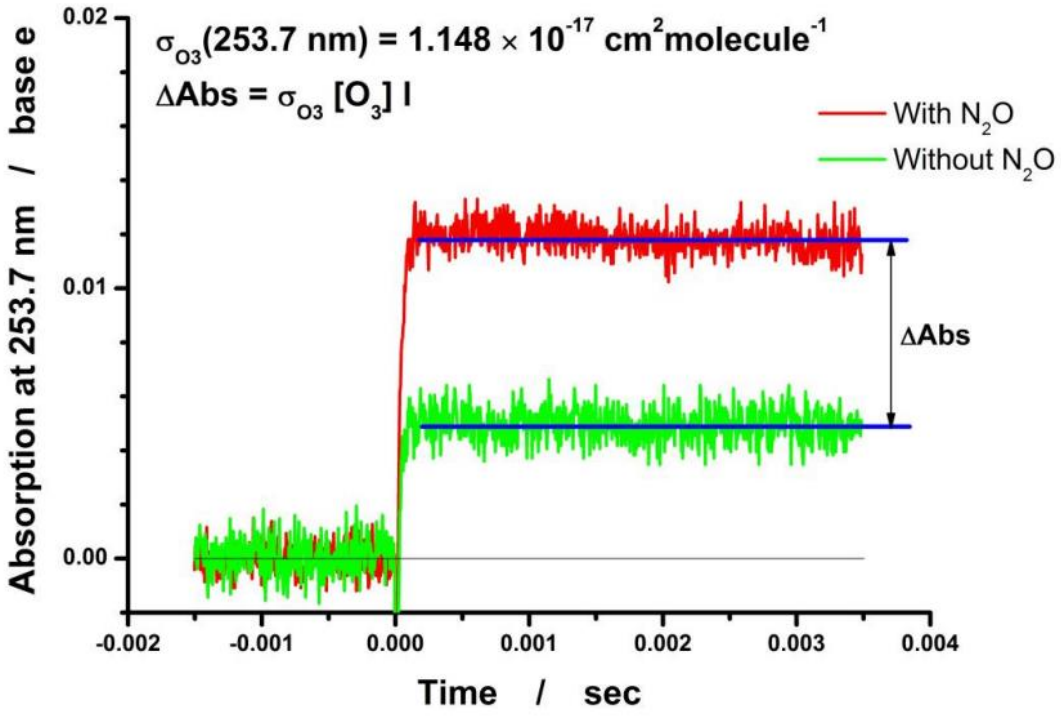

Figure 2.5 In situ actinometry based on the ozone formation.

The difference in the absorbance, ΔAbs, was used to calculate the concentration of ozone formed due to the photolysis of N_2O. The photon fluence, F (photons cm^{-2}) was then calculated as:

$$F = \frac{\Delta Abs}{\sigma(O3) \cdot l \cdot 0.985 \cdot \sigma(N2O) \cdot [N2O]} \quad \text{(E2.1)}$$

where $\sigma(O_3) = (1.148 \pm 0.034) \times 10^{-17}$ cm^2 $molecule^{-1}$ is the ozone absorption cross section at 253.7 nm; l = 10.00 cm is the length of the reactor (the distance between the two internal windows), and $\sigma(N_2O) = (8.77 \pm 0.44) \times 10^{-20}$ cm^2 $molecule^{-1}$ is the N_2O absorption cross section at 193.3 nm (all at 298 K and 1 bar). Two such determinations were performed, both before and after a series of measurements.

CHAPTER 3

OH + OH

3.1 Introduction

The hydroxyl radical is significant in both combustion reactions[1, 51, 52] and the atmospheric environment[53-57]. Its self-reaction is crucial in laboratory studies of other reactions involving this intermediate, and it also plays a fundamental role in chemical kinetics as one of the simplest self-reactions of diatomic free radicals：

$$OH + OH \rightarrow H_2O + O \quad (3.1a)$$

$$\rightarrow H_2O_2 \quad (3.1b)$$

Reaction 3.1 is one of the ways in which hydroxyl radicals are consumed in the reaction mechanism, and it results in the production of oxygen atoms. However, this leads to the generation of hydrogen atoms through subsequent reactions with hydroxyl radicals, which makes the interpretation of data more complex. To accurately interpret laboratory data, it is essential to have precise rate constants and branching ratios, along with their temperature dependences across a wide range of temperatures and pressures.

Several publications[29, 58] have thoroughly investigated Reaction 3.1 both experimentally[59-67] and theoretically[68-71]. The temperature dependence of the disproportionation channel 3.1a has been found to be negative (meaning a slower reaction at higher temperatures) at ambient and slightly elevated temperatures, with one old experimental study reporting a positive temperature dependence[66]. However, subsequent experimental studies have confirmed a small negative temperature dependence near

ambient conditions[72]. As of now, the negative temperature dependence of the disproportionation channel 3.1a at ambient and slightly elevated temperatures is well-established.

Although there have been numerous experimental studies on the kinetics of Reaction 3.1, the absolute value of the rate constant for the disproportionation channel 3.1a, even at ambient temperature, is still a topic of debate.

The current IUPAC recommendations accept the room-temperature rate constant of the disproportionation channel 3.1a, $k_{3.1a} = 1.48 \times 10^{-12}$ cm^3 molecule^{-1} s^{-1}, obtained using a discharge flow system, as well as the negative temperature dependence at moderate temperatures.[73, 74] However, a later study reinvestigated channel 3.1a using pulsed laser-photolysis of N_2O/H_2O mixtures at 193 nm and obtained a factor of approximately 1.8 higher value of 2.7×10^{-12} cm^3 molecule^{-1} s^{-1}.[58] The kinetics of reaction 3.1 were also investigated using photolysis of $N_2O/H_2O/O_2$ at 193nm at high pressures, where the production of ozone formed in the recombination of oxygen atoms produced in channel 3.1a with molecular oxygen was monitored.[29] This study confirmed the lower value of $k_{3.1a}$ at ambient temperature and reported a turning point in its temperature dependence at around 500 K. In the most recent study, essentially the same approach as in the previous study by the same group[58] was used, but a modified heatable reactor was employed, yielding a high value of $k_{3.1a}$ again while confirming the turning point in its temperature dependence at around 500 K.

In this work, the kinetics of the title reaction was investigated at ambient temperature and low pressures (no more than 1 atm). Laser photolysis−time-resolved transient UV absorption of OH at ca. 308 nm allowed us to monitor the decay kinetics.

Photolysis of $N_2O/H_2O/He$ was used to produce excited $O(^1D)$ atoms, subsequently, excited oxygen atoms produce OH radicals via fast reaction with water molecules:

$$O(^1D) + H_2O \rightarrow 2\ OH \qquad (3.2)$$

3.2 Experimental Approach

Pulsed-laser photolysis combined with transient UV absorption was used in the studies. The detailed experimental setup and the design of the flow reactor was described before.[49] A low-pressure reactor diagram is shown in Figure 3.1. A vacuum pump (Agilent Technologies, SH-110 Dry Scroll Vacuum Pump) combined with a set of control valves were used to achieve designated low-pressure conditions. The exact pressure was determined by a set of calibrated pressure gauges.

There were two different variables in this work, one is the laser energy passed through the reactor, which was controlled by a set of meshes; the other is the ratio of N_2O/H_2O, which was controlled by the mass flow controller of N_2O and the infuse rate of liquid H_2O. A single mesh or combined meshes were placed before the entrance of the reactor, so a 10% - 100% laser intensity can be achieved inside the reactor. Since the concentration of OH radical is proportional to the laser intensity, the concentration of OH radical was varied from 10% - 100%.

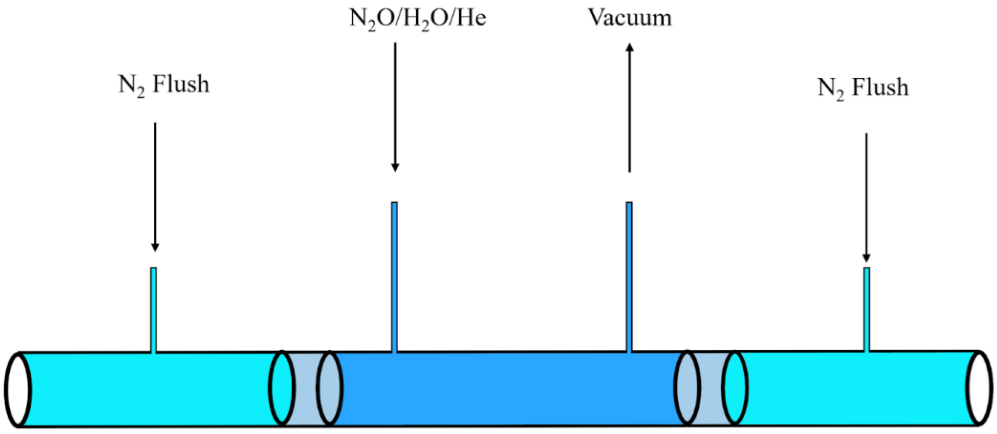

Figure 3.1 Low-pressure reactor diagram.

3.3 OH Radical Absorption Cross-section

OH radical has strong absorption lines near 308 nm. Figure 3.2 shows the simulated absorption spectrum of OH using LFFBASE software.

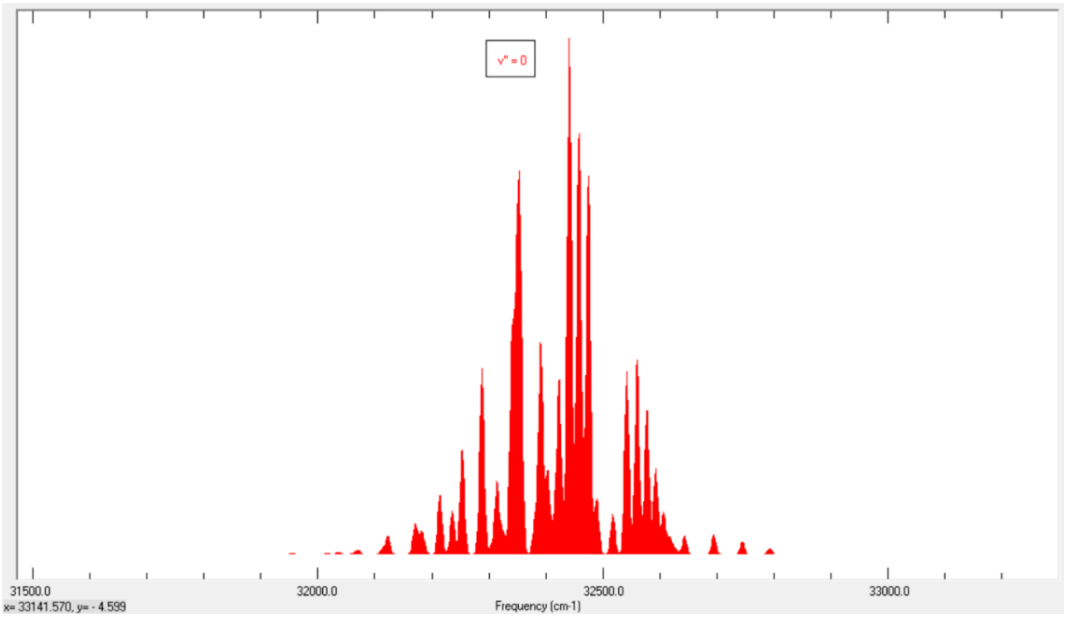

Figure 3.2 Absorption spectra of OH radical (simulated using LIFBASE).

It should be noted that the apparent absorption cross section of OH radical is temperature and pressure dependent, so a small adjustment was introduced to accommodate different reaction conditions. These dependencies were studied well in previous publications, where the ratio of the apparent cross-section, (defined as $\sigma_{app} = \ln(I_0/I)/([OH]*l]$) and the apparent cross-section in the limit of very small absorptions, $\sigma_{app,0}$, is plotted vs. the apparent absorbance, $\ln(I_0/I)$. This representation allows simple correction of the observed absorbance profiles. The deviations from Beer-Lambert law are linear with high accuracy when apparent absorbance does not exceed 15%, and can be expressed as:

$$A_{app}/A_{app,0} = \sigma_{app}/\sigma_{app,0} = 1 - S * A_{app} \qquad \text{(E3.1)}$$

where S is the slope of the ratio $\sigma_{app}/\sigma_{app,0}$ plotted vs. A_{app}. The values of the slope at 300 K are shown in Figure 3.3.

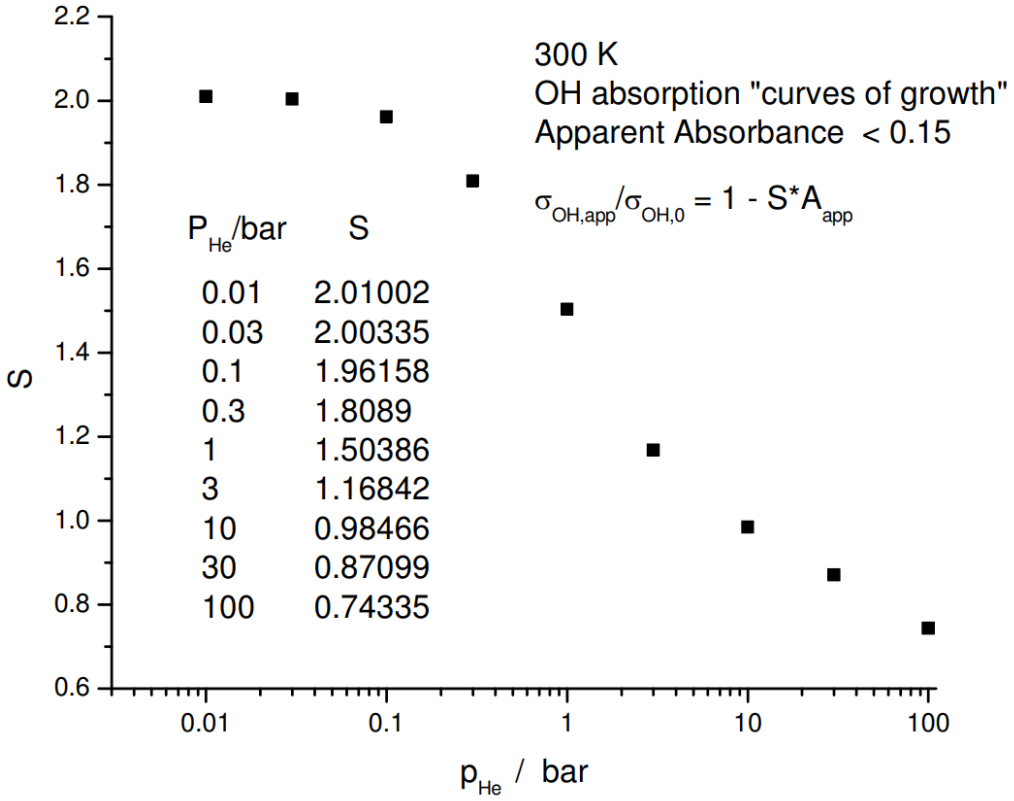

Figure 3.3 Pressure dependent S value from 0.01 – 100 bar, at 300 K.
Source:[29]

The slopes S from (E3.1) obtained using linear regression over the 0 – 15% range of the apparent absorbances are listed in Table 3.1. For different reaction conditions, corresponding S value was used to calculate the apparent absorption in the limit of very small absorptions.

Table 3.1 The Slopes of The Dependences of $\sigma_{OH,app}/\sigma_{OH,0}$ vs. The Apparent Absorbance ($A_{app} = \ln(I_0/I)$) at Different Pressures and Temperatures

T/K	0.01 bar	0.1 bar	1 bar	3 bar	10 bar	30 bar	100 bar
298	2.01	1.98	1.56	1.29	1	0.89	0.76
354	1.64	1.62	1.29	1.07	0.84	0.75	0.65
400	1.34	1.32	1.08	0.89	0.7	0.64	0.57
414	1.29	1.27	1.04	0.86	0.68	0.62	0.55
500	0.99	0.97	0.82	0.69	0.54	0.5	0.45
555	0.87	0.86	0.73	0.61	0.48	0.45	0.4
600	0.76	0.76	0.65	0.55	0.43	0.4	0.37
626	0.73	0.72	0.62	0.52	0.42	0.39	0.36
700	0.62	0.61	0.54	0.45	0.36	0.34	0.31
714	0.6	0.6	0.53	0.44	0.35	0.33	0.31
769	0.55	0.54	0.48	0.41	0.33	0.31	0.29
800	0.52	0.51	0.46	0.39	0.31	0.29	0.27
834	0.49	0.49	0.44	0.38	0.3	0.28	0.26
900	0.44	0.44	0.4	0.37	0.27	0.26	0.24

3.4 Results and Discussion

Radicals' concentration traces were normally averaged for 500 to 5000 times by oscilloscope and transferred to a PC for processing. The profiles transferred from PC were fitted using a smooth function with enough parameters to provide adequate fitting flexibility. SCIENTIST software (Micro Math, Inc.) was used to perform the nonlinear least squares fitted by numerical solutions of the ODE system which corresponds to the reaction mechanism. The model was constructed in SCIENTIST software and listed in Appendix. The reaction mechanisms used to fit are listed in Table 3.2. (Rate constant and concentrations' unit is based on molecule, cm^3, sec. Temperature is in K.)

Table 3.2 Reaction Mechanism Used for Fitting the Experimental Absorption Profiles

Reactants	**Products**	**Rate Constant**	**Reference**	**Comments**
OH+OH	$O+H_2O$	This work		
	H_2O_2	$k_0=9.0 \times 10^{-31}(T/300)^{-3.5}$ $k_{inf}=2.4 \times 10^{-11}(T/300)^{-0.5}$ $F_{cent}=0.37$	Ref.[29]	
$O+O_2$	O_3	$3.4 \times 10^{-34}(T/300)^{-1.2}$	Ref.[75]	
$O(^1D)+H_2O$	OH+OH	$1.7 \times 10^{-10}\exp(36/T)$	Ref.[76]	
	$O(^3P)+H_2O$	$< 0.003\ k_{2.2a}$	Ref.[77]	neglected
	H_2+O_2	2.2×10^{-12}	Ref.[73]	
$O(^1D)+N_2O$	NO+NO	8.37×10^{-11}	Branching ratio = 0.62. Ref.[73]	Total rate constant[58] k = 1.35×10^{-10} is the average value in three studies.[78-80]
	O_2+N_2	5.31×10^{-11}	Branching ratio = 0.62. Ref.[73]	
	$O(^3P)+N_2O$	1.3×10^{-12}	Ref.[76]	
OH+O	O_2+H	$2.4 \times 10^{-11}\exp(110/T)$	Ref.[73]	
	HO_2	$1.6 \times 10^{-31}\ (T/298)^{-2.6}$	Ref.[81]	
$H+O_2$	OH+O	$1.62 \times 10^{-10}\exp(-7470/T)$	Ref.[82]	
	HO_2	$1.8 \times 10^{-32}(T/298)$	Ref.[83]	
HO_2+O_2	$OH+O_3$	0		Endothermic, neglected
$OH+O_3$	HO_2+O_2	$1.7 \times 10^{-12}\exp(-940/T)$	Ref.[73]	
$O+O_3$	O_2+O_2	$8.0 \times 10^{-12}\exp(-2060/T)$	Ref.[73]	
$H+O_3$	$OH+O_2$	$1.4 \times 10^{-10}\exp(480/T)$	Ref.[80]	
HO_2+O_3	$OH+O_2+O_2$	$1.97 \times 10^{-16} \times (T/298)^{4.57}$ $\exp(693/T)$	Ref.[73]	
OH+H	H_2+O	$6.86 \times 10^{-14}(T/298)^{2.8}$ $\exp(-1950/T)$	Ref.[84]	
	H_2O	$1.6 \times 10^{-31}\ (T/298)^{-2.6}$	Ref.[81]	
OH+NO	HONO	$k_0=6.0 \times 10^{-31}(T/300)^{-2.5}$ $k_{inf}=3.3 \times 10^{-11}(T/300)^{-0.3}$ $F_{cent}= 0.60\ \exp(91/T)$	Ref.[85]	
$OH+HO_2$	H_2O+O_2	$4.8 \times 10^{-11}\exp(250/T)$	Ref.[86]	
HO_2+NO	$OH+NO_2$	$4.0 \times 10^{-12}\exp(223/T)$		Computed using SCIENTIST (Micro math software)
$OH+H_2O_2$	H_2O+HO_2	$2.9 \times 10^{-12}\exp(-109/T)$	Ref.[87]	
$O+HO_2$	$OH+O_2$	$2.7 \times 10^{-11}\exp(224/T)$	Ref.[73]	
$O+H_2O_2$	$OH+HO_2$	$1.40 \times 10^{-12}\exp(-2000/T)$	Ref.[73]	
$H+HO_2$	H_2+O_2	$7.11 \times 10^{-11}\exp(-710/T)$	Ref.[88]	
	OH+OH	$2.81 \times 10^{-10}\exp(-440/T)$	Ref.[88]	
	H_2O+O	$5 \times 10^{-11}\exp(-866/T)$	Ref.[88]	
	$H_2O+O(^1D)$	$3.29 \times 10^{-12}(T/298)^{1.55}\ \exp(81/T)$	Ref.[89]	

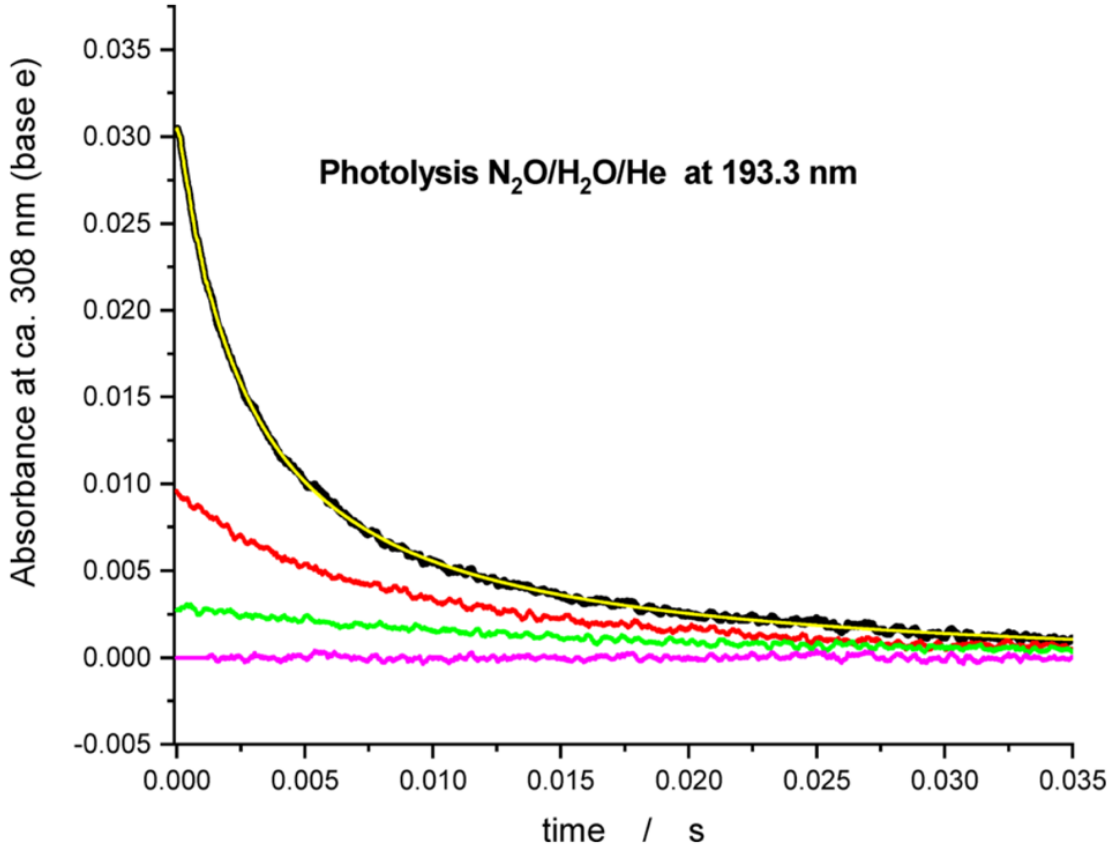

Figure 3.4 Sample UV absorption profiles of OH radical (multiline at ca. 308 nm). Photolysis of N_2O/H_2O/He mixture at 193.3 nm. T = 295 K, p = 0.01 bar (7.51 Torr).

The reactants' concentrations in Figure 3.4 are: $[N_2O] = 1.54 \times 10^{16}$ molecules cm^{-3} , $H_2O = 1.57 \times 10^{17}$ molecules cm^{-3} , $[N_2O]/[H_2O] = 0.1$. The initial concentration of OH is varied by the laser light attenuation. Wall coating is PFPE (Krytox 1525). Black−experimental curve, yellow−fitting, magenta−the residual of the fit. The red and green curves are the experimental profiles obtained at the same experimental conditions using attenuated laser light.

The concentrations of reactants (N_2O, H_2O and He) were maintained constant, while the laser light was attenuated using meshes and quartz plates to adjust the initial

concentration of OH radicals. The decay curves from 1.2 ms until approximately one-third of the amplitude decay were fitted with an exponential function to determine the "initial slope" rate constant. The results show that the intercept = 35.4 s^{-1} , the calculated wash-out time = 145 cm/s/10 cm = 14.5 s^{-1} , then the first approximation for $k_{w,OH}$ = 21 s^{-1}. Assuming the apparent stoichiometric coefficient of 3.37 for these experimental conditions (obtained using modeling of the kinetic absorption profiles using the complete model), the first approximation rate constant for channel 3.1a is $k_{3.1a} = 1.40 \times 10^{-12}$ cm^3 $molecule^{-1}$ s^{-1}.

The absorption profiles of OH radicals at various initial concentrations were fitted using the full kinetic model by solving the ODE system corresponding to the reaction mechanism through SCIENTIST software. The first approximation wall rate constant obtained from the initial slope analysis was incorporated into the reaction model, and the wash-out contribution was accurately included in the fitting model. The obtained product $k_{3.1a}[OH]_{ini}$ is plotted versus the $[OH]_{ini}$, and the intercept was adjusted until it became zero, thereby determining the wall decay rate constant, $k_{w,OH}$. In this example, the process converged in two additional steps beyond the initial slope analysis, resulting in a rate constant of $k_{3.1a} = 1.39 \times 10^{-12}$ cm^3 $molecule^{-1}$ s^{-1}, and a wall loss rate constant for hydroxyl radicals of $k_{w,OH}$ = 28 s^{-1}. It is noteworthy that although all pertinent reactions were considered in the mechanism, only four reactions accounted for 93% of the returned rate constant $k_{3.1a}$, which include the two channels of reaction 3.1, reaction of oxygen atoms with OH, and the wall reaction of hydroxyl radicals. Adding all other processes in the reaction mechanism produced a correction that did not exceed 7% of the rate constant.

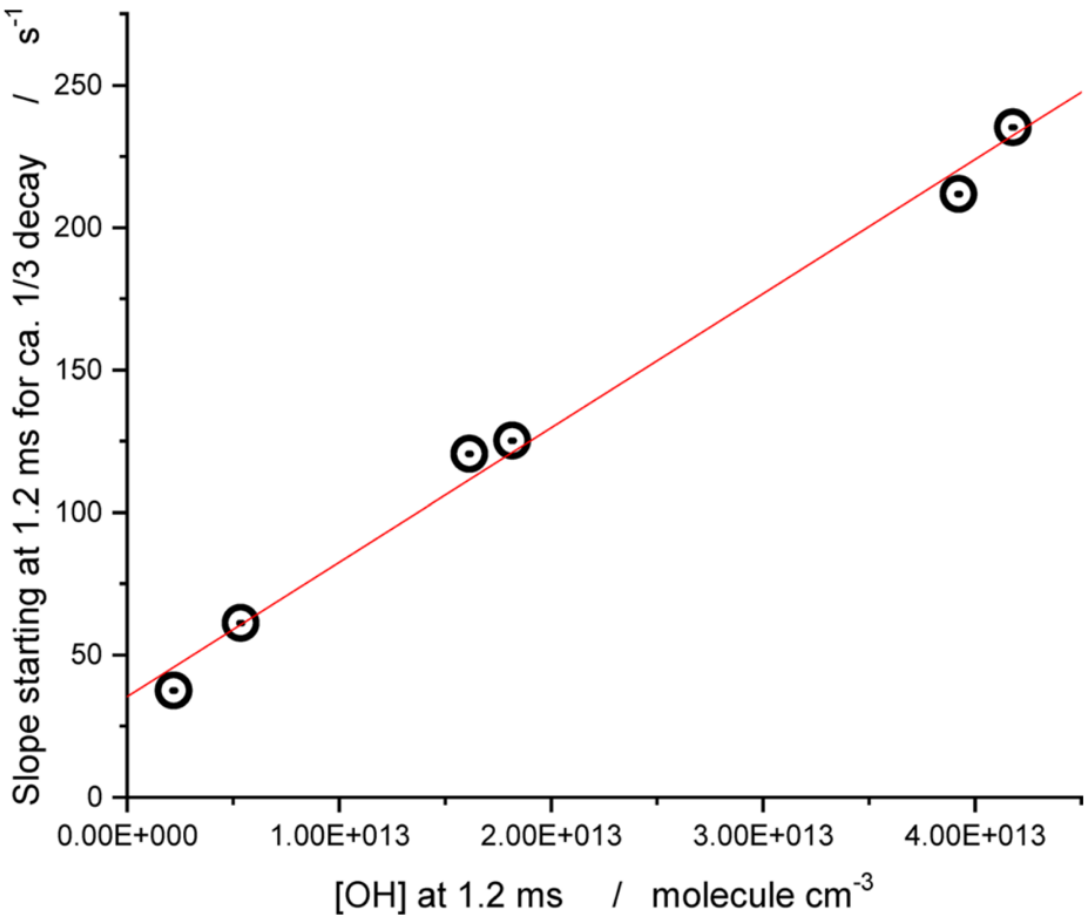

Figure 3.5 Initial slope analysis ("the first approximation") of a series of measurements at 295 K, 0.01 bar (He).

Figure 3.4 displays OH decay absorption profiles for OH radicals at different initial concentrations. Because the wall decay rate constant is initially unknown, an iterative approach was used to process the experimental data. First, the "initial slope rate constant," k', was determined by fitting an exponential curve through the initial part of the decay curve, which typically corresponds to approximately 1/3 of the amplitude decay. Next, the resulting k' was plotted against the absorption amplitude to yield a straight line with an intercept (3.5). The intercept accounts for the wash-out of the gas mixture from the reactor (a well-defined contribution) and the rate constant of the wall decay of hydroxyl radicals, $k_{w,OH}$. The intercept was then used to determine the first approximation of the hydroxyl

radical wall decay rate constant, $k_{w,OH}$ (Figure 3.6). The slope could also be used to determine the first approximation of the rate constant of channel 3.1a using the apparent stoichiometric coefficient calculated via modeling with the complete reaction mechanism.

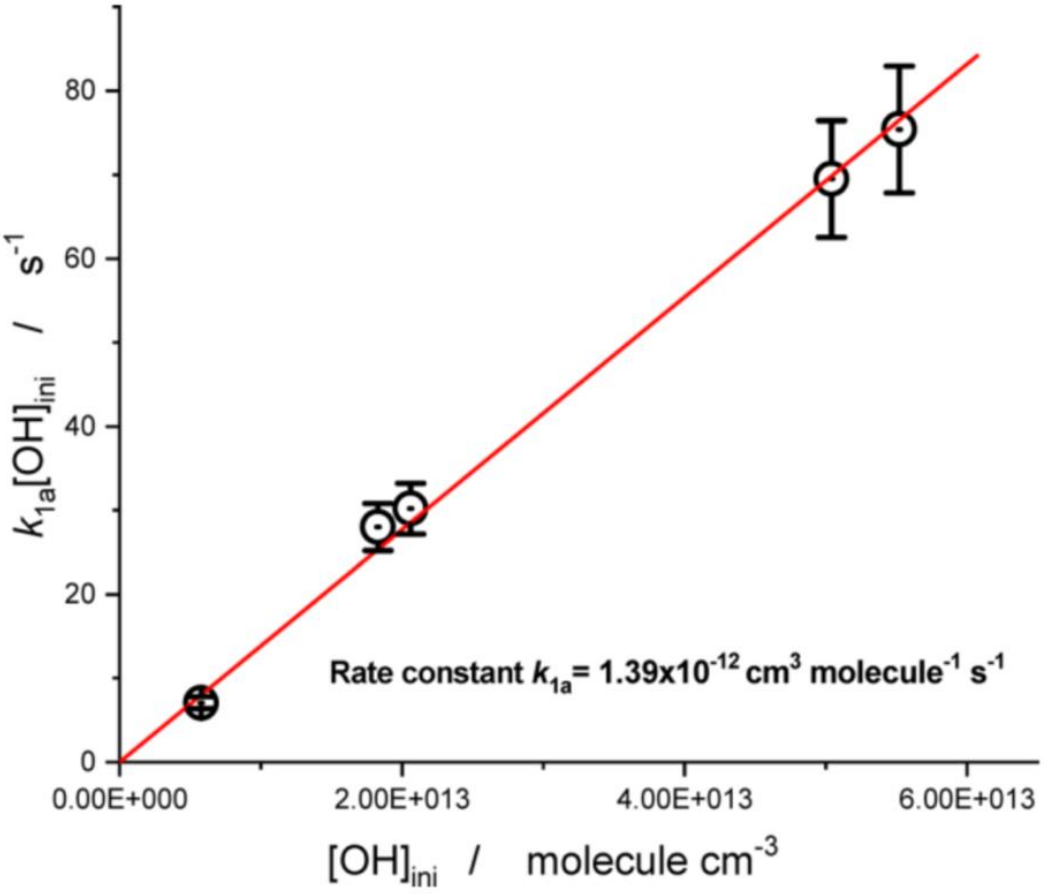

Figure 3.6 Final iteration (third) in the processing of a series of measurements.

The main concern associated with the high $[N_2O]/[H_2O]$ ratios is in the possible participation of "hot" hydroxyl radicals formed in the reaction of excited oxygen atoms with water molecules:

$$O(^1D) + H_2O \rightarrow OH^* + OH^{**} \quad (3.3)$$

Hydroxyl radicals formed in the reaction of excited oxygen atoms with water molecules can be highly vibrationally excited, with v = 1,2. Additionally, the two resulting hydroxyl radicals have very high rotational temperatures of approximately 2600 K and 6000 K, respectively.[90, 91] Due to the large rotational constant of OH radicals, it is assumed that rotational relaxation of high J levels in collisions with helium atoms is not fast. Thus, the ratio of N_2O and H_2O concentrations may be a factor to consider. When H_2O concentrations are high, relaxation of both vibrationally and rotationally excited OH radicals on water molecules would be much faster than any potential reaction with hot OH radicals with N_2O:

$$OH^* + N_2O \rightarrow N_2 + HO_2 \quad (3.4)$$

$$OH^* + N_2O \rightarrow HNO + NO \quad (3.5)$$

If reactions (3.4) and (3.5) occur, they would lead to the formation of reactive species HO_2 and HNO, which react with OH faster than the self-reaction 3.1a ($k_{3.4} = 1.1 \times 10^{-10}$, $k_{3.5} = 1.5 \times 10^{-11}$ cm^3 $molecule^{-1}$ s^{-1})[92].

To investigate this issue, measurements were performed to determine the yield of hydroxyl radicals after all fast processes had been completed, including reactions of $O(^1D)$, relaxation, and other reactions of hot species. The measurements were conducted over a wide range of $[N_2O]/[H_2O]$ ratios at three pressures of 1, 0.1, and 0.01 bar (He). The results (Figure 3.7) showed that there is no interference when the concentration of N_2O is high.

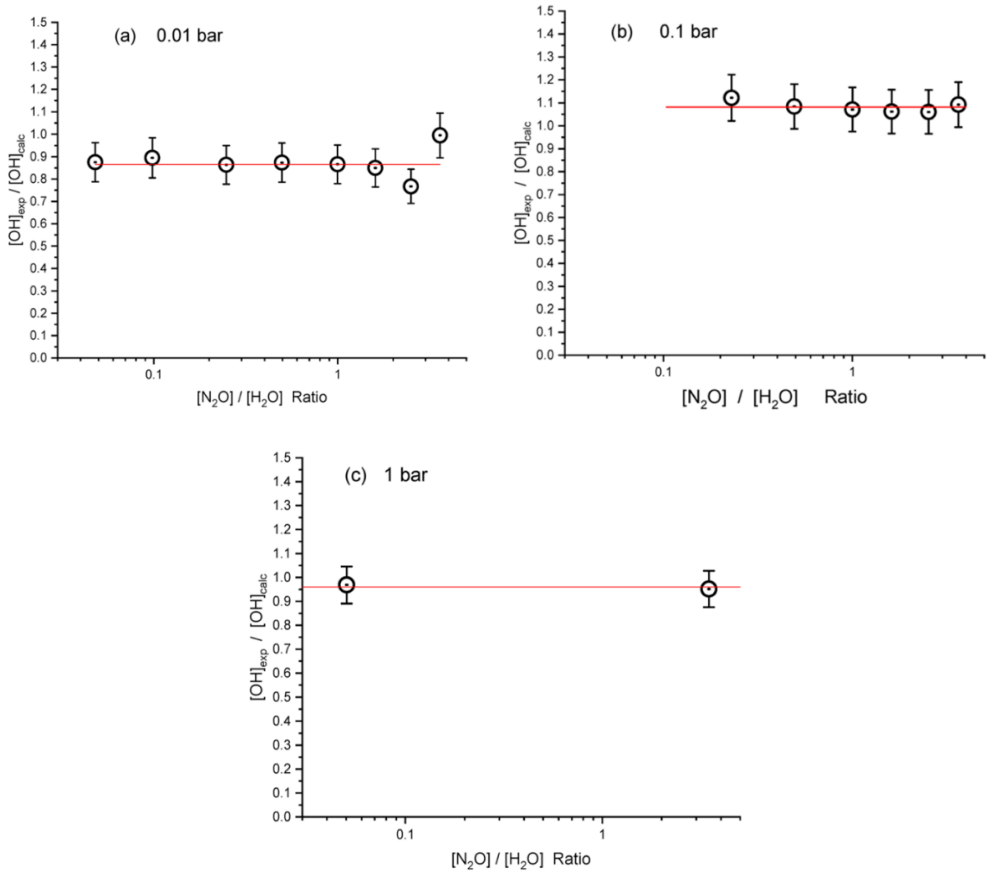

Figure 3.7 Plot of $[OH]_{exp}/[OH]_{calc}$ value vs the ratio of $[N_2O]/[H_2O]$.

3.5 Conclusion

The self-reaction of hydroxyl radicals (reaction 3.1a) was measured at ambient temperature using pulsed laser photolysis coupled to transient UV absorption, and the rate constant of the disproportionation channel was determined. The study is in excellent agreement and confirms the lower value of the rate constant of the title reaction of $k_{3.1a} = (1.4 \pm 0.2) \times 10^{-12}$ cm^3 molecule^{-1} s^{-1} (298 ± 5 K). Furthermore, the reaction was studied over a wide range of N_2O/H_2O ratios (0.05 - 3.5), confirming that no hot species are produced when the concentration of N_2O is high.

CHAPTER 4

OH+TMP

4.1 Introduction

There exist various methods for extinguishing fires, which can be classified into physical and chemical approaches. Physical techniques involve diluting the air with inert gases like nitrogen or carbon dioxide, reducing the temperature of combustible materials with liquid nitrogen or water, or obstructing the access of oxygen with solid powders, foams, or water vapor. On the other hand, chemical methods employ flame retardants that consume the active reactive species in the combustion process. Of these, the chemical approach shows greater potential since flame inhibitors can be effective even at low concentrations. In last three decades, organophosphorus compounds emerged as the leading chemically active flame retardants.[93] Trimethyl phosphate (TMP) is perhaps one of the most famous chemical compounds of this class.

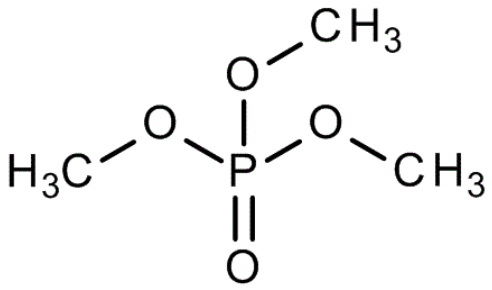

Figure 4.1 Structure of trimethyl phosphate (TMP).

Source:[94]

Trimethyl phosphate (TMP) is a phosphoric acid trimethyl ester. To evaluate the effectiveness of chemically active flame inhibitors and determine the necessary quenching concentrations, it is important to have detailed chemical combustion mechanisms that

account for the reactions between the additives and the active intermediates. The first experimental investigations into the kinetics of doped flames were conducted by Hestie[95] and Twarowski[96-98],with the proposed kinetic mechanisms serving as the foundation for subsequent research. Multiple research groups have conducted numerical and experimental studies on the combustion of TMP[99-103]. Based on these studies and others, a mechanism for the destruction of organophosphorus compounds in combustion systems was developed[104]. This mechanism includes a comprehensive range of intermediate products and incorporates quantum-chemical ab initio calculations of all essential elementary chemical reactions using the BAC-G2 method.

It is important to acknowledge that the early investigations primarily concentrated on the pathways of the transformation of phosphorus-containing compounds, mainly through participation in the catalytic recombination of free radicals, which is responsible for flame inhibition. The rate constants for the reactions of TMP with free radicals were only approximate and require precise and comprehensive experimental determinations.

It is surprising that there is a notable lack of both experimental and theoretical studies on the elementary reactions of free radicals, even for the most used organophosphorus flame retardant, TMP. Despite the significance of the reaction between the highly reactive hydroxyl radical, which is the primary chain carrier species in combustion, and TMP, only one experimental study[23] has been dedicated to determining the rate constant of OH + TMP.

$$OH + TMP \rightarrow Products. \quad (4.1)$$

Currently, no information is available on the importance of pathways involving the attachment of OH to the ‘P=O’ double bond, nor is there information on the potential

pressure dependence of the rate constant of reaction (4.1). The lack of information on the kinetics, temperature, and pressure dependencies, as well as the pathways and products of reaction (4.1), highlights the need for further extended experimental studies (preferably direct) and theoretical investigations.

In this work, a direct measurement of the reaction rate constant, OH+TMP, was carried out using laser flash photolysis combined with transient UV absorption spectroscopy over an extended temperature range, 273 - 837 K.

4.2 Experimental Approach

Figure 4.2 shows a simplified experimental set-up. There were four major parts, including the ArF excimer laser, high-pressure heatable flow reactor, hydroxyl lamp and a digital storage oscilloscope.

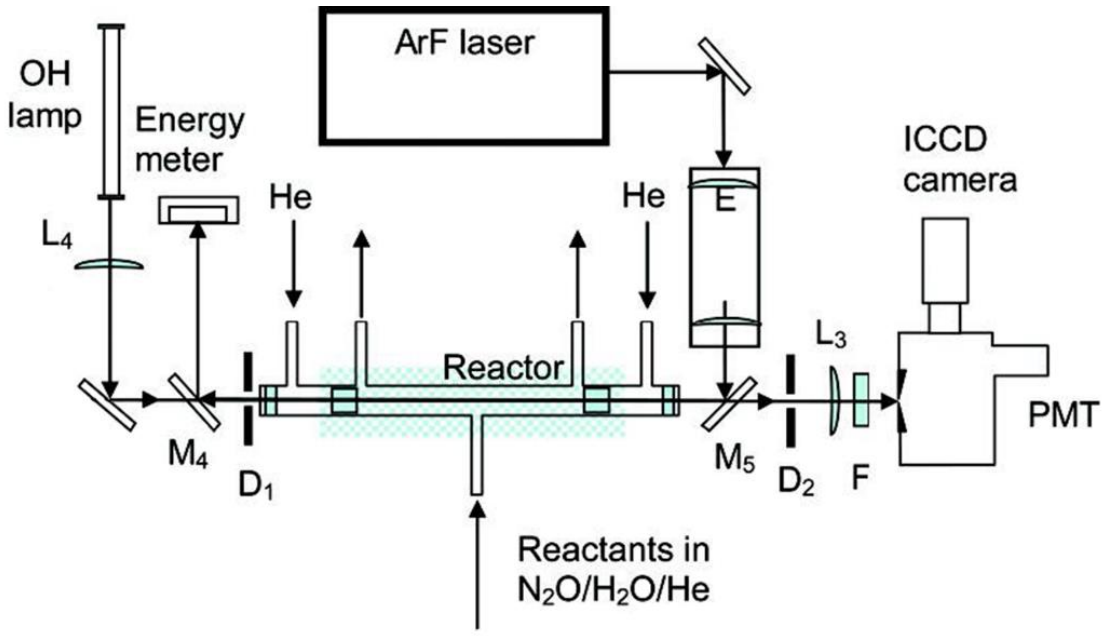

Figure 4.2 Experimental setup.

Trimethyl phosphate was introduced into the system in a form of an aqueous solution. The preparation steps of TMP in water solution are as follows: transfer 2.0 mL of trimethyl phosphate into a 50 mL volumetric flask, add around 30 mL distilled water, shake, and sonicate to dissolve. Dilute to volume with distilled water, mix well. This is the TMP/H_2O solution with a concentration of 0.343 M. This solution was degassed using freeze-thaw cycles, then withdrawn to the high-pressure precision syringe prior to use.

A high-pressure heatable flow reactor was used. The reactor was placed inside a metal block which contains two heating rods that can be heated and maintained at designed temperatures. The metal block was wrapped with insulation materials, then placed on an aluminum base. This base was cooled by flowing tap water, protecting it from melting down when the reactor is being heated.

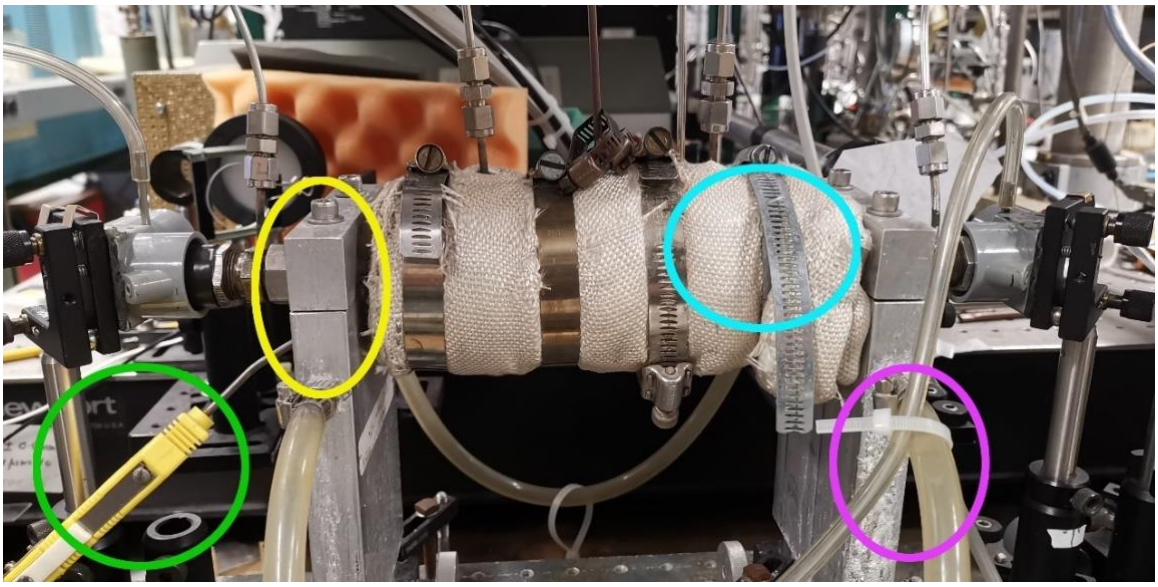

Figure 4.3 High-pressure heatable flow reactor.

Figure 4.3 shows a real picture of the reactor. From left to right, colored enclosed areas are 1) Green: Thermocouple, 2) Yellow: Supporting and positioning base, 3) Blue: insulation materials wrapped around the metal block, 4) Purple: cooling tap water tube.

There was a pre-heater enclosed around the inlet of the reactor, with a total heating length of around 12 cm. The gas mixture entered the reactor before passing a pre-heater, which was set at the same temperature as the reactor, to make sure the temperature of the gas mixture in the reactor was evenly distributed.

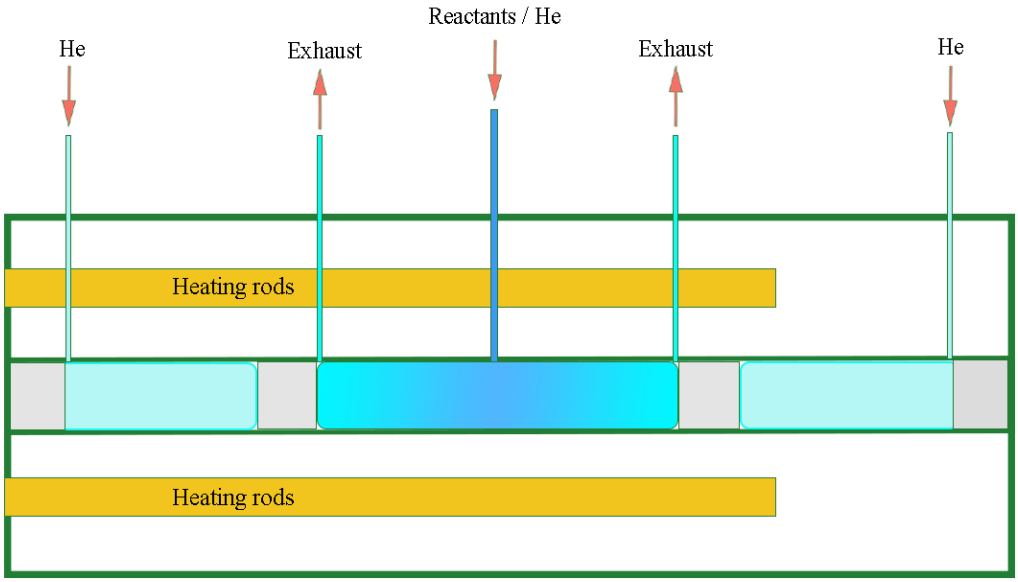

Figure 4.4 Reactor diagram.

Figure 4.4 shows the heatable high-pressure reactor diagram. The flow rates of He and N_2O were controlled by corresponding mass flow controllers (MFCs). Hydroxyl radicals were produced via photolysis of N_2O/H_2O/He at 193 nm pulsed laser (detailed mechanism see Chapter 2). To achieve uniformity across the cross section of the reactor,

the photolysis laser beam would pass through two lenses prior to entering the reactor. A spherical lens, positioned 70 cm from the reactor entrance with a focal length of 30 cm, and a spherical lens, positioned 23 cm from the reactor with a focal length of 30 cm, were used. This setup resulted in a beam uniformity of ±7.3% from the mean value, ensuring consistency throughout the reactor.

Helium was selected as a bath gas in all experiments. The measurements were conducted at varied temperature (298 - 837 K). The path length and cross section of the reaction zone was precisely defined using the four-window configuration of the reactor. Brooks mass flow controllers (model 5850) were used to control all gas flow rates. The total flow rate ranged from 10 to 65 standard cubic centimeters per second (sccs). Flush flow to the reactor windows was set as 6.5 sccs at 298 K.

Two precise syringe pumps (Harvard Apparatus, model PHD 4400) were used to inject liquid water and TMP/H_2O solution through their corresponding capillary tube into an evaporator (kept at 90 ℃) and, subsequently, to the reactor. In this way, steady flows of H_2O and TMP vapor were achieved. The total flow rate of the liquid was kept constant at each given temperature, ranging from 6 to 15 μL/min, providing approximately the same concentration of H_2O throughout the whole measurement.

The concentrations of the precursors used at 1 bar were (2.08 - 3.08) × 10^{17} (H_2O), (1.11 - 2.36) × 10^{16} (N_2O) and (0 - 10) × 10^{14} (TMP) molecules cm^{-3}. As pressure increases, the absorption cross section of OH radicals becomes smaller, the concentration of N_2O was higher to acquire better signal to noise ratio.

Reagents: In the experiments, BIP helium from Airgas with 99.9999% purity with reduced oxygen content (<10 ppb) was used. Pure nitrous oxide was obtained from Scott

Specialty Gases (purity 99.9995%). In the high-pressure experiments, certified mixture of N_2O in He (mole fraction = 0.025, accuracy = ±2%) obtained from Airgas was used. UHP argon (99.999%) was used in the H_2O/Ar discharge lamp. Distilled water was degassed using three freeze-pump-thaw cycles and used as a solvent for TMP/H_2O solutions. These solutions were supplied by two syringe pumps (Harvard Apparatus PHD 4400). TMP was purchased from Aldrich, >97%.

4.3 Data Processing

The experiment conditions were written in the lab notebook, then digitized and saved on a computer. The kinetics data, including the time-resolved absorption decay data, were saved in both the lab computer and personal storage devices. The kinetic data was fitted and processed using Origin software to get the rate constant.

Once the laser pulse passes through the reactor, OH radicals were generated within a few μs, the decay curve was monitored and recorded by an oscilloscope. Decay of the OH concentration was due to the reactions of OH radical with OH (self-reaction)[15], the reactor wall, as well as the target molecule TMP.

Once the hydroxyl radicals were generated, they were consumed in the target reaction (4.1), along with the side reactions mentioned earlier. As a result, the consumption rate constant could be expressed as follows at short times:

$$k' = -\frac{1}{[OH]0}\frac{d[OH]}{dt} = k1' + k0 \; at \; t = 0 \qquad \text{(E4.1)}$$

Where k' is the "initial slope" rate constant, $k_1' = k_1[TMP]$ is the pseudo-first order rate constant of the target reaction, k_0 accounts for all other reactions. To obtain the initial

slopes of the decay curves, the initial portion of the data needed to be accurately fitted. For decay processes that follow pseudo-first order kinetics, an exponential decay function was selected to determine the decay rates as it can provide a reliable estimate of the "initial slopes".

An iterative approach was employed to analyze the experimental data. Initially, an exponential decay function was used to fit the initial portion of the decay curve and obtain the "initial slope rate constant," k'. Typically, this involved using the decay curve's initial part that corresponds to approximately one-third of the amplitude drop. Subsequently, k' was plotted against the TMP molecule concentration, producing a linear line. The slope of this linear line provided the rate constant for the OH+TMP reaction under the experimental conditions.

Sample OH decay absorption profiles with different concentrations of TMP are shown in Figure 4.5.

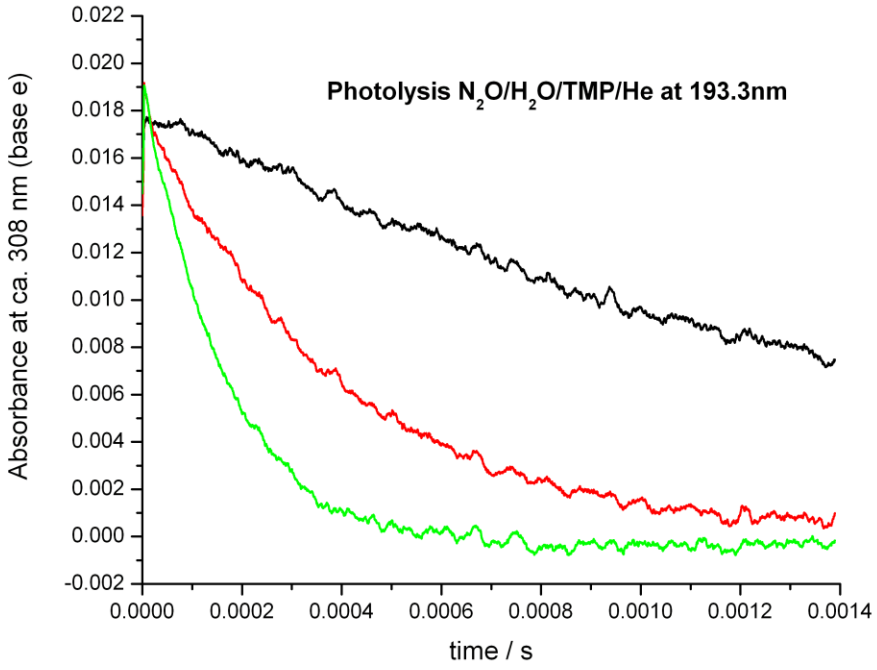

Figure 4.5 Sample UV absorption profiles of OH radical (multiline at ca. 308 nm). Photolysis of $N_2O/H_2O/TMP/He$ mixture at 193.3 nm. T=673 K, p=1 bar.

The reactants' concentrations in 4.5 are: $[N_2O] = 1.66 \times 10^{16}$ molecules cm^{-3}, $[H_2O] = 3.66 \times 10^{17}$ molecules cm^{-3}, $[N_2O]/[H_2O] = 0.054$, $[TMP] = 0 - 10 \times 10^{14}$ molecules cm^{-3}. The initial concentration of OH is approximately the same. Black-[TMP] = 0, red- $[TMP] = 4 \times 10^{14}$ molecules cm^{-3}, green- $[TMP] = 10 \times 10^{14}$ molecules cm^{-3}.

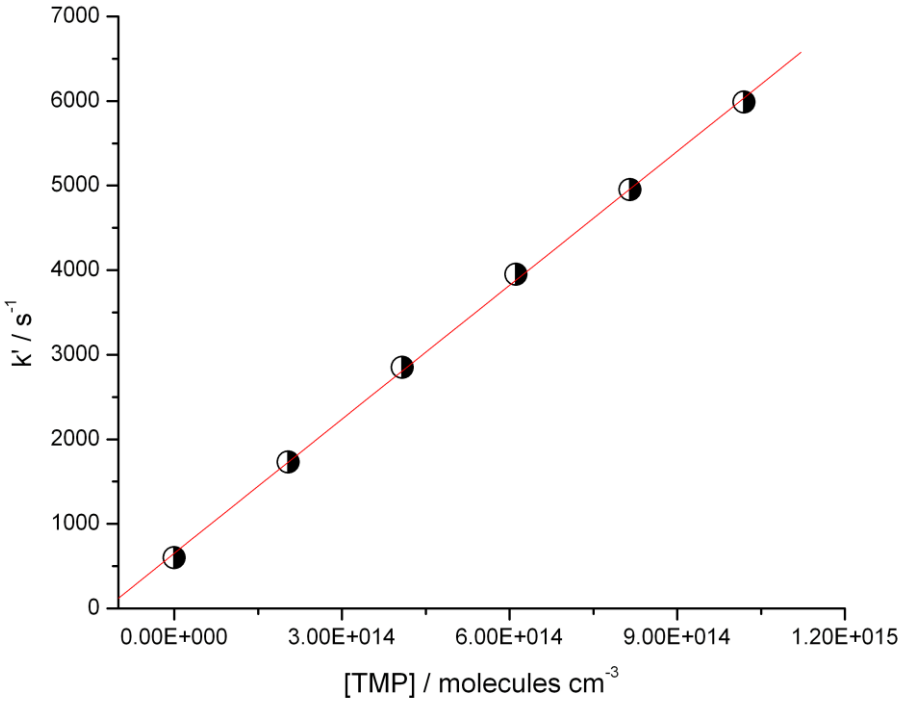

Figure 4.6 Sample initial slope k' of a series of measurements (at 673 K, 1 bar), versus [TMP].

The reactants' concentrations were kept constant, except [TMP] ranges from 0 to 10×10^{14} molecules cm^{-3}, with 5 intervals controlled by the flow rate of TMP in H_2O solution.

4.4 Results and Discussion

The experimental conditions, including reactants' concentrations, temperatures and pressures, and the resulting rate constant, are listed in Table 4.1.

Table 4.1 Experimental Conditions and Rate Constant of Reaction TMP + OH at 1 bar, Varied Temperatures

T / K	P / bar	$[H_2O]/10^{17}$ molecule/cm^3	$[N_2O]/10^{16}$ molecule/cm^3	$[TMP]/10^{14}$ molecule/cm^3	$k'/10^3$ s^{-1}	$k/10^{-12}$ molecule/cm^3/s
298	1.015	3.08	2.27	0	0.568	7.96
298	1.015	3.08	2.27	10.14	11.39	
298	1.015	3.08	2.27	8.11	10	
298	1.015	3.08	2.27	6.08	7.246	
298	1.015	3.08	2.27	4.06	5.181	
298	1.015	3.08	2.27	2.03	3.164	
365	1.013	2.91	2.36	0	0.286	3.87
365	1.013	2.91	2.36	10.18	4.695	
365	1.013	2.91	2.36	8.14	3.788	
365	1.013	2.91	2.36	6.11	3.003	
365	1.013	2.91	2.36	4.07	2.183	
365	1.013	2.91	2.36	2.04	1.266	
411	1.013	2.84	2.09	0	0.213	3.17
411	1.013	2.84	2.09	10.32	3.745	
411	1.013	2.84	2.09	8.26	2.985	
411	1.013	2.84	2.09	6.19	2.37	
411	1.013	2.84	2.09	4.13	1.623	
411	1.013	2.84	2.09	2.06	1.087	
500	1.015	2.96	1.85	0	1.127	3.09
500	1.015	2.96	1.85	10.23	4.739	
500	1.015	2.96	1.85	8.19	3.952	
500	1.015	2.96	1.85	6.14	3.279	
500	1.015	2.96	1.85	4.09	2.512	
500	1.015	2.96	1.85	2.05	1.672	
629	1.019	2.63	1.98	0	0.505	4.47
629	1.019	2.63	1.98	2.01	1.825	
629	1.019	2.62	1.98	4.01	2.577	
629	1.019	2.62	1.98	6.02	2.237	

Table 4.1 Experimental Conditions and Rate Constant of Reaction TMP + OH at 1 bar, Varied Temperatures (Continued)

T / K	P / bar	$[H_2O]/10^{17}$ molecule/cm^3	$[N_2O]/10^{16}$ molecule/cm^3	$[TMP]/10^{14}$ molecule/cm^3	$k'/10^3$ s^{-1}	$k/10^{-12}$ molecule/cm^3/s
629	1.019	2.62	1.98	8.03	4.167	4.47
629	1.019	2.64	1.98	10.03	4.878	
673	1.01	3.06	1.66	0	0.598	5.35
673	1.01	3.06	1.66	10.2	5.988	
673	1.01	3.06	1.66	8.16	4.95	
673	1.01	3.06	1.66	6.12	3.952	
673	1.01	3.06	1.66	4.09	2.849	
673	1.01	3.06	1.66	2.05	1.73	
773	1.015	2.83	1.53	0	0.917	8.41
773	1.015	2.83	1.53	9.43	7.634	
773	1.015	2.83	1.53	7.54	6.024	
773	1.015	2.83	1.53	5.66	4.854	
773	1.015	2.83	1.53	3.77	3.3	
773	1.015	2.83	1.53	1.88	2.037	
837	1.013	2.08	1.11	0	0.61	11.43
837	1.013	1.05	1.12	10.54	13.85	
837	1.013	2.08	1.11	8.33	10.74	
837	1.013	2.08	1.11	6.25	7.463	
837	1.013	2.08	1.11	4.16	5.236	
837	1.013	2.08	1.11	2.08	2.809	

Figure 4.7 shows the resulted k' value vs [TMP], at various temperatures. The temperature ranged from room temperature to the upper limit, 837 K. Each linear fit gave a rate constant at corresponding reaction conditions.

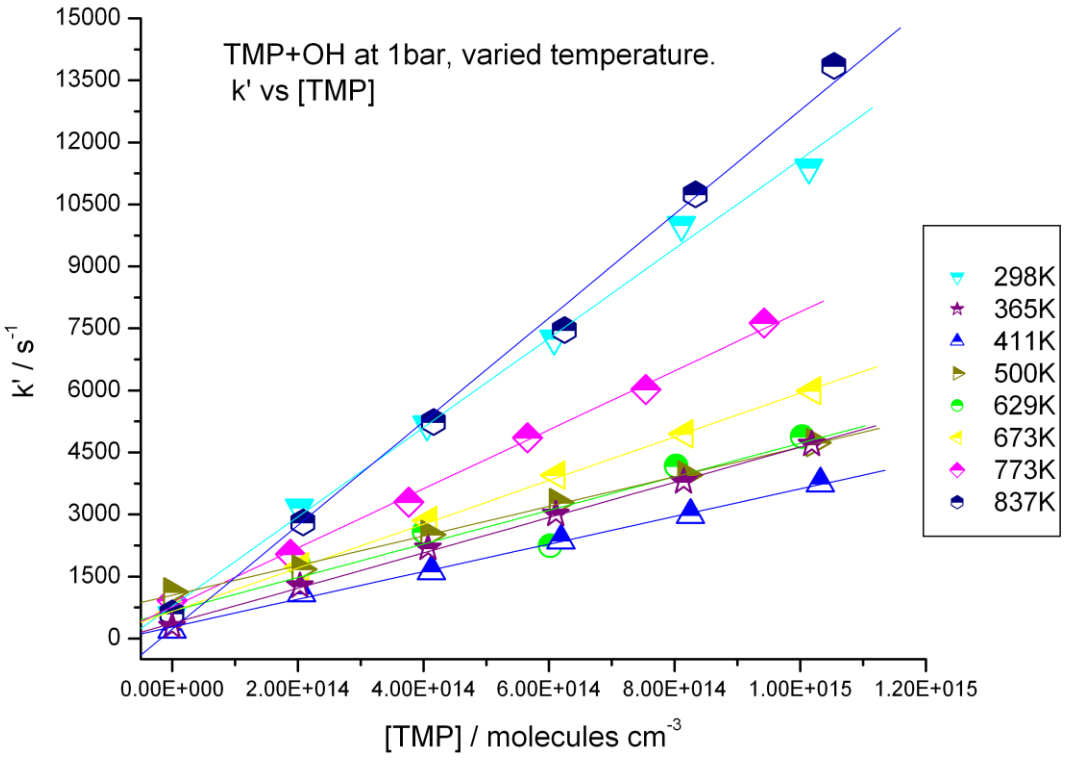

Figure 4.7 Summary of k' vs [TMP] at different temperature. Each linear fitting gives a k(TMP+OH) at that temperature.

Different rate constants were plotted vs 1000 K/T, where T is the corresponding temperatures in K. The result is shown in Figure 4.8, a V-shaped temperature dependent rate constant was observed.

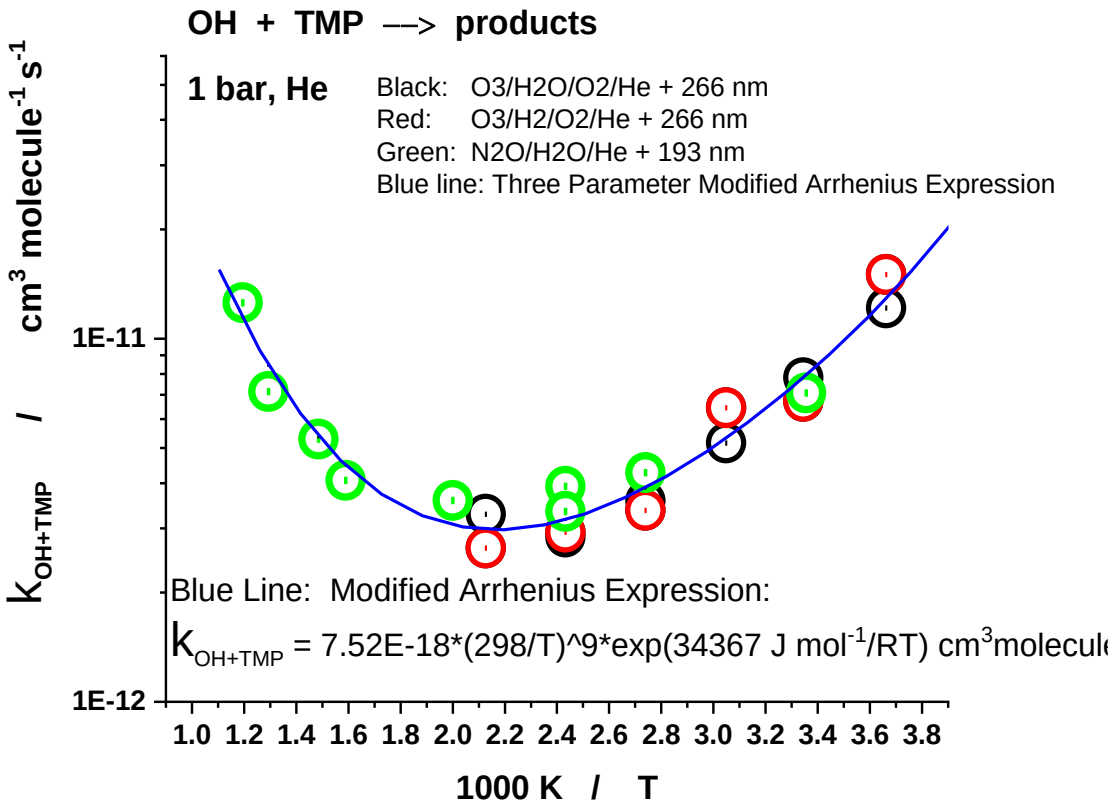

Figure 4.8 Rate constant of reaction 4.1 at 1 bar, over the temperature range 298 - 837 K.

In Figure 4.8, green points: N_2O/H_2O/He +193 nm, black points: O_3, H_2O, + 266 nm, red points: O_3/H_2/He +266 nm. Blue line – fit by the Modified 3-parameter Arrhenius Expression.

Besides the measurements described above, several high-pressure measurements at room temperature were conducted, too. These experimental conditions, including reactants' concentrations, temperatures and pressures, and the resulting rate constant, are listed in Table 4.2.

Table 4.2 Experimental Conditions and Rate Constant of Reaction TMP + OH at RT, Varied Pressures

T / K	P / bar	$[H_2O]/10^{17}$ molecule/cm^3	$[N_2O]/10^{16}$ molecule/cm^3	$[TMP]/10^{14}$ molecule/cm^3	$k'/10^3$ s^{-1}	$k/10^{-12}$ molecule/cm^3/s
295	3	3.98	9.59	0	0.926	9.44
295	3	3.98	9.59	9.96	10.57	
295	3	3.98	9.59	7.97	8.62	
295	3	3.98	9.59	5.98	6.757	
295	3	3.98	9.59	3.98	4.808	
295	3	3.98	9.59	1.99	3.289	
295	3	3.98	9.59	0	1.205	
297	10	3.54	12.9	0	1.149	10.24
294	10	3.58	13	8.94	10.34	
293	10	3.59	13.1	7.18	8.333	
293	10	3.59	13.1	5.38	6.211	
293	10	3.59	13.1	3.59	4.237	
292	10	3.6	13.1	1.8	2.941	

Table 4.3 shows the reaction conditions carried at 773 K and several pressures.

Table 4.3 Experimental Conditions and Rate Constant of Reaction TMP + OH at 773 K, Varied Pressures

T / K	P / bar	$[H_2O]/10^{17}$ molecule/cm^3	$[N_2O]/10^{16}$ molecule/cm^3	$[TMP]/10^{14}$ molecule/cm^3	$k'/10^3$ s^{-1}	$k/10^{-12}$ molecule/cm^3/s
773	3	1.58	1.04	0	0.182	
773	3	1.58	1.04	3.95	4.132	
773	3	1.58	1.04	3.16	3.584	
773	3	1.58	1.04	2.37	2.71	10.17
773	3	1.58	1.04	1.58	2.008	
773	3	1.58	1.04	0.79	1.112	
773	3	1.58	1.04	0	0.208	
773	10	1.38	1.81	0	0.392	
773	10	1.38	1.81	3.46	5.348	
773	10	1.38	1.81	2.76	4.464	
773	10	1.38	1.81	2.07	3.521	14.75
773	10	1.38	1.81	1.38	2.433	
773	10	1.38	1.81	0.69	1.357	
773	10	1.38	1.81	0	0.256	
773	30	1.84	5.03	0	0.847	
773	30	1.84	5.03	4.6	9.524	
773	30	1.84	5.03	3.68	7.194	
773	30	1.84	5.03	2.76	5.814	18.39
773	30	1.84	5.03	1.84	4.098	
773	30	1.84	5.03	0.92	2.252	
773	30	1.84	5.03	0	0.885	

The resulted rate constants were plotted vs the pressure (log scale), as shown in Figure 4.9. A positive pressure dependent rate constant was observed at both room temperature and elevated temperature.

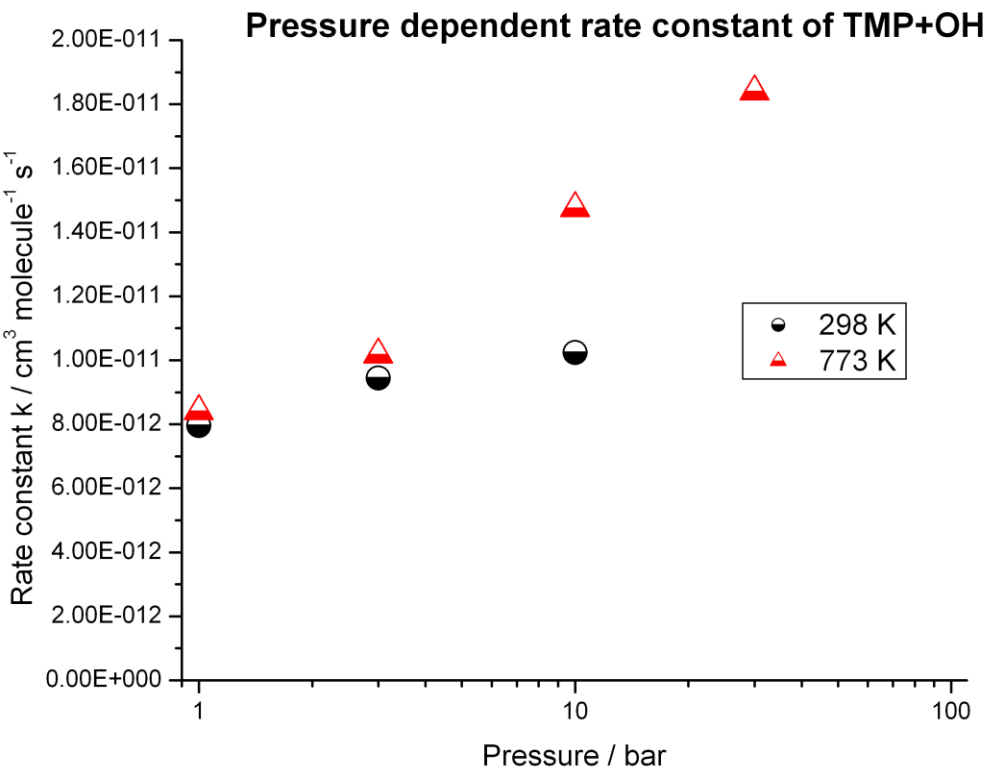

Figure 4.9 Summary of pressure-dependent measurements of k(TMP+OH) at two temperatures.

4.5 Conclusion

Two research groups investigated the reaction between hydroxyl radicals and trimethyl phosphate (reaction (4.1)) using three distinct hydroxyl radical generation methods at temperatures ranging from 273 to 837 K. The rate constant at room temperature was in excellent agreement with the only previous determination.

A V-shaped temperature dependence with a turning point at 471 K was unambiguously established, with a negative slope at low temperatures and a positive slope at higher temperatures. Extended experimental investigations, including bath gas pressure

dependence, as well as theoretical studies of this reaction and other phosphorus-centered compounds, are necessary for understanding the reaction mechanism.

CHAPTER 5

OH+DMMP

5.1 Introduction

Over the past few decades, it has been widely acknowledged that organophosphorus compounds are effective flame retardants, even at low concentrations[105] However, these compounds are also present in the environment as pesticides, insecticides, and so on [106]. To gain a better understanding of the mechanisms behind flame retardancy and the breakdown of these compounds in the environment, it is essential to have detailed knowledge of the kinetics of the elementary reactions in their reaction mechanisms. Unfortunately, such data are currently very limited, even for reactions with major oxidation species such as the hydroxyl radical (OH). Specifically, for the target reaction of this study, reaction of hydroxyl radical with dimethyl methylphosphonate, DMMP, $(CH_3O)_2CH_3PO$, only a single indirect kinetic study exists[107].

$$OH + DMMP \rightarrow Products. \quad (5.1)$$

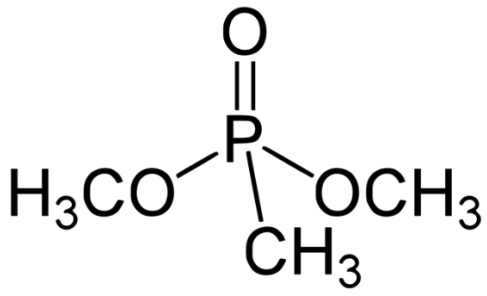

Figure 5.1 Structure of dimethyl methylphosphonate (DMMP).
Source:[94]

In the only existing gas-phase indirect kinetic study for the reaction of hydroxyl radical with dimethyl methylphosphonate (DMMP), the rate of reaction (5.1) was measured relative to the rate of reaction of hydroxyl radicals with n-butyl ether $(n\text{-}C_4H_9)_2O$ across a temperature range of 283 - 348 K. Within this range, a negative temperature dependence was observed, indicating that the reaction rate decreased with increasing temperature. A similar trend was previously observed for the reaction of hydroxyl radical with trimethyl phosphate (TMP, $(CH_3O)_3PO$)[14], wherein the negative temperature dependence at lower temperatures shifted to a positive temperature dependence at higher temperatures, resulting in a V-shaped temperature dependence.

This study utilized pulsed laser photolysis and transient UV absorption to investigate the kinetics of reaction (5.1) over a wide temperature range of 295 - 837 K. A unique V-shaped temperature dependence was observed, which is like what was previously reported for the reaction of OH with TMP. Additionally, a pressure dependence was observed within the pressure range of 0 - 30 bar, consistent with predictions from theoretical studies.

5.2 Experimental Approach

The experimental set-up was the same as described in Chapter 4. Hydroxyl radicals were generated in pulsed photolysis of N_2O in the presence of water vapor at 193.3 nm (ArF excimer laser).

$$N_2O + h\nu\ (193\ nm) \rightarrow O(^1D) + N_2 \qquad (5.2)$$

$$O(^1D) + H_2O \rightarrow 2\ OH \qquad (5.3)$$

The importance of different channels of the photodissociation process as well as of the subsequent reaction of $O(^1D)$ with H_2O were also discussed in detail in previous publications.

Like the TMP (see Chapter 4), the DMMP was introduced into the system in the form of an aqueous solution. The difference is that a lower concentration of DMMP was used, to increase the infuse rate interval of DMMP/H_2O solution. This preparation fastened the equilibrium of the evaporation process when the infuse rate was changed. The preparation steps of DMMP in water solution are as follows: transfer 2.0 mL of DMMP into a 100 mL volumetric flask, add ca. 70 mL of distilled water, shake, and sonicate to dissolve. Dilute to volume with distilled water, mix well. This is the DMMP/H_2O solution with a concentration of 0.181 M. This solution was degassed using freeze-thaw cycles at least three times, then withdrawn to the high-pressure precision syringe prior to use.

The kinetics of hydroxyl radical decay was monitored by absorption in the UV (multi-line at ca. 308 nm using low pressure H_2O/Ar DC discharge lamp). The gas flow rates were controlled by mass flow controllers (Brooks, model 5850). The total flow rates of the reactant mixtures with He were in the range 11 – 12 sccs. Additional He flush flows to the reactor windows were 2 sccs. The liquid injection performed via corresponding capillary tubes through an evaporator (kept at 90 ℃) and, subsequently, to the reactor. In this way, steady flows of H_2O and DMMP vapor were achieved. The total flow rate of these two liquids were kept constant at each given temperature, ranged from 6 to 11 μL/min, provided approximately the same concentration of H_2O. The equivalent gas flow rate of DMMP in standard cubic centimeters per minute (sccm) was calculated based on the volumetric flowrate of the solution, based on the ideal gas law.

The concentrations of the precursors used were $(1.94 – 3.24) \times 10^{17}$ (H_2O), $(3.23 – 7.70) \times 10^{16}$ (N_2O) and $(0 – 10) \times 10^{14}$ (DMMP) molecule cm^{-3}.

The absolute concentrations of OH radicals were calculated based on the photon flux inside the reactor, the absorption cross-section of N_2O at 193.3 nm, and the efficiency of conversion of $O(^1D)$ atoms produced in the photolysis of N_2O to OH radicals. The absorption cross-section of N_2O at 298 and 1 bar is accurately known, at other conditions, the cross-sections of N_2O were measured in previous works[29, 108-110]. The model used for the calculations of the efficiency of conversion of excited $O(^1D)$ atom to OH radicals and in-situ laser light actinometry were explained in detail in Chapter 2. The approach was based on the monitoring of ozone formation at 253.6 nm in the photolysis of $N_2O/O_2/N_2$ mixtures at 1 bar and 298 K. The photolysis laser photon fluence inside the reactor was varied in the range of $(4 – 9) \times 10^{15}$ photon cm^{-2} $pulse^{-1}$. The initial concentrations of hydroxyl radicals were in the range $(1.4 – 2.7) \times 10^{13}$ molecule cm^{-3}.

5.3 Data Processing

The decrease in OH concentration is caused by various reactions involving OH, such as OH radical self-reaction, decay on the walls, and the target reaction with DMMP. Additionally, the decay rates may also be influenced by secondary reactions involving the products of reaction (5.1). In contrast to our previous investigations of elementary reactions of hydroxyl radical and other radical species, where the corresponding reaction mechanism's system of differential equations was numerically solved and the resulting profiles were fitted to the experimental data, we adopted a simplified analysis in this study. As of now, there is no available information regarding the products, branching ratios, and

rate constants of subsequent reactions for reaction (5.1). Due to the lack of a detailed reaction mechanism, the previously used rigorous approach was not feasible, and no integrated kinetic decay curves could be obtained. Hence, the method of initial rates, which is widely used in chemical kinetics, was applied instead.

After the formation of OH radicals, they were consumed by the target reaction (5.1), as well as other side reactions. At short times the consumption rate of OH radicals, k', can be written as:

$$k' = \left(\frac{1}{[OH]0} * \frac{d[OH]}{dt}\right) at\ t = 0 \quad \text{(E5.1)}$$

$$k' = k1' + k0 \quad \text{(E5.2)}$$

$$k1' = k1 * [DMMP] \quad \text{(E5.3)}$$

where k' is the "initial slope rate constant" defined by Equation (E5.1), k_1' is the pseudo-first order rate constant of the target reaction, and k_0 accounts for all other processes. To properly evaluate the initial slopes of the decay curves, it is necessary to fit the initial fractions of the curves with an appropriate function. There are various functions available, including linear ones, that can be used for this purpose. In the case of pseudo-first order decays, the decay profiles follow an exponential function. Hence, we chose the exponential decay function to estimate the initial decay rates, as it provides an unbiased estimation of the "initial slopes" for such processes.

Several OH radical sample UV absorption profiles are shown in Figure 5.2. To evaluate the "initial slope" rate constant, the initial portion of the decay profiles (About one-third of the amplitude) was fitted with exponential function:

$$[OH] = [OH]0 * \exp(-k't) \quad \text{(E5.4)}$$

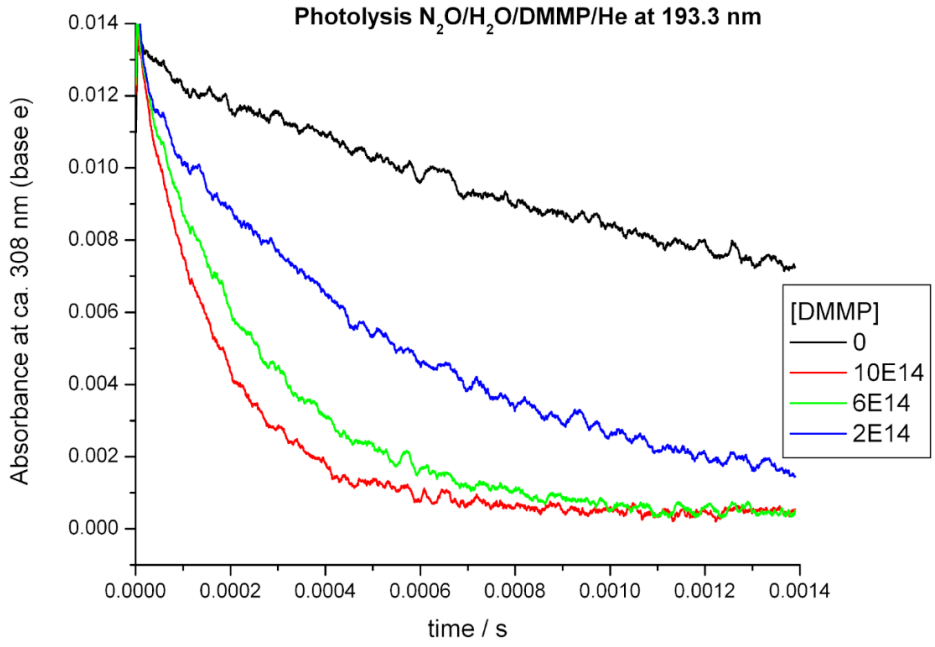

Figure 5.2 Sample UV absorption profiles of OH radical (multiline at ca. 308 nm). Photolysis of N_2O/H_2O/DMMP/He mixture at 193.3 nm. T = 365 K, p = 1 bar.

The reactants' concentration in Figure 5.2 are: $[N_2O] = 4.49 \times 10^{16}$ molecules cm^{-3} , $[H_2O] = 2.91 \times 10^{17}$ molecules cm^{-3} , $[N_2O]/[H_2O] = 0.154$, [TMP] = 0 - 10×10^{14} molecules cm^{-3}. The initial concentration of OH is approximately the same. Black- [DMMP] = 0, red- [DMMP] = 10×10^{14} molecules cm^{-3}, green- [DMMP] = 6×10^{14} molecules cm^{-3}, blue- [DMMP] = 2×10^{14} molecules cm^{-3}.

By plotting the rate of initial slope k' as a function of the concentration of the reactant [DMMP], a straight line was obtained, as shown in Figure 5.3. The slope of this line represents the rate constant for the target reaction (5.1), while the intercept provides information about the contribution of other processes (such as self-reaction) during the initial stage of the reaction.

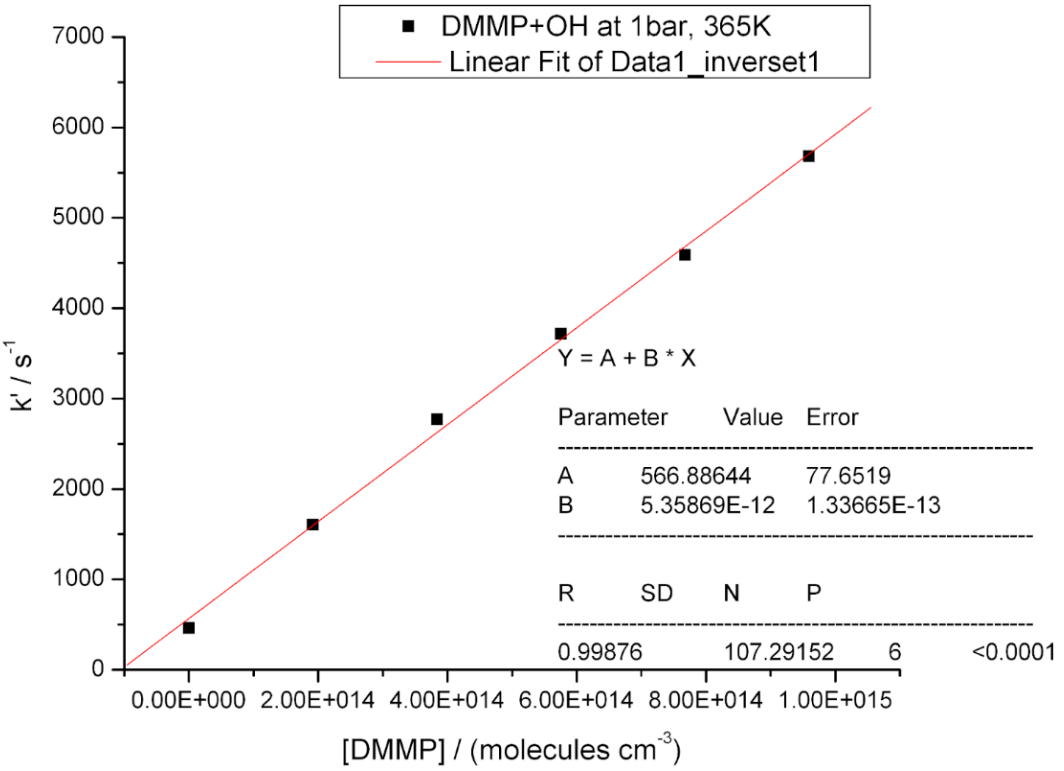

Figure 5.3 Sample initial slope k' of a series of measurements (at 365 K, 1 bar), versus [DMMP].

The reactants' concentrations were kept constant, except [DMMP] ranged from 0 to 10×10^{14} molecules cm^{-3}, with 5 intervals controlled by the flow rate of DMMP in H_2O solution.

5.4 Results and Discussion

The reaction conditions carried at 1 bar pressure as well as the resulted rate constants are shown in Table 5.1.

Table 5.1 Experimental Conditions and Rate Constant of Reaction OH + DMMP at 1 bar, Varied Temperatures

T / K	P / bar	$[H_2O]/10^{17}$ molecule/cm^3	$[N_2O]/10^{16}$ molecule/cm^3	$[DMMP]/10^{14}$ molecule/cm^3	$k'/10^3$ s^{-1}	$k/10^{-12}$ molecule/cm^3/s
295	1.02	3.03	3.23	0	0.847	
295	1.02	3.03	3.23	10	9.259	
295	1.02	3.03	3.23	8	7.576	
295	1.02	3.03	3.23	6	5.952	8.51
295	1.02	3.03	3.23	4	4.219	
295	1.02	3.03	3.23	2	2.247	
295	1.02	3.03	3.23	0	0.794	
323	1.015	2.98	7.7	0	0.448	
323	1.015	2.98	7.7	7.56	5.618	
323	1.015	2.98	7.7	6.05	4.608	
323	1.015	2.98	7.7	4.54	3.436	6.82
323	1.015	2.98	7.7	3.02	2.347	
323	1.015	2.98	7.7	1.51	1.513	
323	1.015	2.98	7.7	0	0.442	
365	1.016	2.91	4.49	0	0.463	
365	1.016	2.91	4.49	9.59	5.682	
365	1.016	2.91	4.49	7.68	4.587	
365	1.016	2.91	4.49	5.76	3.717	5.36
365	1.016	2.91	4.49	3.84	2.77	
365	1.016	2.91	4.49	1.92	1.605	
411	1.009	3.03	5.99	0	0.36	
411	1.009	3.03	5.99	10	4.566	
411	1.009	3.03	5.99	8	3.774	
411	1.009	3.03	5.99	6	3.04	4.17
411	1.009	3.03	5.99	4	2.242	
411	1.009	3.03	5.99	2	1.324	
411	1.009	3.03	5.99	0	0.465	

Table 5.1 Experimental Conditions and Rate Constant of Reaction OH + DMMP at 1 bar, Varied Temperatures (Continued)

T / K	P / bar	$[H_2O]/10^{17}$ molecule/cm^3	$[N_2O]/10^{16}$ molecule/cm^3	$[DMMP]/10^{14}$ molecule/cm^3	$k'/10^3$ s^{-1}	$k/10^{-12}$ molecule/cm^3/s
455	1.018	3.24	5.44	0	0.341	
455	1.018	3.24	5.44	9.62	3.831	
455	1.018	3.24	5.44	7.7	3.096	
455	1.018	3.24	5.44	5.77	2.525	3.59
455	1.018	3.24	5.44	3.85	1.89	
455	1.018	3.24	5.44	1.92	1.058	
455	1.018	3.24	5.44	0	0.394	
500	1.014	2.81	4.23	0	0.371	
500	1.014	2.81	4.23	9.27	3.268	
500	1.014	2.81	4.23	7.42	2.747	
500	1.014	2.81	4.23	5.56	2.164	3.16
500	1.014	2.81	4.23	3.71	1.481	
500	1.014	2.81	4.23	1.85	1	
500	1.014	2.81	4.23	0	0.35	
540	1.017	2.46	3.64	0	0.34	
540	1.017	2.46	3.64	9.02	3.086	
540	1.017	2.46	3.64	7.22	2.512	
540	1.017	2.46	3.64	5.41	1.984	2.98
540	1.017	2.46	3.64	3.61	1.51	
540	1.017	2.46	3.64	1.8	1.038	
540	1.017	2.46	3.64	0	0.353	
591	1.015	2.73	4.17	0	0.388	
591	1.015	2.73	4.17	9.82	3.509	
591	1.015	2.73	4.17	7.86	2.915	
591	1.015	2.73	4.17	5.9	2.278	3.17
591	1.015	2.73	4.17	3.93	1.7	
591	1.015	2.73	4.17	1.96	1.03	
591	1.015	2.73	4.17	0	0.427	

Table 5.1 Experimental Conditions and Rate Constant of Reaction OH + DMMP at 1 bar, Varied Temperatures (Continued)

T / K	P / bar	$[H_2O]/10^{17}$ molecule/cm^3	$[N_2O]/10^{16}$ molecule/cm^3	$[DMMP]/10^{14}$ molecule/cm^3	$k'/10^3$ s^{-1}	$k/10^{-12}$ molecule/cm^3/s
673	1.024	2.42	4.85	0	0.355	
673	1.024	2.42	4.85	8.7	3.65	
673	1.024	2.42	4.85	6.96	3.058	
673	1.024	2.42	4.85	5.22	2.512	3.85
673	1.024	2.42	4.85	3.48	1.742	
673	1.024	2.42	4.85	1.74	1.066	
673	1.024	2.42	4.85	0	0.346	
773	1.023	2.1	3.55	0	0.424	
773	1.023	2.1	3.55	7.6	4.348	
773	1.023	2.1	3.55	6.06	3.571	
773	1.023	2.1	3.55	4.54	2.841	5.16
773	1.023	2.1	3.55	3.03	2.146	
773	1.023	2.1	3.55	1.51	1.33	
773	1.023	2.1	3.55	0	0.412	
837	1.022	1.94	3.27	0	0.465	
837	1.022	1.94	3.27	9.89	6.452	
837	1.022	1.94	3.27	7.91	5.319	
837	1.022	1.94	3.27	5.94	4.184	6.07
837	1.022	1.94	3.27	3.96	3.012	
837	1.022	1.94	3.27	1.98	1.905	
837	1.022	1.94	3.27	0	0.385	

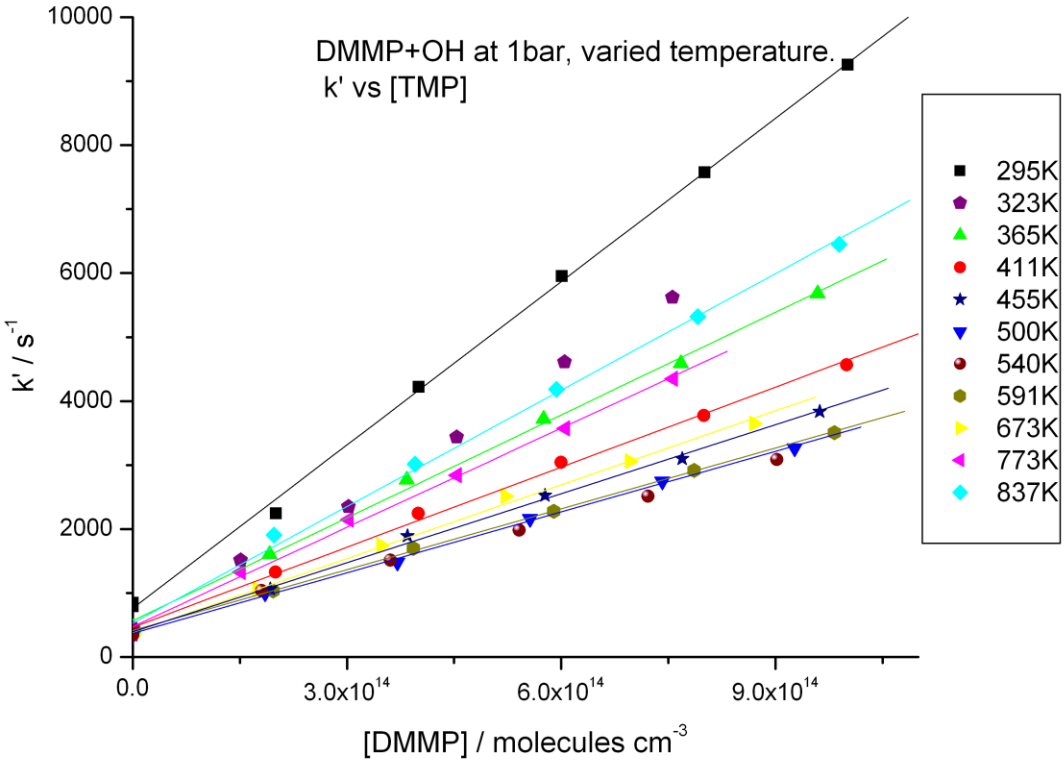

Figure 5.4 Summary of k' vs [DMMP] at different temperatures.

Each linear fit gives a k(DMMP+OH) at that temperature. Plot the rate constant vs 1000 K/T, where T is the reaction temperature in K, the result is shown in Figure 5.6. A V-shaped temperature dependent rate constant was observed.

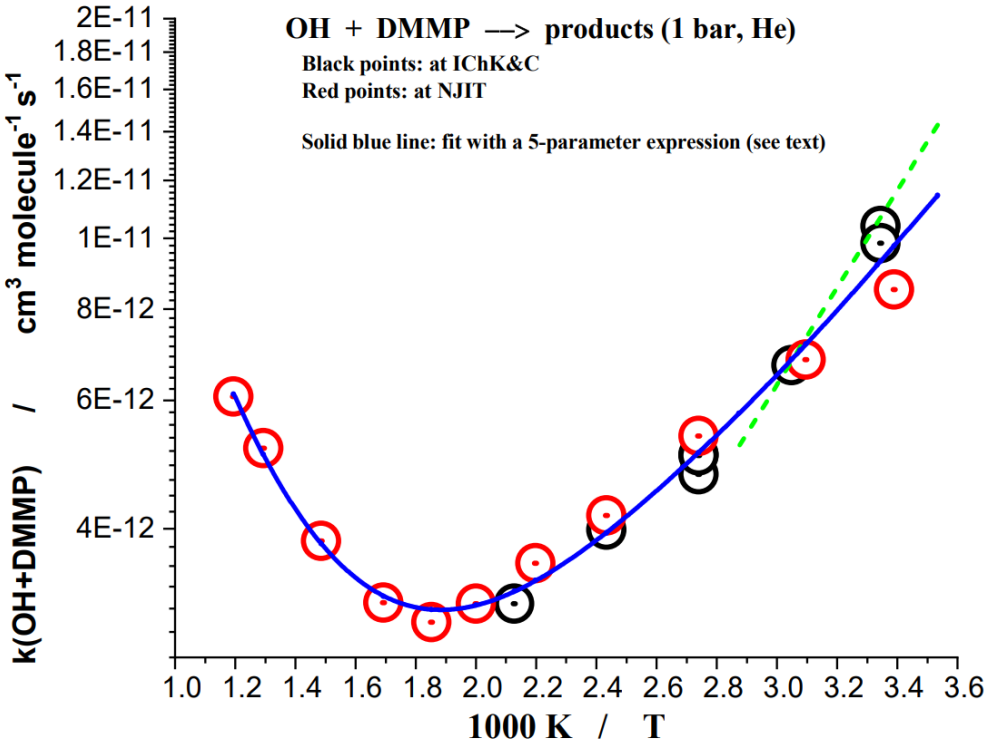

Figure 5.4 Summary of rate constant of reaction (OH+DMMP) at 1 bar, over the temperature range 298–837 K.

In Figure 5.6, red points: N_2O/H_2O/He + 193 nm, (at NJIT), black points: O_3/H_2O/He + 266 nm, (at ICKC). Blue line—fit by a 5-parameter expression (see text). Green dotted line: the only previous indirect experimental determination (relative rates method).

A standard 3-parameter modified Arrhenius expression was not sufficient to adequately fit the rate constant. A minimum of five parameters were required to achieve an accurate fit to the experimental data. The data was fitted using a 5-parameter expression, $k = A*T^n*\exp(-Ea_1/RT) + B*\exp(-Ea_2/RT)$, which is shown below:

$$k1 = 2.19 * 10^{-14} \left(\frac{T}{298}\right)^{2.43} \exp\left(\frac{15.02\ KJ\ mol^{-1}}{RT}\right) + 1.71 * 10^{-10} \exp\left(\frac{-26.51\ KJ\ mol^{-1}}{RT}\right) \quad \text{(E5.5)}$$

where A and B are the pre-exponential factors, Ea_1 and Ea_2 are the apparent activation energies of the potential reaction pathways.

Several measurements were conducted at elevated pressures and room temperature, the reaction conditions are shown in Table 5.2.

Table 5.2 Experimental Conditions and Rate Constant of Reaction OH + DMMP at RT, Varied Pressures

T / K	**P / bar**	**$[H_2O]/10^{17}$ molecule/cm^3**	**$[N_2O]/10^{16}$ molecule/cm^3**	**$[DMMP]/10^{14}$ molecule/cm^3**	**$k'/10^3$ s^{-1}**	**$k/10^{-12}$ molecule/cm^3/s**
295	3	3	4.11	0	0.826	
295	3	3	4.11	4.84	5.78	
295	3	3	4.11	3.87	4.695	
295	3	3	4.11	2.9	4	10.16
295	3	3	4.11	1.94	2.915	
295	3	3	4.11	0.97	2.083	
295	3	3	4.11	0	0.752	
292	10	3.4	9.29	0	1.901	
292	10	3.4	9.29	5.47	9.009	
292	10	3.4	9.29	4.38	8	
292	10	3.4	9.29	3.28	6.211	13.51
292	10	3.4	9.29	2.19	5.025	
292	10	3.4	9.29	1.09	3.049	
292	10	3.4	9.29	0	1.795	
290	30	3.85	27.81	0	5.376	
290	30	3.85	27.81	4.96	14.37	
290	30	3.85	27.81	3.97	12.48	
290	30	3.85	27.81	2.98	10.53	17.54
290	30	3.85	27.81	1.98	8.771	
290	30	3.85	27.81	0.99	7.299	
290	30	3.85	27.81	0	5.78	

The resulting rate constants were plotted vs the pressures, as shown in Figure 5.7. A positive pressure dependent rate constant was observed.

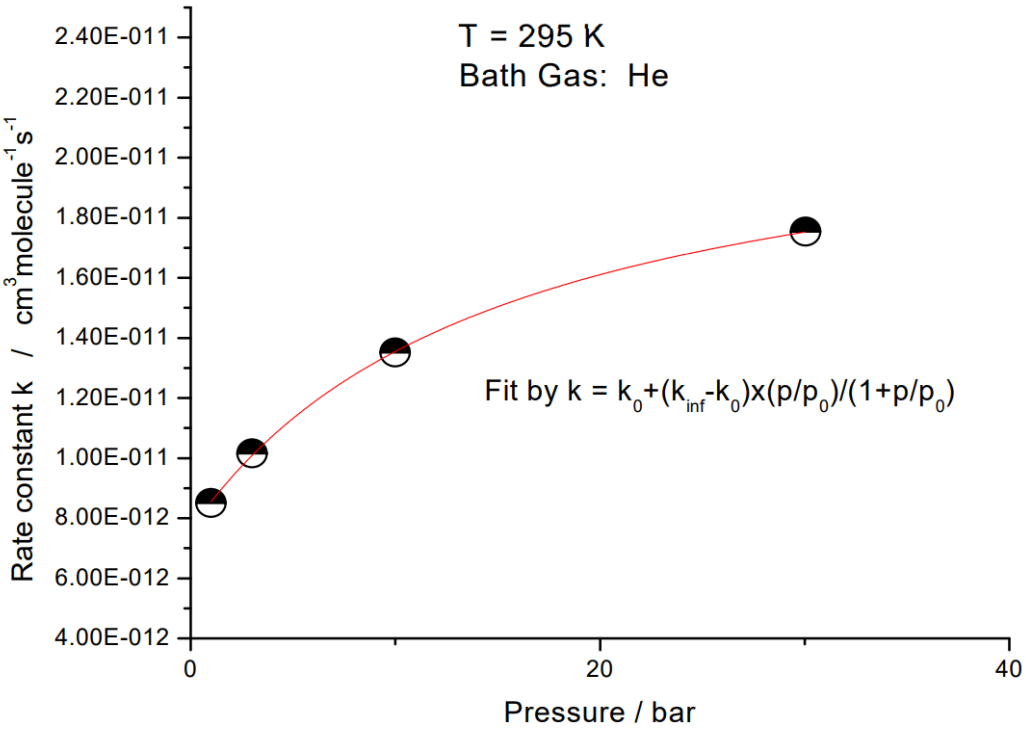

Figure 5.5 Pressure dependence of the rate constant of reaction (OH+DMMP).

In Figure 5.7, bath gas—He. Temperature 295 K. Smooth curve—fit using a simple model. Fitted parameters: $k_0 = (7.64 \pm 0.12) \times 10^{-12}$ $cm^3molecule^{-1}$ s^{-1}, $k_{inf} = (2.25 \pm 0.044) \times 10^{-11}$ $cm^3molecule^{-1}$ s^{-1} , and $p_0 = (15.2 \pm 1.2)$ bar.

5.5 Conclusion

Two research groups investigated the kinetics of the reaction between hydroxyl radical and dimethyl methylphosphonate, DMMP, using direct methods. The studies were conducted over a wide temperature range from 273 K to 837 K, and two different techniques were

employed to generate hydroxyl radicals. The rate constant at room temperature obtained from these studies is in agreement with the only previous indirect determination[111].

A clear V-shaped temperature dependence was observed, with a negative dependence at low temperatures and a positive dependence at higher temperatures, with a turning point at 530 ± 10 K. The rate constant was found to be significantly dependent on the pressure of the bath gas (He). These observations support the idea that the primary reaction pathway involves the abstraction of an H-atom from methoxy groups, with a reaction barrier that lies beneath the ground state of the reactants.

This was the first study that directly investigates the title reaction. The extended temperature range employed in this study enabled the discovery of the distinctive V-shaped temperature dependence. This was the second reaction of hydroxyl radicals with an organophosphorus compound that displays such behavior. To gain a better understanding of the mechanism of these reactions, more comprehensive experimental studies, including bath gas pressure dependence over an extended pressure and temperature range, as well as theoretical investigations, are necessary.

CHAPTER 6

OH+TMPi

6.1 Introduction

Trimethyl phosphite (TMPi) is an organophosphorus compound with the formula $P(OCH_3)_3$ that is phosphine in which the three hydrogens are replaced by methoxy groups. It is an alkylating agent used primarily in the synthesis of organophosphate compounds. Compared to trimethyl phosphate (TMP), it does not have P=O double bond, which makes it susceptible to oxidation to trimethyl phosphate.

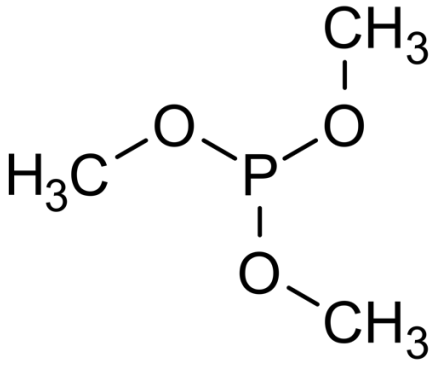

Figure 6.1 Structure of trimethyl phosphite.
Source:[94]

Trimethyl phosphite is a colorless liquid with a highly pungent odor. It is soluble in several organic solvents, such as ethanol, hexane, benzene, and carbon tetrachloride. Trimethyl phosphite (TMPi) was chosen as another organophosphorus compound reacting with OH radical. The result would help us to understand the reaction mechanism and what is the effect of P=O double bond, as well as different substituents.

$$TMPi + OH \rightarrow Products \qquad (6.1)$$

6.2 Experimental Approach

The overall experimental setup was the same as in Chapters 4 and 5, a heatable flow reactor combined with pulsed laser photolysis - UV/vis absorption technique was used. There are two major different preparations in Chapter 6. The first one is the concentration of trimethyl phosphite, since the title reaction rate is much faster than TMP and DMMP, a lower concentration of TMPi was used (ca. 20% of the value in TMP and DMMP measurements). Another difference is that pure TMPi was infused and carried to the reactor, instead of making a solution like what we treated TMP and DMMP. The main reason is that TMPi would react with water, making it impossible to dilute to an aqueous solution. Also, no suitable solvent can be used since the solvent should not interfere with UV absorption. A fluorinated hydrocarbon, perfluoro hexane, was used to dissolve TMPi initially, but experiments showed the solubility of TMPi was less than 0.05%; another issue is the oxygen dissolved in perfluoro hexane could react with TMPi, so a small infuse rate was used to inject pure TMPi in this work.

Our experiments showed TMPi is highly reactive. To prevent the possible reaction between water vapor and TMPi after evaporation part before entering the reactor, pure TMPi liquid was infused and carried to the reactor by helium bath gas directly (using a separate line), unlike in the TMP and DMMP measurements, which are mixed with water vapor and carrier gas (He) at a mixing point before carried to the reactor.

The concentrations of the precursors used at 1 bar were $(1.08 - 2.50) \times 10^{17}$ (H_2O), $(5.35 - 13.7) \times 10^{16}$ (N_2O) and $(3.89 - 37.0) \times 10^{13}$ (TMPi) molecules cm^{-3}.

6.3 Data Processing

Since the title reaction is much faster than TMP/DMMP + OH, the time-resolved profile is a little bit different, with a shorter OH lifetime. As shown in Figure 6.2, t_2 corresponds to the initial slope in this case. The rest of the data processing was the same as used in Chapters 4 and 5.

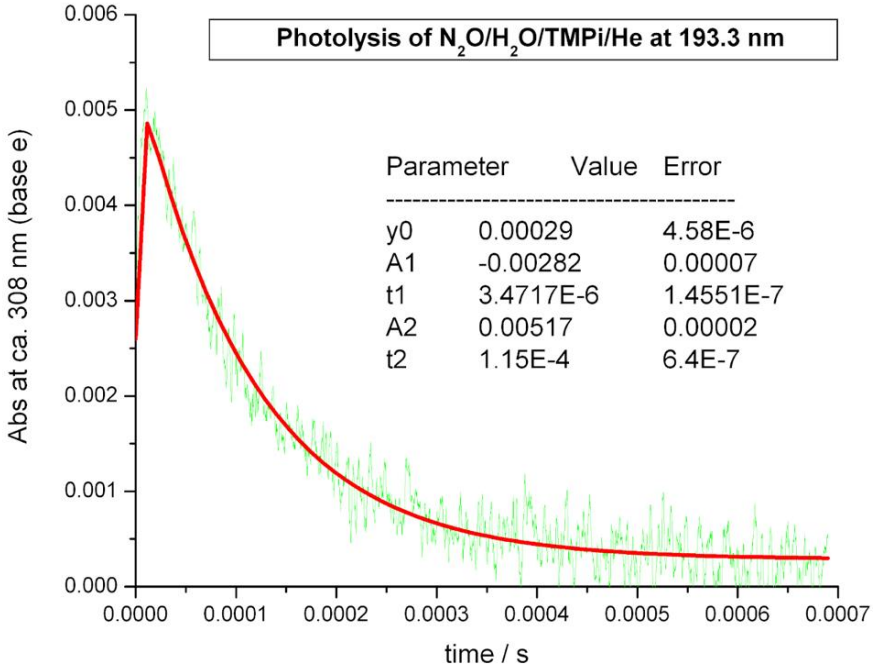

Figure 6.2 Sample OH radical absorption profile (green line) fitted with a 5-parameter first order decay curve (red line).

6.4 Results and Discussion

The reaction conditions of TMPi+OH are shown in Table 6.1. The measured temperatures ranged from room temperature to the upper limit, 837 K.

Table 6.1 Experimental Conditions and Rate Constant of Reaction TMPi + OH at 1 bar, Varied Temperatures

T / K	**P / bar**	**$[H_2O]/10^{17}$**	**$[N_2O]/10^{16}$**	**$[TMPi]/10^{14}$**	**$k'/10^3\ s^{-1}$**	**$k/10^{-11}$**
295	1.015	2.5	13.7	3	34.01	10.6
295	1.015	2.5	13.7	2.4	25.77	
295	1.015	2.5	13.7	1.8	17.45	
295	1.015	2.5	13.7	1.2	14.84	
295	1.015	2.5	13.7	0.6	7.87	
295	1.015	2.5	13.7	0	0.62	
323	1.02	1.78	7.27	2.68	23.47	8.28
323	1.02	1.78	7.27	2.14	17.51	
323	1.02	1.78	7.27	1.61	13.12	
323	1.02	1.78	7.27	1.07	8.47	
323	1.02	1.78	7.27	0.54	5.65	
323	1.02	1.78	7.27	0	0.45	
411	1.017	1.8	9.88	2.7	16.34	5.82
411	1.017	1.8	9.88	2.16	12.39	
411	1.017	1.8	9.88	1.62	8.47	
411	1.017	1.8	9.88	1.08	6.67	
411	1.017	1.8	9.88	0.54	3.02	
411	1.017	1.8	9.88	0	0.34	
500	1.028	1.79	8.19	2.24	10.04	4.5
500	1.028	1.79	8.19	1.79	7.75	
500	1.028	1.79	8.19	1.34	5.99	
500	1.028	1.79	8.19	0.89	3.44	
500	1.028	1.79	8.19	0.45	1.43	
500	1.028	1.79	8.19	0	0.24	
591	1.018	1.55	8.53	2.33	8.7	3.7
591	1.018	1.55	8.53	1.86	7.25	
591	1.018	1.55	8.51	1.39	5.24	
591	1.018	1.55	8.51	0.93	3.33	

Table 6.1 Experimental Conditions and Rate Constant of Reaction TMPi + OH at 1 bar, Varied Temperatures (Continued)

T / K	P / bar	$[H_2O]/10^{17}$ molecule/cm^3	$[N_2O]/10^{16}$ molecule/cm^3	$[TMPi]/10^{14}$ molecule/cm^3	$k'/10^3$ s^{-1}	$k/10^{-11}$ molecule/cm^3/s
591	1.018	1.55	8.51	0.46	1.83	
591	1.018	1.55	8.51	0	0.24	
657	1.003	1.37	7.53	3.09	10.45	
657	1.003	1.37	7.53	2.45	7.87	
657	1.003	1.37	7.53	1.85	6.06	3.29
657	1.003	1.37	7.53	1.23	4.37	
657	1.003	1.37	7.53	0.62	1.32	
657	1.003	1.37	7.53	0	0.52	
735	1.009	1.23	6.77	3.7	10.72	
735	1.009	1.23	6.77	2.96	8.55	
735	1.009	1.23	6.77	2.22	6.49	2.85
735	1.009	1.23	6.77	1.48	3.75	
735	1.009	1.23	6.77	0.74	1.93	
735	1.009	1.23	6.77	0	0.54	
782	1.003	1.15	6.33	2.59	8.4	
782	1.003	1.15	6.33	2.07	7.25	
782	1.003	1.15	6.33	1.56	5.62	3.05
782	1.003	1.15	6.33	1.04	3.62	
782	1.003	1.15	6.33	0.52	1.9	
782	1.003	1.15	6.33	0	0.94	
800	1.006	1.13	6.2	2.03	6.9	
800	1.006	1.13	6.2	1.69	5.71	
800	1.006	1.13	6.2	1.53	5.21	3.18
800	1.006	1.13	6.2	1.02	3.11	
800	1.006	1.13	6.2	5.08	1.67	
800	1.006	1.13	6.2	0	0.61	
818	1.006	1.11	6.07	2.49	9.62	3.65
818	1.006	1.11	6.07	1.99	7.09	

Table 6.1 Experimental Conditions and Rate Constant of Reaction TMPi + OH at 1 bar, Varied Temperatures (Continued)

T / K	P / bar	$[H_2O]/10^{17}$ molecule/cm^3	$[N_2O]/10^{16}$ molecule/cm^3	$[TMPi]/10^{14}$ molecule/cm^3	$k'/10^3$ s^{-1}	$k/10^{-11}$ molecule/cm^3/s
818	1.006	1.11	6.07	1.49	4.81	
818	1.006	1.11	6.07	0.99	3.57	
818	1.006	1.11	6.07	0.5	1.97	
818	1.006	1.11	6.07	0	0.23	
837	1.006	1.08	5.93	1.94	8.77	
837	1.006	1.08	5.93	1.55	6.8	
837	1.006	1.08	5.93	1.17	4.93	4.34
837	1.006	1.08	5.93	0.78	3.17	
837	1.006	1.08	5.93	0.39	1.88	
837	1.006	1.08	5.93	0	0.27	
837	1.009	1.08	5.95	2.44	10.62	
837	1.009	1.08	5.95	1.95	8.26	
837	1.009	1.08	5.95	1.46	6.17	
837	1.009	1.08	5.95	0.97	3.62	4.21
837	1.009	1.08	5.95	0.49	2.25	
837	1.009	1.08	5.95	0	0.37	

A OH radical sample UV absorption profiles are shown in Figure 6.3. The initial amplitudes of the signal were kept approximately the same, only the [TMPi] varied with 5 intervals.

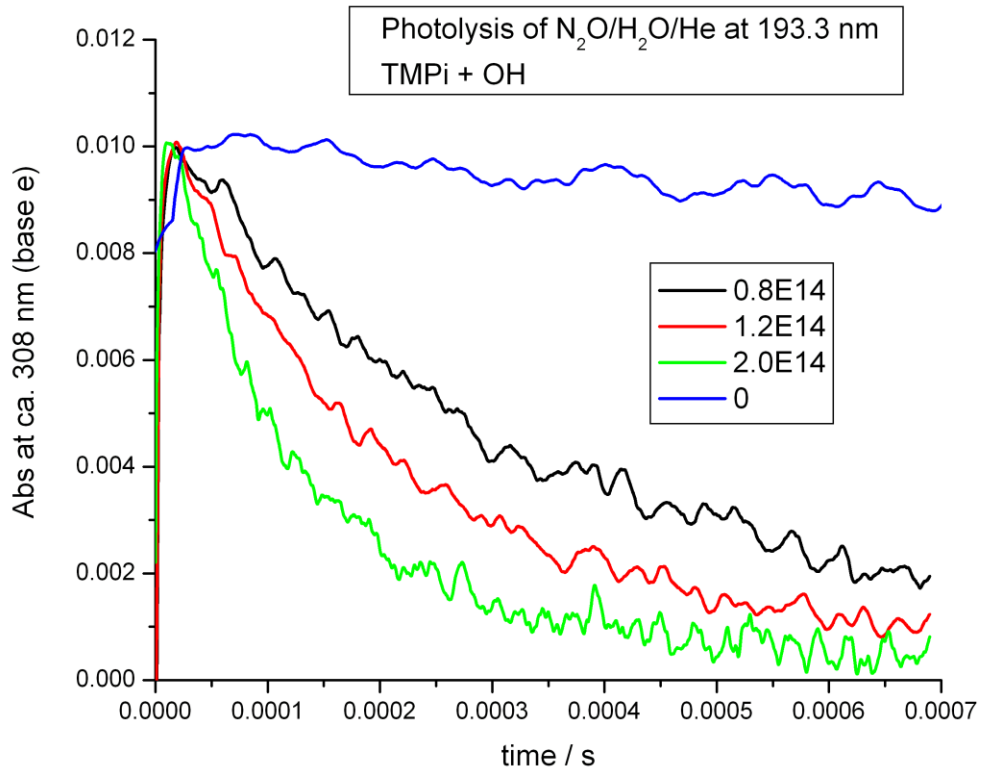

Figure 6.3 Sample UV absorption profiles of OH radical (multiline at ca. 308 nm). Photolysis of $N_2O/H_2O/TMPi/He$ mixture at 193.3 nm. T = 591 K, p = 1 bar.

The reactants' concentrations in Figure 6.3 are: $[N_2O] = 8.51 \times 10^{16}$ molecules cm^{-3}, $[H_2O] = 1.55 \times 10^{17}$ molecules cm^{-3}, $[N_2O]/[H_2O] = 0.55$, [TMPi] = 0.93 – 2.33 × 10^{14} molecules cm^{-3}. The initial concentration of OH is approximately the same. Green- [TMPi] = 2.0 × 10^{14} molecules cm^{-3}, red- [TMPi] = 1.2 × 10^{14} molecules cm^{-3}, black- [TMPi] = 0.80 × 10^{14} molecules cm^{-3}, blue- [TMPi] = 0.

Each decay curve in Figure 6.3 resulted in a k'. k' was plotted vs [TMPi], a linear fit gave a corresponding rate constant of TMPi+OH, an example is shown in Figure 6.4.

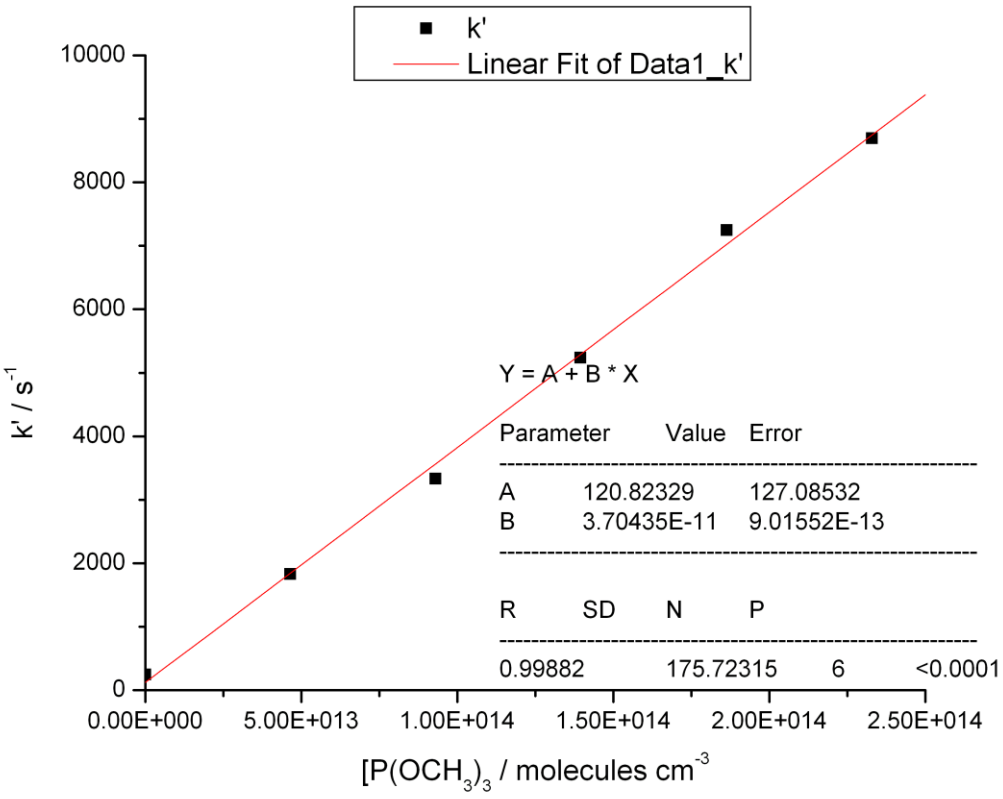

Figure 6.4 Sample initial slope k' of a series of measurements (at 591 K, 1 bar), versus [TMPi].

The reactants' concentrations were kept constant, except [TMPi] ranged from 0.46 to 2.33 × 10^{14} molecules cm^{-3}, with 5 intervals controlled by the infuse rate of TMPi. The linear fit of k' vs [TMPi] gave the reaction rate constant k(TMPi+OH), a summary of these plots is shown in Figure 6.5.

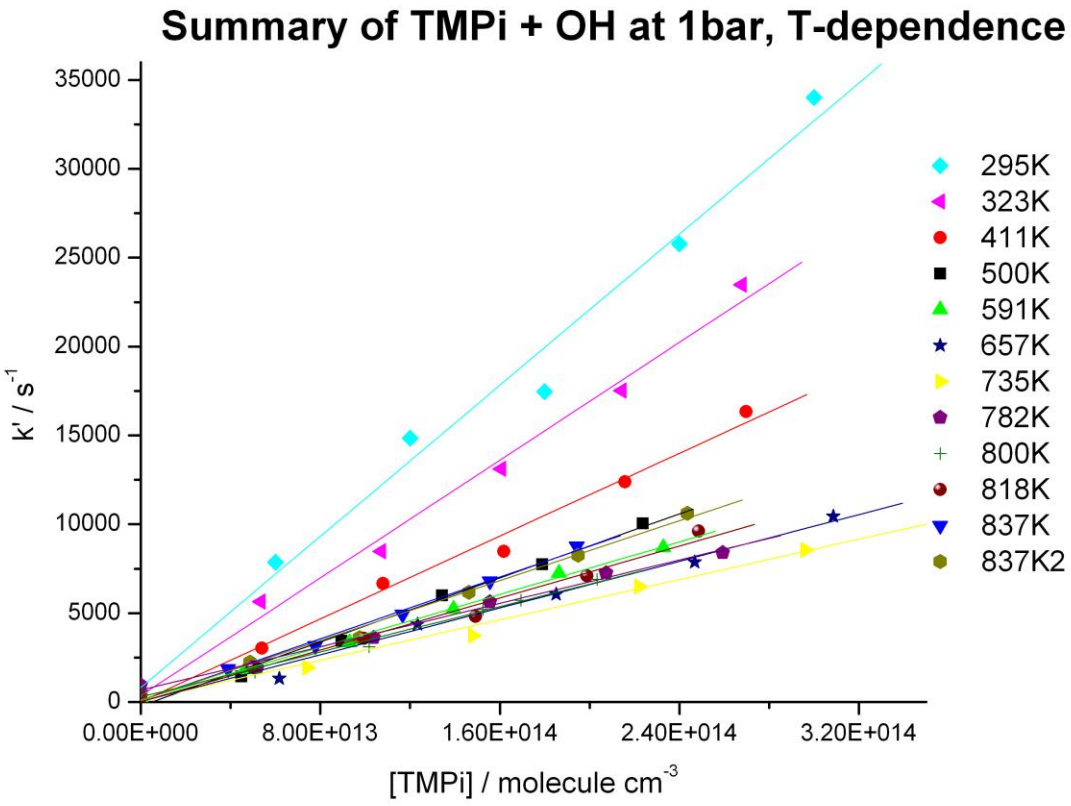

Figure 6.5 Summary of k' vs [TMPi] at different temperatures.

The resulted rate constants from Figure 6.5 were plotted vs 1000 K/T, where T is the temperature in K. The result is shown in Figure 6.6. A V-shaped temperature dependent rate constant of reaction TMPI+OH was observed, with a much higher turning point compared with TMP and DMMP.

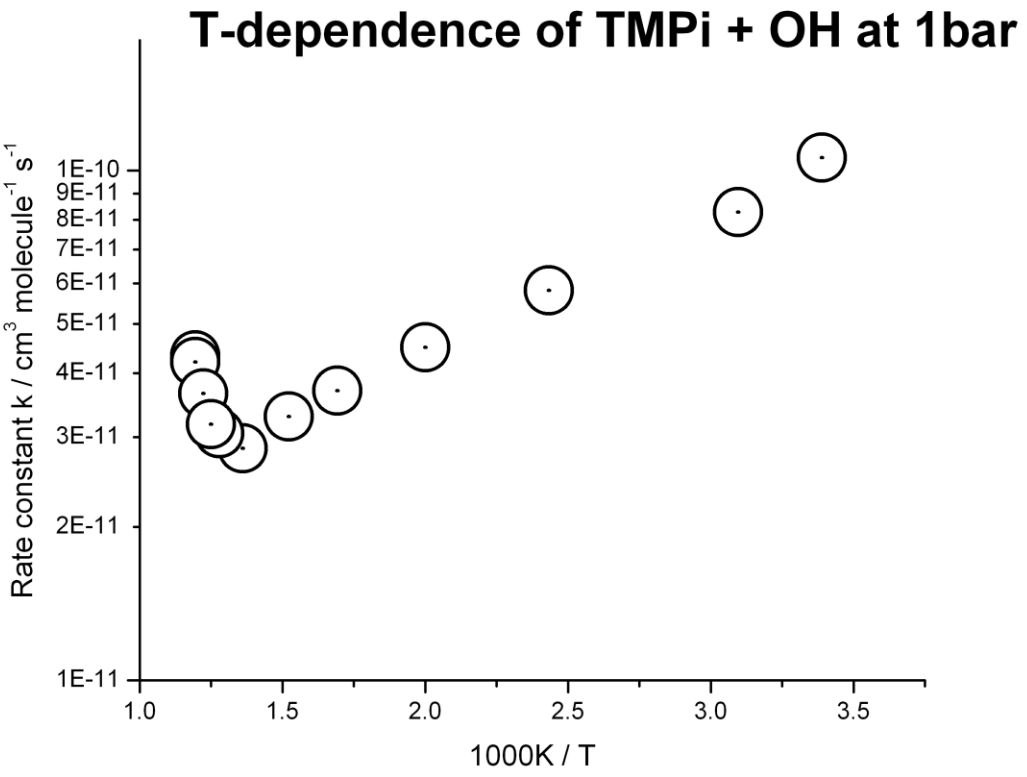

Figure 6.6 Summary of rate constant of reaction (OH+TMPi) at 1 bar, over the temperature range 298–837 K.

6.5 Conclusion

This work investigated the temperature-dependent kinetics of the reaction between hydroxyl radical and trimethyl phosphite, TMPi. The studies were conducted over a wide temperature range from 295 K to 837 K, the reaction rates are one order of magnitude higher than the previous two organophosphorus compounds, Trimethyl phosphate (TMP) and Dimethyl methylphosphonate (DMMP). Trimethyl phosphite also shows a V-shaped temperature dependent rate constant, a turning point at 735 ± 10 K was observed.

The study presented here is the inaugural investigation of the titled reaction using direct methods. The expanded temperature range employed in this study allowed for the

identification of the unique V-shaped temperature dependence, which is the third instance of a hydroxyl radical reaction with an organophosphorus compound displaying this behavior.

CHAPTER 7

DISCUSSION

Chemical reactions involve breaking of old bonds and forming of new bonds, as shown in Figure 7.1, where the resulting barrier along the reaction pathway represents an intermediate which has a higher energy than the reactants.

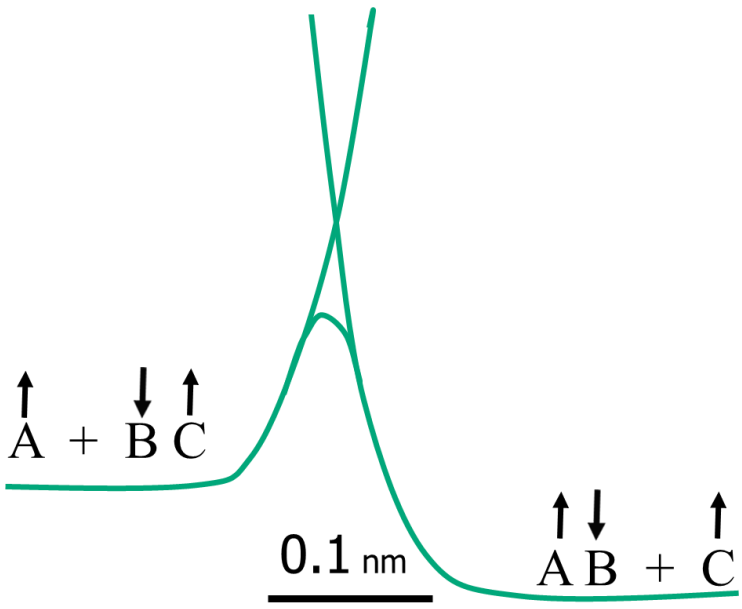

Figure 7.1 Energy diagram during a reaction.

For most chemical reactions, the activation energy is a positive value, their rate constants would increase when temperature increases. Our experimental results show a negative temperature dependent rate constant for all three organophosphorus compounds, which indicates a negative activation energy is present.

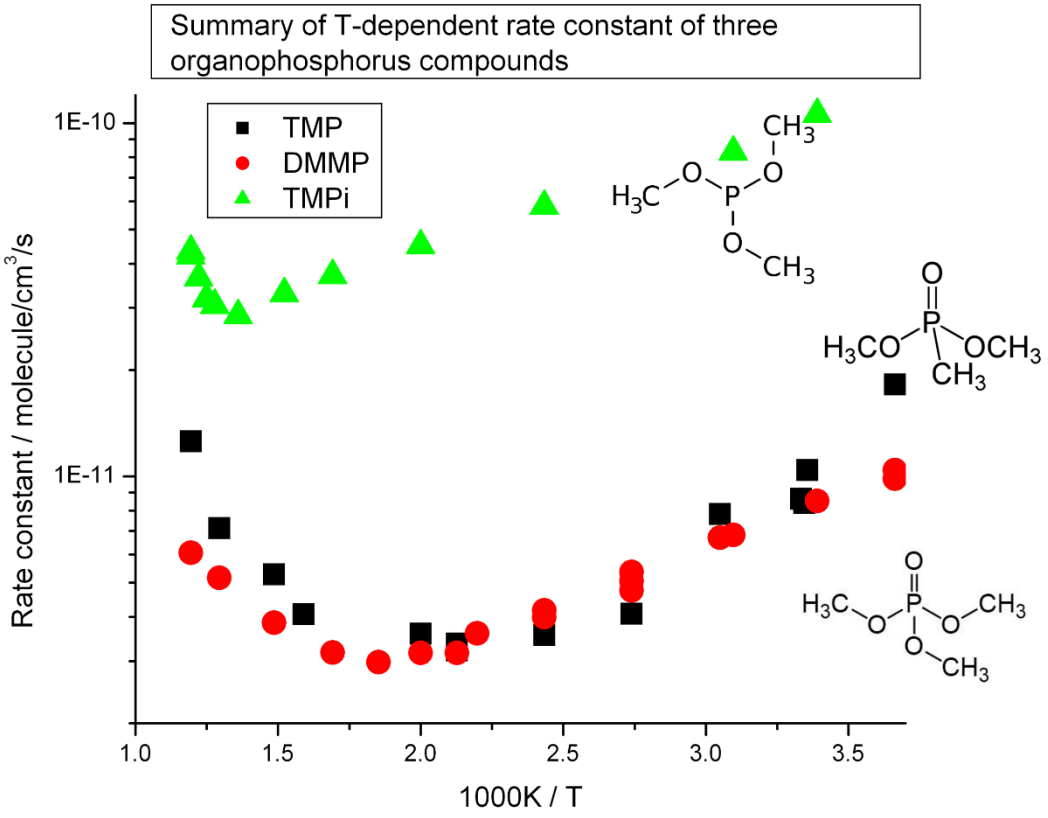

Figure 7.2 Summary of the temperature dependent rate constant of three organophosphorus compounds.

In Figure 7.2, TMPi has a much faster reaction rate than that of TMP and DMMP. This can be explained by the reactivity of TMPi, since the oxidation state of P atom in the TMPi is 3, making it easier to react with OH radicals. Its V-shaped temperature dependence is a result of H-abstraction channel and the channel that OH attached to P atom directly.

For DMMP, a methoxy group is replaced by a methyl group (compared to TMP), which will lead to a different C-H bond strength (C atom attached to P atom directly), as well as a different H-abstraction reaction rate.

These non-Arrhenius plots can be explained by assuming that an intermediate complex is formed, which allows the rate determining step to have a transition state with small and negative potential energy relative to the reactants. When the temperature increases, the vibrational energy of the transition state becomes significant and the plot curves upward.[44]

Another possible reaction pathway is the opening of the P=O double bond and attachment of the OH to the P atom directly. This process may have a positive barrier due to the steric effect, which may contribute to the positive temperature dependence after the turning point.

CHAPTER 8

CONCLUSIONS

The latest experimental findings indicate that k(TMP+OH), k(DMMP+OH), and k(TMPi+OH) exhibit a temperature-dependent V-shape pattern, where they are negative at low temperatures and positive at high temperatures. This phenomenon could be attributed to two potential explanations. One explanation is that the transition state's ground state is positioned beneath the reactants' ground state, resulting in a negative barrier. Under these circumstances, a modified transition state theory predicts a V-shape temperature dependence, with the possibility of pressure dependence at high pressures.[46, 112] Another possibility is that these reactions have two or more reaction channels, such as H-atom abstraction from CH_3 groups (as discussed in the theoretical paper) and OH attachment to the P=O double bond in TMP and DMMP.

The disproportionation channel of OH+OH was published in 2020. The temperature dependence of OH+TMP was published in 2021. The temperature dependence as well as the pressure dependence (up to 30 bar) of OH+DMMP has been published in 2022. The temperature dependence of OH+TMPi is in preparation stage. The complete pressure dependence measurements of these reactions are not finished yet. While from the current data we have, a positive pressure dependent rate constant is clear. Further experiments (pressure dependence measurements and other phosphorus centered compounds) as well as theoretical studies are required to understand the reaction mechanism better.

APPENDIX

SCIENTIST MODEL

The following model was constructed in SCIENTIST software, which yielded the rate constant of OH+OH (Chapter 3).

```
// production of H2O2 from the wall reaction added 05/14/19 LK
// 04/18/19 slightly modified version 04/27/19 for NJIT conditions
// 042717 this transform fits k(OH+OH) for given sOHat308. L Krasnoperov, 042717
//1215new.eqn
//Reactions of O2(1SIGMA) are added!
//Important in actinometry!!
//Based on:
//OH_ozone.eqn   L. Krasnoperov 11/11/16
//Processing OH profiles obtained by photolysis of N2O/H2O/He mixtures at 193.3 nm
//based on OHwithO2.eqn.   O3 profiles processing, version 3. L Krasnoperov, 03/13/12
//Reversible reaction O + O2 <=> O3. Not required here, rudiment
// Calculation of the initial concentration of transients is here
//Recording OH at 308 nm, O3 at 253.6 nm

//Troe Formalizm Functions Definitions:
// It looks like that User Defined Functions do not work properly!!!
//This is for the reference only (just replace rxn with the reaction number!):

//k0rxn= (expression for k0)
//kinfrxn=(expression for kinf)
//Fcentrxn=(expression for Fcent)
//xrxn=k0rxn*M/kinfrxn
//crxn=-0.4-0.67*Log10(Fcentrxn)
//Nrxn=0.75-1.27*Log10(Fcentrxn)
//d=0.14
//yrxn=Log10(xrxn)+crxn
```

//LFrxn=Log10(Fcentrxn)/(1+(yrxn/(Nrxn-d*yrxn))^2)
//Frxn=10^LFrxn
//krxn=kinfrxn*Frxn*xrxn/(1+xrxn)

// Notations:
// CC-chemical compound
// Reactant Concentrations placed in the reactor are labeled with "0" subscript , CC_0 (like O2_0)
// Changes of the concentrations after photolysis are labeled as DeltaCC_1, (like DeltaO3_1)
// Concentrations after photolysis are labeled as CC_1
// Changes of the concentrations caused by reactions with O(1D) are labeled as DeltaCC_2
// Concentrations after consumption of all O(1D) are labeled CC_2
// Changes of the concentrations caused by reactions of O2(1Sigma) are labeled as DeltaCC_3
// Concentrations after all fast processes (which are the initial conditions for the ODE system) are labeled with "ini", CCini
//
// No index - current concentrations used in the ODE system, like HO2

// Time should be in the 1-st column, signal (absorbance) - in 2-nd and 3-rd

IndVars: TIME,SIGNAL1
DepVars: SIGNAL, OHini, kprime
Params: PhotonFluence_0, k4a

// Only information between the two solid lines may be changed
// from experiment to experiment
//_____
// Conditions/Time Window for fit (all in sec)

```
//Time Window for fit (all in sec)

t1=1.3e-3
t2=8e-3

//Path length (cm)
L=10.0
// Conditions:

// Pressure in Torr
//04/11/19/14
pr=7.483
T=298.15
N2O_0=1.57E16
H2O_0=1.60079E17
v=143.05277*1.10

//velocity for 7 mm ID is 1.10 times larger

N2_0=0
O3_0=0
O2_0=0

// Photon Fluence at the  entrance of the reactor labeled as PhotonFluence_0

//PhotonFluence_0=3.189e15


kwOH=28
//kwOH=0

ZeroShift308=0
ZeroShift253=0
//Decay on Windows correction (diffusion controlled)
```

```
//CorrFactor3=0.03418*exp(-47.585*tr)+0.0154*exp(-433.26975*tr)+0.94587-
1.11133*tr
//This is valid for delta=D/(vL) = 0.036
//where tr = t*v/L is the Reduced Time
//flush-out is included in this function

//
//_____________________________________________________________

p=pr/750
M=p*2.429e19*298.15/T



// Reaction Mechanism

//"Instantaneous" processes (happening on μs/sub-μs time scale)

// Photolysis (instantaneous):
// O3 + hv -->O(1D) + O2              (Fi1)
// O3 + hv--> O   +   O2                        (Fi2)

// O(1D) processes (sub-μs time scale)

// O(1D)+H2O -->   2 OH                         (1a)
// O(1D)+H2O--> H2 +O2              (1b)
// O(1D)+O2 --> O + O2SIGMA                     (2a) f2a
// O(1D)+O2 --> O + O2                          (2b) f2b
// O(1D)+O3 --> O +O +O2            (3a)
// O(1D)+O3 --> O2   + O2           (3b)
// O(1D)+O3 --> O + O3                          (3c)
// O(1D)+N2 --> O + N2                          (400)

// O2(1Sigma) Reactions. (10 μs time scale)
```

// Only relevant processes are considered
// O2SIGMA == O2(1Sigma)

// O2SIGMA+O2--> products (300)
// O2SIGMA + N2 --> products (301)
// O2SIGMA+O3 --> O + 2O2 (302)
// O2SIGMA + H2O --> O2+H2O (303)
// O2SIGMA + O --> products (304)

//Reaction timescale processes including reactions with ozone (100 usec - 10 ms time scale)

// OH+OH --> H2O + O (4a)
// OH+OH --> H2O2 (4b)
// OH + O --> O2 +H (7a)
// OH + O --> HO2 (7b)
// OH + H --> H2 + O (8a)
// OH + H --> H2O (8b)

// OH + H2O2 --> H2O + HO2 (14)
// OH + HO2 --> H2O + O2 (15)
// O + HO2-->O2+OH (19)
// O + H2O2--> OH + HO2 (20)
// H + HO2 --> H2 +O2 (21a)
// H + HO2 --> 2 OH (21b)
// H + HO2 --> H2O + O (21c)
// H + HO2 --> O(1D) +H2O (21d)

// O + O2 --> O3 (30) reversible
// H + O2 --> OH + O (31a)
// H + O2 --> HO2 (31b)
// HO2 + O2 --> OH + O3 (32)

// OH +O3 --> HO2 + O2 (35)
// O + O3 --> O2 + O2 (36)
// H + O3 --> OH + O2 (37)
// HO2 + O3 --> OH + O2 + O2 (38)

//Cross-sections and Quantum Yields
// Photolysis of O3 at 266 nm,1 bar, 298 K: Cross-section 0.84e-17, Fi(O(1D))=0.9, Fi(O)=0.1 (JPL 10-6)

//Fi1aat266=0.9
//Fi1bat266=0.1

Fi1at193=1.0
Fi2at193=0

//Relevant cross-sections (references yet to be added!!!!)

//At 308 nm:
sOHat308=5.05e-17
sO3at308 =11.2e-20

// HO2 and H2O2 absorptions at 308 are negligible, set to zero:
sHO2at308=0
sH2O2at308=0

//At 253.6 nm:
sO3at253=1.148e-17*(T/298)^(-0.2303)
sH2O2at253=7.1e-20
sHO2at253=32.4e-20

//At 266 nm (JPL-10-6)
sO3at266=0.84e-17

```
// At 193.3 nm (JPL-10-6) at 298 K:
sN2Oat193=8.70e-20

//Rate Constants of O(1D) Reactions

// O(1D)+H2O -->  2 OH                    (1a)
//k1a= 1.7e-10*exp(36/T) (Vranckx et al.PCCP, 2010)

k1a=1.7e-10*exp(36/T)

//O(1D)+H2O--> H2 +O2                    (1b)
//Vranckx et al, 2010, k1b= 2.2 e -12
k1b=2.2e-12

// Quenching on water is < 0.003 of the totals (Carl, 2005), and is neglected.

//O(1D)+O2 --> O + O2(1Sigma)                (2a)
//O(1D)+)2 --> O + O2                        (2b)
//k2= 3.3e-11exp(55/T)  k298 =  3.95e-11   (JPL 10-6, 2011)
k2= 3.3e-11*exp(55/T)

//According to JPL-15, f2a=0.8 +- 0.2
f2a=0.8
f2b=0.2

k2a=k2*f2a
k2b=k2*f2b


//O(1D)+O3 --> O +O +O2          (3a)
// Note: these are really two accidently equal rate constants, the total is 2.4e-10 (JPL 10-6)
//k3a=1.2e-10    (JPL 10-6)
k3a=1.2e-10
```

//O(1D)+O3 --> O2 + O2 (3b)
//k3b=1.2e-10 (JPL 10-6)
k3b=1.2e-10

//O(1D)+O3 --> O + O3 (3c)
//This channel (3c) is NOT mentioned in the JPL evaluation, is not considered.
//Therefore, the yield of O-atoms from reaction with ozone is 1.0 for every O(1D) reacted with O3

//O(1D)+N2 --> O + N2 (400)
// note insertion O(1D)+N2 --> N2O is termolecular 2.8e-36*(T/300)^0.9 is not important at low pressures
// JPL-15 k400=2.5e-11*exp(110/T)
k400=2.5e-11*exp(110/T)

// O2(1Sigma) Reactions. Only relevant processes are considered. All - from JPL-15 evaluation, except when indicated otherwise.

// O2SIGMA+O2--> products (300)
k300=3.9e-17

// O2SIGMA + N2 --> products (301)
k301=1.8e-15*exp(45/T)

// O2SIGMA+O3 --> O + 2O2 (302)
// 2005DUN/TAL3912-3920
k302=3.63e-11*exp(960/8.31447/T)

// O2SIGMA + H2O --> O2+H2O (303)
// 2005DUN/TAL3912-3920
k303=4.52e-12*exp(740/8.31447/T)

// O2SIGMA + O --> products (304)
k304=8e-14

```
//Rate constants:

//k4a:   OH+OH --> H2O + O                    (4a)
// 2011 Sangwan et al.
// Low T <420K 1999 Bedjanian et al, high T>550K   - our data 2011
// fit of the data that were submitted in the final version
//k4a=1.07e-12*(1+1.0e-4*((T-483)^2))^0.2
//k4a=1.4e-12

// k4b:  OH+OH --> H2O2                       (4b)
// 2011 Sangwan et al.

k04b=9.0e-31*(T/300)^(-3.5)
kinf4b=2.4e-11*(T/300)^(-0.5)
Fcent4b=0.37
x4b=k04b*M/kinf4b
c4b=-0.4-0.67*Log10(Fcent4b)
N4b=0.75-1.27*Log10(Fcent4b)
d=0.14
y4b=Log10(x4b)+c4b
LF4b=Log10(Fcent4b)/(1+(y4b/(N4b-d*y4b))^2)
F4b=10^LF4b
k4b=kinf4b*F4b*x4b/(1+x4b)
//This generates k4b=4.4e-12 at 1 bar and 298 K
// Our direct value is (6.2-1.4)e-12

//OH + O -->   O2    +H                      (7a)
// 2004 ATK/BAU
k7a=2.4e-11*exp(109/T)


// OH + O --> HO2                             (7b)
// No data, set as OH+H
```

k7b=M*1.6e-31*(T/298)^(-2.6)

//OH + H --> H2 + O (8a)
//86TSA/HAM
k8a = 6.86e-14*(T/298)^2.8*exp(-1950/T)

//OH + H --> H2O (8b)
//77 ZEL/ERL
k8b=M*1.6e-31*(T/298)^(-2.6)

// OH + H2O2 --> H2O + HO2 (14)
//2004JIM/GIE
k14=2.9e-12*exp(-109/T)

// OH + HO2 --> H2O + O2 (15)
//1988KEY
k15=4.8e-11*exp(250/T)

//O + HO2-->O2+OH (19)
//2004ATK/BAU
k19= 2.70E-11*exp(1860/8.31447/T)

//O + H2O2--> OH + HO2 (20)
//2004ATK/BAU
k20 =1.40E-12*exp(-16630/8.31447/T)

//H + HO2 --> H2 +O2 (21a)
//1992 BOU/COB
k21a=7.11E-11*exp(-5900/8.31447/T)

//H + HO2 --> 2 OH (21b)
//1992Bau/COB
k21b=2.81E-10*exp(-3660/8.31447/T)

```
//H + HO2 --> H2O + O                    (21c)
//1992 BAU/COB
k21c=5.00E-11*exp(-7200/8.31447/T)

//H + HO2 --> O(1D) +H2O                 (21d)
//2007MOU/SAH1901-1913
// A theoretical paper - important reaction, thou!
// Will be used as H + HO2 --> 2OH +H2O
k21d=3.29E-12*(T/298)^1.55*exp(670/8.31447/T)

// O + O2 --> O3                         (30)
// Hippler, Rahn, Troe 1990 (on He)
k30 = M*3.4e-34*(T/300)^(-1.2)*k30Factor

// Hippler, Rahn, Troe 1990 (on N2)
//k30=M*5.51e-34*(T/298)^(-2.60)

//Equilibrium constant from dHf298(O3)=141.746 kJmol-1
//(from Active Thermo Tables), O and O2 fro GRI, and
// the rest for ozone from NIST Webbook.
Keq30=4.0007e-9*(T/298)^(-1.37313)*exp(14123.53/T)
kfkr30=Keq30*10*8.31451*T/6.022e23


// H + O2 --> OH + O                     (31a)
//1994 Bau/Cob
//Plays a role only at high T
k31a = 1.62E-10*exp(-62110/8.31447/T)

// H + O2 --> HO2                        (31b)
// 1997ATK/BAU (for N2):
k31b = M*5.4E-32*(T/298)^(-1.80)
```

```
// HO2 + O2 --> OH + O3                    (32)
// This reaction is ENDOTHERMIC by ca. 180 kJ mol-1
// Play absolutely no role
k32=0

// OH +O3 --> HO2 + O2                     (35)
// 2004 ATK/BAU
k35 = 1.7E-12*exp(-7820/8.31447/T)

// O + O3 --> O2 + O2                      (36)
// 2001 ATK/BAU
k36=8.0E-12*exp(-17130/8.31447/T)

// H + O3 --> OH + O2                      (37)
// 1989 ATK/BAU
k37=1.4E-10*exp(-3990/8.31447/T)

// HO2 + O3 --> OH + O2 + O2               (38)
// 2004 ATK/BAU
k38 =1.97E-16 *(T/298)^4.57*exp(5760/8.31447/T)

// Photolysis and the fate of O(1D)

// N2O+hv(193)-->O(1D)+N2                  (Fi1at193)
// N2O+hn(193)-->O+N2                      (Fi2at193)

// O(1D)+H2O -->  2 OH                     (1a)
//O(1D)+H2O--> H2 +O2                      (1b)
//O(1D)+O2 --> O + O2(1Sigma)              (2a)
// O(1D) + O2 --> O + O2                   (2b)
//O(1D)+O3 --> O +O +O2          (3a)
//O(1D)+O3 --> O2  + O2                    (3b)
//O(1D)+O3 --> O + O3                      (3c) neglected - not mentioned anywhere
//O(1D)+N2 --> O + N2                      (400)
```

// O2(1Sigma) Reactions. Only relevant processes are taken into account

// O2SIGMA+O2--> products (300)
// O2SIGMA + N2 --> products (301)
// O2SIGMA+O3 --> O + 2O2 (302)
// O2SIGMA + H2O --> O2+H2O (303)
// O2SIGMA + O --> products (304) this process is neglected

//Calculation of Average Photon Fluence along the reactor

A193=sN2Oat193*N2O_0*L
PhotonFluenceAve=PhotonFluence_0*(1-exp(-A193))/A193

// Calculation of the Initial Conditions

//Reactants with constant concentrations
O2=O2_0
N2=N2_0
N2O=N2O_0
H2O=H2O_0

// Stage 1. Photolysis at 193 nm.
//DeltaO3_1=-PhotonFluenceAve*sO3at266*O3_0
DeltaO3_1=0
DeltaOH_1=0
O3_1=O3_0+DeltaO3_1
//O1D_1=-DeltaO3_1*Fi1aat266
//DeltaO_1=-DeltaO3_1*Fi1bat266

DeltaN2O_1=-PhotonFluenceAve*sN2Oat193*N2O_0
O1D_1=-DeltaN2O_1*Fi1at193

```
DeltaO_1=-DeltaN2O_1*Fi2at193

// Stage 2. Reactions of O(1D)

TotalQuenchO1D = (k1a+k1b)*H2O+(k2a+k2b)*O2+(k3a+k3b)*O3_1+k400*N2
DeltaO_2 =O1D_1*(2*k3a*O3_1+(k2a+k2b)*O2+k400*N2)/TotalQuenchO1D
DeltaOH_2=O1D_1*2*k1a*H2O/TotalQuenchO1D
DeltaO2SIGMA_2=O1D_1*k2a*O2/TotalQuenchO1D
O2SIGMA_2=0+DeltaO2SIGMA_2
DeltaO3_2=-O1D_1*(k3a+k3b)*O3_1/TotalQuenchO1D
O3_2=O3_1+DeltaO3_2


// Stage 3. Reactions of O2(1Sigma)

TotalQuenchO2Sigma=k300*O2+k301*N2+k302*O3_2+k303*H2O
DeltaO3_3=-O2SIGMA_2*k302*O3_2/TotalQuenchO2Sigma
DeltaO_3 = O2SIGMA_2*k302*O3_2/TotalQuenchO2Sigma
DeltaOH_3=0


// Initial Concentrations:

O3ini=O3_0+DeltaO3_1+DeltaO3_2+DeltaO3_3
Oini=0+DeltaO_1+DeltaO_2+DeltaO_3
OHini=0 +DeltaOH_1+DeltaOH_2+DeltaOH_3

HO2ini=0
H2O2ini=0
Hini=0

// Diffusion coefficient 0.88 bar cm2 s-1 according to Ivanov et al. at 296
// Temperature dependence T^1.6 is ASSUMED
//0.146 is R^2 (R =0.76 cm/2)
```

```
kwO=0
kwH=0
kwHO2=0

//Species transient:  OH,  O,  H, H2O2, HO2, O3
//Species stable:  O2, H2O, He, N2O

//Equations:


r4a=k4a*OH*OH
r4b=k4b*OH*OH
r7a=k7a*OH*O
r7b=k7b*OH*O
r8a=k8a*OH*H
r8b=k8b*OH*H
r14=k14*OH*H2O2
r15=k15*OH*HO2
r19=k19*O*HO2
r20=k20*O*H2O2
r21a=k21a*H*HO2
r21b=k21b*H*HO2
r21c=k21c*H*HO2
r21d=k21d*H*HO2
r30=k30*(O*O2-O3/kfkr30)
r31a=k31a*H*O2
r31b=k31b*H*O2
r32=k32*HO2*O2
r35=k35*OH*O3
r36=k36*O*O3
r37=k37*H*O3
r38=k38*HO2*O3
```

```
//r300=k300*O2SIGMA*O2
//r301=k301*O2SIGMA*N2
//r302=k302*O2SIGMA*O3
//r303=k303*O2SIGMA*H2O
//r304=k304*O2SIGMA*O

//Initial Conditions

TIME=0

O=Oini
H=Hini
H2O2=H2O2ini
HO2=HO2ini
//delta=0.1
//tau=0.1e-3
PhotonFluence_0>0
//k4a>0
kwOH>0
***
O3=O3ini
OH=OHini

// ODE system

//O2SIGMA'=-r300-r301-r302-r303-r304
OH'=-2*r4a-2*r4b-r7a-r7b-r8a-r8b-r14-r15+r19+r20+2*r21b+2*r21d+r31a+r32-
r35+r37+38-kwOH*OH
O'=r4a-r7a-r7b+r8a-r19-r20+r21c-r30 +r31a-r36-kwO*O
H'=r7a-r8a-r8b-r21a-r21b-r21c-r21d-r31a-r31b-r37-kwH*H
H2O2'=r4b-r14-r20+kwOH*OH/2
HO2'=r7b+r14-r15-r19+r20-r21a-r21b-r21c-r21d+r31b-r32+r35-r38
O3'=r30+r32-r35-r36-r37-r38
```

```
O3trans=O3-O3_0

AbsO3at253 =L*sO3at253*O3trans
AbsHO2at253=L*sHO2at253*HO2
AbsH2O2at253=L*sH2O2at253*H2O2

AbsOHat308=L*sOHat308*OH
AbsO3at308 =L*sO3at308*O3trans
AbsHO2at308=L*sHO2at308*HO2
AbsH2O2at308=L*sH2O2at308*H2O2

Abs253=AbsO3at253+AbsHO2at253+AbsH2O2at253
Abs308=AbsOHat308+ AbsO3at308+AbsHO2at308+AbsH2O2at308

//Flush-out correction
Correction=1-TIME*v/L
CorrFactor=IFGEZERO(Correction,Correction,0)

//Radial spreading approximate correction
//CorrFactor2=1-delta*(1-exp(-TIME/tau))

//Diffusion controlled decay on windows + flush-out
k30Factor=1
//kwOH=21
//tr=time*v/L
//CorrFactor3=0.03418*exp(-47.585*tr)+0.0154*exp(-433.26975*tr)+0.94587-
1.11133*tr
Abs308corr=Abs308*CorrFactor
//Abs308corr=Abs308*CorrFactor*CorrFactor2
//Abs253corr=Abs253*CorrFactor*CorrFactor2

F1=SIGNAL1
```

```
Abs308corr=Abs308*CorrFactor
//Abs253corr=Abs253*CorrFactor


//F2=Abs253corr
F2=Abs308corr+ZeroShift308
gate=UNIT(TIME-t1)*UNIT(t2-TIME)
SIGNAL=(1-gate)*F1+gate*F2


kprime=OHini*k4a

//Initial Parameters and Constraints


k4a=1.4e-12
PhotonFluence_0=2e16

//k30Factor=1.25
```

REFERENCES

1. Miller, J. A.; Pilling, M. J.; Troe, J., Unravelling combustion mechanisms through a quantitative understanding of elementary reactions. *Proceedings of the Combustion Institute* **2005,** *30* (1), 43-88.

2. Li, J.; Zhao, Z.; Kazakov, A.; Chaos, M.; Dryer, F. L.; Scire Jr, J. J., A comprehensive kinetic mechanism for CO, CH_2O, and CH_3OH combustion. *International Journal of Chemical Kinetics.* **2007,** *39* (3), 109-136.

3. Howard, J.; Essenhigh, R. In Mechanism of solid-partical combustion with simultaneous gas-phase volatiles combustion, Symposium (International) on Combustion, pp 399-408. Amsterdam, Netherlands: Elsevier, **1967.**

4. Jones, W.; Lindstedt, R., Global reaction schemes for hydrocarbon combustion. *Combustion and Flame* **1988,** *73* (3), 233-249.

5. Motherwell, W. B.; Crich, D., Free radical chain reactions in organic synthesis. Amsterdam, Netherlands: Elsevier, **2013.**

6. Zhang, S.; Horrocks, A. R., A review of flame retardant polypropylene fibres. *Progress in Polymer Science* **2003,** *28* (11), 1517-1538.

7. McAllister, S.; Chen, J.-Y.; Fernandez-Pello, A. C., Fundamentals of combustion processes. Vol. 302. Berlin, Germany: Springer, **2011.**

8. Frenklach, M.; Wang, H.; Rabinowitz, M. J., Optimization and analysis of large chemical kinetic mechanisms using the solution mapping method—combustion of methane. *Progress in Energy and Combustion Science* **1992,** *18* (1), 47-73.

9. Zeng, J.; Cao, L.; Xu, M.; Zhu, T.; Zhang, J. Z., Complex reaction processes in combustion unraveled by neural network-based molecular dynamics simulation. *Nature Communications* **2020,** *11* (1), 1-9.

10. Jungkamp, T. P.; Smith, J. N.; Seinfeld, J. H., Atmospheric oxidation mechanism of n-butane: the fate of alkoxy radicals. *The Journal of Physical Chemistry A* **1997,** *101* (24), 4392-4401.

11. Pelucchi, M.; Cavallotti, C.; Faravelli, T.; Klippenstein, S., H-Abstraction reactions by OH, HO_2, O, O_2 and benzyl radical addition to O_2 and their implications for kinetic modelling of toluene oxidation. *Physical Chemistry Chemical Physics* **2018,** *20* (16), 10607-10627.

12. Alvarez-Idaboy, J. R.; Mora-Diez, N.; Boyd, R. J.; Vivier-Bunge, A., On the importance of prereactive complexes in molecule− radical reactions: Hydrogen abstraction from aldehydes by OH. *Journal of the American Chemical Society* **2001,** *123* (9), 2018-2024.

13. Chakir, A.; Cathonnet, M.; Boettner, J.; Gaillard, F., Kinetic study of n-butane oxidation. *Combustion Science and Technology* **1989,** *65* (4-6), 207-230.

14. Calvert, J. G.; Madronich, S., Theoretical study of the initial products of the atmospheric oxidation of hydrocarbons. *Journal of Geophysical Research: Atmospheres* **1987,** *92* (D2), 2211-2220.

15. Pantelaki, I.; Voutsa, D., Organophosphate flame retardants (OPFRs): A review on analytical methods and occurrence in wastewater and aquatic environment. *Science of The Total Environment* **2019,** *649*, 247-263.

16. Hoffman, K.; Butt, C. M.; Webster, T. F.; Preston, E. V.; Hammel, S. C.; Makey, C.; Lorenzo, A. M.; Cooper, E. M.; Carignan, C.; Meeker, J. D., Temporal trends in exposure to organophosphate flame retardants in the United States. *Environmental Science and Technology Letters* **2017,** *4* (3), 112-118.

17. Yao, C.; Yang, H.; Li, Y., A review on organophosphate flame retardants in the environment: Occurrence, accumulation, metabolism and toxicity. *Science of The Total Environment* **2021,** *795*, 148837.

18. Salamova, A.; Ma, Y.; Venier, M.; Hites, R. A., High levels of organophosphate flame retardants in the Great Lakes atmosphere. *Environmental Science and Technology Letters* **2014,** *1* (1), 8-14.

19. Hoffman, K.; Daniels, J. L.; Stapleton, H. M., Urinary metabolites of organophosphate flame retardants and their variability in pregnant women. *Environment International* **2014,** *63*, 169-172.

20. Organophosphate. Retrieved on Febuary-01, **2023** from https://commons.wikimedia.org/wiki/File:Organophosphate.svg

21. Retrieved on Febuary-01, **2023** from https://www.lucintel.com/press/organophosphorus-flame-retardant-market.aspx. Dallas, Texas, USA

22. Huang, J.; Ye, L.; Fang, M.; Su, G., Industrial production of organophosphate flame retardants (OPFRs): big knowledge gaps need to be filled? *Bulletin of Environmental Contamination and Toxicology* **2022,** *108* (5), 809-818.

23. Tuazon, E. C.; Atkinson, R.; Aschmann, S. M.; Arey, J.; Winer, A. M.; Pitts, J. N., Atmospheric loss processes of 1, 2-dibromo-3-chloropropane and trimethyl phosphate. *Environmental Science and Technology Letters* **1986,** *20* (10), 1043-1046.

24. Burns, D. S.; Cory, M. G.; Taylor, D. E.; Bunte, S. W.; Runge, K.; Vasey, J. L., A comparison of primary and secondary hydrogen abstraction from organophosphates by hydroxyl radical. *International Journal of Chemical Kinetics* **2013,** *45* (3), 187-201.

25. Gilpin, R.; Schiff, H.; Welge, K., Photodissociation of O_3 in the Hartley Band. Reactions of $O(^1D)$ and O_2 ($1\ \Sigma\ g+$) with O_3 and O_2. *The Journal of Chemical Physics* **1971,** *55* (3), 1087-1093.

26. Streit, G.; Howard, C. J.; Schmeltekopf, A.; Davidson, J.; Schiff, H., Temperature dependence of $O(^1D)$ rate constants for reactions with O_2, N_2, CO_2, O_3, and H_2O. *The Journal of Chemical Physics* **1976,** *65* (11), 4761-4764.

27. Wulf, O. R.; Tolman, R. C., The thermal decomposition of ozone. *Proceedings of the National Academy of Sciences* **1927,** *13* (5), 272-275.

28. Cantrell, C. A.; Shetter, R. E.; Calvert, J. G., Branching ratios for the $O(^1D)+ N_2O$ reaction. *Journal of Geophysical Research: Atmospheres* **1994,** *99* (D2), 3739-3743.

29. Sangwan, M.; Chesnokov, E. N.; Krasnoperov, L. N., Reaction OH+OH studied over the 298–834 K temperature and 1-100 bar pressure ranges. *The Journal of Physical Chemistry A* **2012,** *116* (24), 6282-6294.

30. Smith, I. W., The temperature-dependence of elementary reaction rates: beyond Arrhenius. *Chemical Society Reviews* **2008,** *37* (4), 812-826.

31. Crim, F. F., Bond-selected chemistry: vibrational state control of photodissociation and bimolecular reaction. *The Journal of Physical Chemistry* **1996,** *100* (31), 12725-12734.

32. Bernshtein, V.; Oref, I., Termolecular collisions: comparison between analytical expression and trajectory calculations. *The Journal of Physical Chemistry A* **2004,** *108* (39), 8131-8133.

33. Fernández-Ramos, A.; Miller, J. A.; Klippenstein, S. J.; Truhlar, D. G., Modeling the kinetics of bimolecular reactions. *Chemical Reviews* **2006,** *106* (11), 4518-4584.

34. Atkins, P.; Atkins, P. W.; de Paula, J., Atkins' physical chemistry. Oxford, United Kingdom, Oxford University Press: **2014.**

35. Chen, M. M.; Schaefer III, H. F., Potential energy surface for the $Li+ HF\rightarrow LiF+ H$ reaction. *The Journal of Chemical Physics* **1980,** *72* (8), 4376-4393.

36. Laidler, K. J.; King, M. C., The development of transition-state theory. *The Journal of Physical Chemistry* **1983,** *87* (15), 2657-2664.

37. Truhlar, D. G.; Hase, W. L.; Hynes, J. T., Current status of transition-state theory. *The Journal of Physical Chemistry* **1983,** *87* (15), 2664-2682.

38. Mora-Diez, N.; Alvarez-Idaboy, J. R.; Boyd, R. J., A quantum chemical and TST study of the OH hydrogen-abstraction reaction from substituted aldehydes: FCHO and ClCHO. *The Journal of Physical Chemistry A* **2001,** *105* (39), 9034-9039.

39. Pollak, E.; Child, M. S.; Pechukas, P., Classical transition state theory: a lower bound to the reaction probability. *The Journal of Chemical Physics* **1980,** *72* (3), 1669-1678.

40. Truhlar, D. G.; Garrett, B. C.; Klippenstein, S. J., Current status of transition-state theory. *The Journal of Physical Chemistry* **1996,** *100* (31), 12771-12800.

41. Mozurkewich, M.; Benson, S. W., Self - Reaction of HO_2 and DO_2: Negative temperature dependence and pressure effects. *International Journal of Chemical Kinetics* **1985,** *17* (8), 787-807.

42. Benson, S. W.; Dobis, O., Existence of negative activation energies in simple bimolecular metathesis reactions and some observations on too-fast reactions. *The Journal of Physical Chemistry A* **1998,** *102* (27), 5175-5181.

43. Mozurkewich, M.; Lamb, J. J.; Benson, S. W., Negative activation energies and curved Arrhenius plots. 2. Hydroxyl+ carbon monoxide. *The Journal of Physical Chemistry* **1984,** *88* (25), 6435-6441.

44. Mozurkewich, M.; Benson, S. W., Negative activation energies and curved Arrhenius plots. 1. Theory of reactions over potential wells. *The Journal of Physical Chemistry* **1984,** *88* (25), 6429-6435.

45. Lamb, J. J.; Mozurkewich, M.; Benson, S. W., Negative activation energies and curved Arrhenius plots. 3. Hydroxyl+ nitric acid and hydroxyl+ peroxynitric acid. *The Journal of Physical Chemistry* **1984,** *88* (25), 6441-6448.

46. Krasnoperov, L. N.; Peng, J.; Marshall, P., Modified transition state theory and negative apparent activation energies of simple metathesis reactions: Application to the reaction CH_3+HBr→CH_4+ Br. *The Journal of Physical Chemistry A* **2006,** *110* (9), 3110-3120.

47. Troe, J., Fall - off Curves of Unimolecular Reactions. *Berichte der Bunsengesellschaft für Physikalische Chemie* **1974,** *78* (5), 478-488.

48. Carstensen, H.-H.; Dean, A. M., The kinetics of pressure-dependent reactions. *Comprehensive Chemical Kinetics* **2007,** *42*, 101-184.

49. Krasnoperov, L.; Chesnokov, E.; Stark, H.; Ravishankara, A., Elementary reactions of formyl (HCO) radical studied by laser photolysis—transient absorption spectroscopy. *Proceedings of the Combustion Institute* **2005,** *30* (1), 935-943.

50. Saripalli, P. S.; Sedwick, R. J., Nitrous Oxide Decomposition Using Inductively Heated Heat Exchangers. *Journal of Propulsion and Power* **2020,** *36* (6), 887-900.

51. Smith, R., Role of hydroxyl radicals in combustion. *Coal Research. Commonwealth Scientific and Industrial Research Organisation;(Australia)* **1967,** *32*.

52. Westbrook, C. K., Chemical kinetics of hydrocarbon ignition in practical combustion systems. *Proceedings of the Combustion Institute* **2000,** *28* (2), 1563-1577.

53. Atkinson, R., Kinetics and mechanisms of the gas-phase reactions of the hydroxyl radical with organic compounds under atmospheric conditions. *Chemical Reviews* **1986,** *86* (1), 69-201.

54. Lelieveld, J.; Dentener, F.; Peters, W.; Krol, M., On the role of hydroxyl radicals in the self-cleansing capacity of the troposphere. *Atmospheric Chemistry and Physics* **2004,** *4* (9/10), 2337-2344.

55. Finlayson-Pitts, B. J.; Pitts Jr, J. N., Tropospheric air pollution: ozone, airborne toxics, polycyclic aromatic hydrocarbons, and particles. *Science* **1997,** *276* (5315), 1045-1051.

56. Calvert, J. G.; Derwent, R. G.; Orlando, J. J.; Wallington, T. J.; Tyndall, G. S., Mechanisms of atmospheric oxidation of the alkanes. Oxford, United Kingdom, Oxford University Press:**2008**.

57. Ravishankara, A., Kinetics of radical reactions in the atmospheric oxidation of CH_4. *Annual Review of Physical Chemistry* **1988,** *39* (1), 367-394.

58. Bahng, M.-K.; Macdonald, R. G., Determination of the Rate Constant for the OH ($X^2\Pi$)+ OH ($X^2\Pi$)⟶ O(^{3}P)+ H_2O Reaction over the Temperature Range 293− 373 K. *The Journal of Physical Chemistry A* **2007,** *111* (19), 3850-3861.

59. Kaufman, F.; Del Greco, F. In *Fast reactions of OH radicals*, Symposium (International) on Combustion, pp 659-668. Elsevier, Amsterdam, Netherlands, **1963.**

60. Caldwell, J.; Back, R., Combination reactions of hydroxyl radicals in the flash photolysis of water vapour. *Transactions of the Faraday Society* **1965,** *61*, 1939-1945.

61. Dixon - Lewis, G.; Wilson, W.; Westenberg, A., Studies of hydroxyl radical kinetics by quantitative ESR. *The Journal of Chemical Physics* **1966,** *44* (8), 2877-2884.

62. Wilson Jr, W. E.; O'Donovan, J., Mass-Spectrometric Study of the Reaction Rate of OH with Itself and with CO. *The Journal of Chemical Physics* **1967,** *47* (12), 5455-5457.

63. McKenzie, A.; Mulcahy, M.; Steven, J., Kinetics of decay of hydroxyl radicals at low pressure. *The Journal of Chemical Physics* **1973,** *59* (6), 3244-3254.

64. Clyne, M. A.; Down, S., Kinetic behaviour of OH $X^2\Pi$ and $A^2\sigma+$ using molecular resonance fluorescence spectrometry. *Journal of the Chemical Society, Faraday Transactions 2: Molecular and Chemical Physics* **1974,** *70*, 253-266.

65. Trainor, D. W.; von Rosenberg Jr, C., Flash photolysis study of the gas phase recombination of hydroxyl radicals. *The Journal of Chemical Physics* **1974,** *61* (3), 1010-1015.

66. Wagner, G.; Zellner, R., Temperature Dependence of the Reaction OH+ OH→ H_2O+ O. *Berichte der Bunsengesellschaft für physikalische Chemie* **1981,** *85* (12), 1122-1128.

67. Sangwan, M.; Chesnokov, E. N.; Krasnoperov, L. N., Reaction CH_3+ OH studied over the 294–714 K temperature and 1–100 bar pressure ranges. *The Journal of Physical Chemistry A* **2012,** *116* (34), 8661-8670.

68. Harding, L. B.; Wagner, A. F. In *Theoretical study of the reaction rates of OH+ OH⇔ H_2O+ O*, Symposium (International) on Combustion, pp 983-989. Amsterdam, Netherlands: Elsevier, **1989.**

69. Karkach, S. P.; Osherov, V. I., Ab initio analysis of the transition states on the lowest triplet H_2O_2 potential surface. *The Journal of Chemical Physics* **1999,** *110* (24), 11918-11927.

70. Brouwer, L.; Cobos, C.; Troe, J.; Dübal, H. R.; Crim, F., Specific rate constants k (E, J) and product state distributions in simple bond fission reactions. II. Application to HOOH→OH+OH. *The Journal of Chemical Physics* **1987,** *86* (11), 6171-6182.

71. Maergoiz, A.; Nikitin, E.; Troe, J., Statistical adiabatic channel calculation of accurate low-temperature rate constants for the recombination of OH radicals in their ground rovibronic state. *The Journal of Chemical Physics* **1995,** *103* (6), 2083-2091.

72. Sun, H.; Li, Z., Rate constant measurement for the OH+OH→ H_2O+O reaction at 220 – 320 K using discharge flow/mass spectrometer/resonance fluorescence technique. *Chemical Physics Letters* **2004,** *399* (1-3), 33-38.

73. Atkinson, R.; Baulch, D.; Cox, R. A.; Crowley, J.; Hampson, R.; Hynes, R.; Jenkin, M.; Rossi, M.; Troe, J., Evaluated kinetic and photochemical data for atmospheric chemistry: Volume I-gas phase reactions of Ox, HOx, NOx and SOx species. *Atmospheric Chemistry and Physics* **2004,** *4* (6), 1461-1738.

74. Atkinson, R.; Baulch, D.; Cox, R.; Hampson Jr, R.; Kerr, J.; Rossi, M.; Troe, J., Evaluated kinetic and photochemical data for atmospheric chemistry, organic species: Supplement VII. *Journal of Physical and Chemical Reference Data* **1999,** *28* (2), 191-393.

75. Hippler, H.; Rahn, R.; Troe, J., Temperature and pressure dependence of ozone formation rates in the range 1–1000 bar and 90–370 K. *The Journal of Chemical Physics* **1990,** *93* (9), 6560-6569.

76. Vranckx, S.; Peeters, J.; Carl, S., Kinetics of $O(^1D)+ H_2O$ and $O(^1D)+ H_2$: absolute rate coefficients and $O(^3P)$ yields between 227 and 453 K. *Physical Chemistry Chemical Physics* **2010,** *12* (32), 9213-9221.

77. Carl, S. A., A highly sensitive method for time-resolved detection of $O(^1D)$ applied to precise determination of absolute $O(^1D)$ reaction rate constants and $O(^3P)$ yields. *Physical Chemistry Chemical Physics* **2005,** *7* (24), 4051-4053.

78. Takahashi, K.; Takeuchi, Y.; Matsumi, Y., Rate constants of the $O(^1D)$ reactions with N_2, O_2, N_2O, and H_2O at 295 K. *Chemical Physics Letters* **2005,** *410* (4-6), 196-200.

79. Dunlea, E. J.; Ravishankara, A., Kinetic studies of the reactions of $O(^1D)$ with several atmospheric molecules. *Physical Chemistry Chemical Physics* **2004,** *6* (9), 2152-2161.

80. Atkinson, R.; Baulch, D.; Cox, R.; Hampson Jr, R. F.; Kerr, J.; Troe, J., Evaluated kinetic and photochemical data for atmospheric chemistry: supplement III. IUPAC subcommittee on gas kinetic data evaluation for atmospheric chemistry. *Journal of Physical and Chemical Reference Data* **1989,** *18* (2), 881-1097.

81. Zellner, R.; Erler, K.; Field, D. In *Kinetics of the recombination reaction OH+H+ M→H_2O+M at low temperatures*, Symposium (International) on Combustion, pp 939-948. Amsterdam, Netherlands: Elsevier, **1977.**

82. Troe, J.; Warnatz, J., Evaluated kinetic data for combustion modelling supplement i. *Journal of Physical and Chemical Reference Data* **1994,** *23*, 847.

83. Michael, J.; Su, M.-C.; Sutherland, J.; Carroll, J.; Wagner, A., Rate constants for $H+O_2+M \rightarrow HO_2+$ M in seven bath gases. *The Journal of Physical Chemistry A* **2002,** *106* (21), 5297-5313.

84. Tsang, W.; Hampson, R., Chemical kinetic data base for combustion chemistry. Part I. Methane and related compounds. *Journal of Physical and Chemical Reference Data* **1986,** *15* (3), 1087-1279.

85. Fulle, D.; Hamann, H.; Hippler, H.; Troe, J., Temperature and pressure dependence of the addition reactions of HO to NO and to NO_2. IV. Saturated laser-induced fluorescence measurements up to 1400 bar. *The Journal of Chemical Physics* **1998,** *108* (13), 5391-5397.

86. Keyser, L. F., Kinetics of the reaction hydroxyl+ hydroperoxo. fwdarw. water+ oxygen from 254 to 382 K. *The Journal of Physical Chemistry* **1988,** *92* (5), 1193-1200.

87. Atkinson, R.; Baulch, D.; Cox, R.; Hampson Jr, R.; Kerr, J.; Rossi, M.; Troe, J., Evaluated kinetic, photochemical and heterogeneous data for atmospheric chemistry: Supplement V. IUPAC Subcommittee on Gas Kinetic Data Evaluation for Atmospheric Chemistry. *Journal of Physical and Chemical Reference Data* **1997,** *26* (3), 521-1011.

88. Baulch, D.; Cobos, C.; Cox, R.; Esser, C.; Frank, P.; Just, T.; Kerr, J.; Pilling, M.; Troe, J.; Walker, R., Evaluated kinetic data for combustion modelling. *Journal of Physical and Chemical Reference Data* **1992,** *21* (3), 411-734.

89. Greenblatt, G. D.; Ravishankara, A., Laboratory studies on the stratospheric NOx production rate. *Journal of Geophysical Research: Atmospheres* **1990,** *95* (D4), 3539-3547.

90. Tanaka, N.; Takayanagi, M.; Hanazaki, I., Nascent rotational and vibrational distributions in ^{16}OH and ^{18}OH produced in the reaction of $O(^1D)$ with $H_2{}^{18}O$. *Chemical Physics Letters* **1996,** *254* (1-2), 40-46.

91. Gericke, K.-H.; Comes, F., Energy partitioning in the reaction $O(^1D)+ H_2O\rightarrow$ OH+ OH. *Chemical Physics Letters* **1980,** *74* (1), 63-66.

92. Manion, J., NIST chemical kinetics database, NIST standard reference database 17, version 7.0 (web version), release 1.4. 3, data version 2008.12. Retrieved on Febuary-01, **2023** from http://kinetics.nist.gov/2008.

93. Tapscott, R. E.; Sheinson, R. S.; Babushok, V.; Nyden, M. R.; Gann, R. G., Alternative fire suppressant chemicals: a research review with recommendations. *NIST Technical Note* **2001,** *1443*, 13.

94. Retrieved on Febuary-01, **2023** from https://en.wikipedia.org/wiki/Dimethyl_methylphosphonate.

95. Hastie, J. W.; Bonnell, D. W., Molecular Chemistry of Inhibited D Combustion Systems. Boulder, Colorado, USA: National Bureau of Standards, **1980.**

96. Twarowski, A., The influence of phosphorus oxides and acids on the rate of H+ OH recombination. *Combustion and Flame* **1993,** *94* (1-2), 91-107.

97. Twarowski, A., Photometric determination of the rate of H_2O formation from H and OH in the presence of phosphine combustion products. *Combustion and Flame* **1993,** *94* (4), 341-348.

98. Twarowski, A., The temperature dependence of H+ OH recombination in phosphorus oxide containing post-combustion gases. *Combustion and Flame* **1996,** *105* (3), 407-413.

99. Korobeinichev, O. P.; Shvartsberg, V. M.; Chernov, A. A., The destruction chemistry of organophosphorus compounds in flames—II: structure of a hydrogen–oxygen flame doped with trimethyl phosphate. *Combustion and Flame* **1999,** *118* (4), 727-732.

100. Korobeinichev, O.; Shvartsberg, V.; Chernov, A.; Mokrushin, V. In *Hydrogen-oxygen flame doped with trimethyl phosphate, its structure and trimethyl phosphate destruction chemistry*, Symposium (International) on Combustion, pp 1035-1042. Amsterdam, Netherlands: Elsevier, **1996.**

101. Korobeinichev, O.; Bolshova, T.; Shvartsberg, V.; Chernov, A., Inhibition and promotion of combustion by organophosphorus compounds added to flames of CH_4 or H_2 in O_2 and Ar. *Combustion and Flame* **2001,** *125* (1-2), 744-751.

102. Glaude, P.; Curran, H.; Pitz, W.; Westbrook, C., Kinetic study of the combustion of organophosphorus compounds. *Proceedings of the Combustion Institute* **2000,** *28* (2), 1749-1756.

103. Glaude, P.; Melius, C.; Pitz, W.; Westbrook, C., Detailed chemical kinetic reaction mechanisms for incineration of organophosphorus and fluoroorganophosphorus compounds. *Proceedings of the Combustion Institute* **2002,** *29* (2), 2469-2476.

104. Jayaweera, T.; Melius, C.; Pitz, W.; Westbrook, C.; Korobeinichev, O.; Shvartsberg, V.; Shmakov, A.; Rybitskaya, I.; Curran, H. J., Flame inhibition by phosphorus-containing compounds over a range of equivalence ratios. *Combustion and Flame* **2005,** *140* (1-2), 103-115.

105. Green, J., A review of phosphorus-containing flame retardants. *Journal of Fire Sciences* **1992,** *10* (6), 470-487.

106. Costa, L. G., Organophosphorus compounds. In Recent Advances in Nervous System Toxicology, pp 203-246. Berlin, Germany: Springer, **1988.**

107. Aschmann, S. M.; Long, W. D.; Atkinson, R., Rate constants for the gas-phase reactions of OH radicals with dimethyl phosphonate over the temperature range of 278− 351 K and for a series of other organophosphorus compounds at∼ 280 K. *The Journal of Physical Chemistry A* **2008,** *112* (21), 4793-4799.

108. Zhang, X.; Sangwan, M.; Yan, C.; Koshlyakov, P. V.; Chesnokov, E. N.; Bedjanian, Y.; Krasnoperov, L. N., Disproportionation channel of the self-reaction of hydroxyl radical, OH+OH→ H_2O+ O, revisited. *The Journal of Physical Chemistry A* **2020,** *124* (20), 3993-4005.

109. Sangwan, M.; Krasnoperov, L. N., Disproportionation channel of self-reaction of hydroxyl radical, OH+OH→H_2O+O, studied by time-resolved oxygen atom trapping. *The Journal of Physical Chemistry A* **2012,** *116* (48), 11817-11822.

110. Yan, C.; Kocevska, S.; Krasnoperov, L. N., Kinetics of the reaction of CH_3O_2 radicals with OH studied over the 292–526 K temperature range. *The Journal of Physical Chemistry A* **2016,** *120* (31), 6111-6121.

111. Aguila, A.; O'Shea, K. E.; Tobien, T.; Asmus, K.-D., Reactions of hydroxyl radical with dimethyl methylphosphonate and diethyl methylphosphonate. A fundamental mechanistic study. *The Journal of Physical Chemistry A* **2001,** *105* (33), 7834-7839.

112. Gao, Y.; Alecu, I.; Hsieh, P.; Morgan, B. P.; Marshall, P.; Krasnoperov, L. N., Thermochemistry is not a lower bound to the activation energy of endothermic reactions: A kinetic study of the gas-phase reaction of atomic chlorine with ammonia. *The Journal of Physical Chemistry A* **2006,** *110* (21), 6844-6850.